8-2019

High Resolution Neutron Imaging with Li-glass Multicore Scintillating Fiber and Diffusion Studies to Enable Improved Neutron Imaging

Michael Moore
University of Tennessee

Recommended Citation

Moore, Michael, "High Resolution Neutron Imaging with Li-glass Multicore Scintillating Fiber and Diffusion Studies to Enable Improved Neutron Imaging. " PhD diss., University of Tennessee, 2019.
https://trace.tennessee.edu/utk_graddiss/5681

To the Graduate Council:

I am submitting herewith a dissertation written by Michael Moore entitled "High Resolution Neutron Imaging with Li-glass Multicore Scintillating Fiber and Diffusion Studies to Enable Improved Neutron Imaging." I have examined the final electronic copy of this dissertation for form and content and recommend that it be accepted in partial fulfillment of the requirements for the degree of Doctor of Philosophy, with a major in Nuclear Engineering.

Jason Hayward, Major Professor

We have read this dissertation and recommend its acceptance:

Steven Zinkle, Charles Melcher, Howard Hall, Lawrence Heilbronn

Accepted for the Council:

Dixie L. Thompson

Vice Provost and Dean of the Graduate School

(Original signatures are on file with official student records.)

High Resolution Neutron Imaging with Li-glass Multicore Scintillating Fiber and Diffusion Studies to Enable Improved Neutron Imaging

A Dissertation Presented for the
Doctor of Philosophy
Degree
The University of Tennessee, Knoxville

Michael Edward Moore
August 2019

To my wife,

Angela you are my lobster

ACKNOWLEDGEMENTS

My most sincere thanks are owed to my wife, Angela, for her selfless devotion to our relationship that inexorably strengthened my resolve during my graduate studies. Together, we are indefatigable. I must also thank my advisor, Jason Hayward, whose mentorship encourages self-improvement in all aspects of scientific exploration. Your capacity for understanding, patience, and integrity has set an honorable exemplar for my own life. I would also like to thank Gilberto Brambilla at the University of Southampton and Joris Lousteau at the Politecnico di Milano for their successful endeavors in creating the scintillating multicore fiber. I thank Pavel Trtik at the Paul Scherrer Institut for his unparalleled experimental assistance during our beamline measurements with the Neutron Microscope. Additionally, I thank Hassina Bilheux at Oak Ridge National Laboratory for her instruction and the opportunities she afforded me to participate in neutron science early in my graduate studies. Finally, I wish to thank the members of my dissertation committee for freely offering up both their experienced input and valued time.

COPYRIGHT DISCLAIMER

Some additional commentary, minor grammatical corrections, redaction, and adaptation of the dissertation author's published journal articles (PJAs) may be transformative of the original work present. Therefore, the PJAs should be referenced directly before citing this work.

Embedded Elsevier PJAs that are part of this submission can be found on ScienceDirect with their respective DOI links back to the formal publications.

In reference to IEEE copyrighted material which is used with permission in this thesis, the IEEE does not endorse any of the University of Tennessee's products or services. Internal or personal use of this material is permitted. If interested in reprinting/republishing IEEE copyrighted material for advertising or promotional purposes or for creating new collective works for resale or redistribution, please go to:

http://www.ieee.org/publications_standards/publications/rights/rights_link.html to learn how to obtain a License from RightsLink.

Chapter 2, is a reprint of the material as it appears published in *25th International Conference on Optical Fiber Sensors IEEE* 2017. A*uthors:* M. E. Moore, X. Zhang, X. Feng, G. Brambilla, J.P. Hayward. "A multicore compound glass optical fiber for neutron imaging." https://doi.org/10.1117/12.2267529 The dissertation author was the primary investigator and author of this paper.

Chapter 3, is a reprint of the material as it appears published in *Nuclear Inst. and Methods in Physics Research, A* 2018. A*uthors:* M. E. Moore, J. Lousteau, P. Trtik, H.Z.

Bilheux, D. Pugliese, D. Milanese, A.T. Simone, G. Brambilla, J.P. Hayward. “Fabrication and experimental evaluation of microstructured ^{6}Li silicate fiber arrays for high spatial resolution neutron imaging.” https://doi.org/10.1016/j.nima.2018.12.010 The dissertation author was the primary investigator and author of this paper.

Chapter 4 is a reprint of material currently under review for publication. A*uthors:* M. E. Moore, P. Trtik, J. Lousteau, D. Pugliese, G. Brambilla, J.P. Hayward. “Neutron imaging with Li-glass based multicore SCIntillating FIber (SCIFI).” The dissertation author was the primary investigator and author of this paper.

Chapter 5 is a reprint of the material as it appears published in *Journal of Non-Crystalline Solids* 2018. A*uthors:* M.E. Moore, H. Xue, P. Vilmercati, S.J. Zinkle, N. Mannella, J.P. Hayward. “Thermal diffusion of mixed valence Ce in ^{6}Li loaded silicate glass for neutron imaging." https://doi.org/10.1016/j.jnoncrysol.2018.06.004 The dissertation author was the primary investigator and author of this paper.

Chapter 6 is a reprint of material currently under review for publication. A*uthors:* M. E. Moore, C. Delzer, J. Watts, B. L. Musicó, C. Xu, R. M. Collette, P. D. Rack, Y. Zhang, C. L. Melcher, S. McConchie, and J. P. Hayward. “Studying the effects of thermally diffusing Ce into the surface of $YAlO_3$ for associated particle imaging.” The dissertation author was the primary investigator and author of this paper.

Chapter 7, is in part, a reproduction of all the papers list above and authored by the dissertation author.

ABSTRACT

High resolution neutron imaging is an essential tool used for fundamental characterization of novel x-ray opaque microstructures. Currently, advanced neutron scattering facilities enable users to image materials with state-of-the-art neutron radiography spatial resolutions of approximately 10-15 microns. Continued progress towards micron resolution is limited by the intensity and the linearity of available thermal neutron fluxes. This places an emphasis on increasing neutron conversion/detection efficiency while maintaining the spatial accuracy of the projected radiograph. This dissertation reports the results of experimental fabrication and characterization of a microstructured multicore 6-lithium-glass scintillating fiber as a proof-of-concept high resolution neutron imager.

The approach towards micron–level thermal neutron imaging and fundamental scintillator materials research for relevant imaging technologies are presented. Fabrication trials and neutron/gamma discrimination observations for an initial square-packed multicore design are described first. Then the fabrication process used for a proof-of-concept hexagonal-packed multicore design, and an evaluation of its radioluminescence and chemical stability is presented. Scintillation characteristics of a neutron imaging faceplate were estimated, and its spatial resolution was experimentally measured. The ultimate resolving power of the proof-of-concept multicore was comparable to the state-of-the-art. The impact of even higher resolution designs, with potential to track neutron conversion particles using smaller core pitch or different cladding material, is discussed.

Neutron imaging often requires nonlinear detection systems that can accurately represent the spatial features of an irradiated object. While thin film and microchannel plate detectors have been heavily researched for this application, little effort has been made to create selective scintillating regions within structured silicate glass detectors. This dissertation presents the continued research of diffusing trivalent cerium in lithium loaded glass. The creation of near surface regions of scintillation with thermal diffusion of the Ce^{3+} activator into ^{6}Li glass is presented, and its use for neutron imaging with a bent optical fiber taper is discussed. The activation energy of Ce within the silicate is calculated and its valance state is observed as a function of diffusion depth. The diffusion process is then adopted for use with YAP ($YAlO_3$:Ce) for associated particle imaging applications.

TABLE OF CONTENTS

LIST OF TABLES

LIST OF FIGURES

Chapter 1

Introduction

Neutrons are characteristically, and fundamentally, chargeless particles. Thus, neutrons cannot experience the Coulombic force. Similar to gamma-rays, neutrons interact with matter either via scattering or absorption. Unlike gammas, neutron interactions almost always result in energetic heavy charged particles. It is the detection of these energetic charged particles that allows one to indirectly infer the presence of neutrons. The dominant interaction mechanism for any given neutron is intrinsically controlled by the kinetic energy of that neutron. Neutron energy is liberally divided into two broad detection camps: fast and slow. For the purposes of this work, the distinction between fast and slow neutrons can be regarded as around an energy of 0.5 eV, i.e. the Cd cutoff energy.

Elastic scattering is the main mechanism for interaction of fast neutrons in matter. A single fast neutron may scatter and create recoil nuclei multiple times before slowing down or escaping a material. Provided that the energy transferred is sufficient, the recoiled nuclei can be detected. The number of scatters and the kinetic energy transferred are related to the fast neutron energy. However, the exact site of the initial fast neutron scatter is not well defined. Conversely, slow neutrons primarily interact with matter via some kind of absorption reaction. Neutron absorptions result in the prompt emission of energetic heavy charged particles, or, in the case of radiative capture, gamma-rays. Absorption reactions that convert slow neutrons into charged particles, that, in-turn, readily lose their kinetic energy to Coulombic forces within a short distance. However, these interactions are not useful in determining neutron energy.

This dissertation is primarily concerned with utilizing slow neutron absorptions for imaging. Imaging is associated with a wide range of methods and technologies to produce a representation of an object. Specifically, creating a two dimensional (2D) image with various forms of radiation is called radiography. Radiography is a form of Nondestructive Analysis (NDA) that reveals information about an object by projecting a beam of radiation, partially attenuated by the object, onto a detector. Dental x-rays are a common example of projectional radiography. The features and contrast of a dental radiograph are formed by the scattering and stopping, or attenuation, of x-rays within the imaged object. Because x-rays are more readily attenuated by elements with larger atomic numbers (Z), the dense bones and metals present in dental x-rays are imaged with greater contrast compared with the lesser attenuating cavities of air.

In contrast, neutron cross-sections do not directly correlate with Z. Neutrons tend to be more highly penetrating for high Z materials and are instead primarily attenuated by low Z materials, with some exceptions, see Figure 1-1. It is this complementary quality which makes imaging with neutrons ideal for applications that involve imaging organics, hydrogenous material, and other light elements, particularly when they are obscured by metals or other heavy materials, not easily penetrated by x-rays.

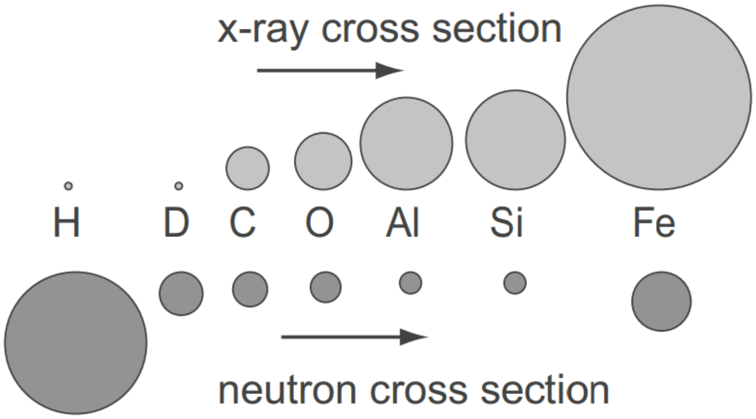

Figure 1-1. Visual comparison of the relative cross-sections of various elements for X-rays and for neutrons [1].

Neutron radiography is a well-established form of imaging that has been in use since 1935 [2], just 3 years after James Chadwick discovered the neutron [3]. Modern digital imaging with neutron radiography produces a pixel-by-pixel intensity measurement of the attenuation coefficient multiplied by the length of the imaged object. This well-established neutron attenuation relationship is expressed by the Beer-Lambert law:

$$I = I_0 exp^{(-\Sigma \mu_i x_i)} \quad \text{Equation 1-1}$$

where I_0 and I are the incident flux and unattenuated, or transmitted, flux of neutrons at iteration i, at thickness x for an attenuation coefficient μ. The attenuation coefficient is calculated as

$$\mu_i = \sigma_{tot} N_A c_i \quad \text{Equation 1-2}$$

where σ_{tot} is the total neutron cross section for scattering and absorption, N_A is Avogadro's Number, and c_i is the molar concentration at i. The neutrons within I that are transmitted through the object of interest can then be detected via elastic scattering or absorption. Slow neutrons are typically converted into charged particles by a neutron sensitive absorber, called a convertor. Neutron tomography is based upon these same physical concepts. The difference is while constructed neutron radiographs produce a 2D image, tomography produces a reconstructed three dimensional (3D) image. Specifically, computed Tomography (CT) utilizes rotation, either of imaged object or the neutron beam probing the object, to take multiple neutron radiographic projections of the object's cross-section at specific angles, or slices. A CT scan reconstructs a 3D image from these slices acquired in incremental angular steps about the object.

1.1 Thermal Neutrons

To reiterate, slow neutrons are readily absorbed and converted for detection. Neutron capture reactions on isotopes such as *^{3}He*, *^{6}Li*, *^{10}B*, *Gd*, and *^{235}U*, presented in Table 1-1, are commonly used to convert slow neutrons into a detectable charged particle(s) due to their relatively high cross sections for thermal capture. In regards to neutron energy regimes, thermal energies imply that the neutron is "room temperature," that is to say the neutron's kinetic energy is near 0.025 eV, possessing an approximate 2 Å wavelength, and traveling near to 2,200 m/s. The relationships between kinetic energy, deBroglie wavelength, and velocity of a neutron are:

$$E = \frac{mv^2}{2} = \frac{h^2}{2m} \times \frac{1}{\lambda^2} \quad \text{Equation 1-3}$$

$$E(meV) = \frac{81.82}{\lambda(\text{Å})^2} \quad \text{Equation 1-4}$$

$$\lambda(\text{Å}) = \frac{9.045}{\sqrt{E(meV)}} \quad \text{Equation 1-5}$$

$$v(ms^{-1}) = 437 \times \sqrt{E(meV)} \quad \text{Equation 1-6}$$

where the mass of a neutron, m, is $1.675 \times 10^{-27}\ kg$, and Planck's Constant, h, is $4.13568 \times 10^{-12}\ meV \cdot s$. The Paul Scherrer Institute provides a convenient breakdown of the relevant temperature regimes of neutrons encountered in high resolution imaging [5], see Table 1-2.

Table 1-1: Thermal neutron cross sections and charged particle production for some materials used as neutron converters (reproduced from [4]).

Isotope	*Reaction*	*Neutron absorption cross section barns at (2,200 m/s)*	*Charged particles and energies (keV)*	*Gamma-ray production?*
^{3}He	$^{3}He(n,p)\ ^{3}H$	5333	p: 573, ^{3}H: 191	*No*
^{6}Li	$^{6}Li\ (n,\alpha)\ ^{3}H$	940	^{3}H: 2727, α: 2055	*No*
^{10}B	$^{10}B(\mathrm{n},\alpha)^{7}Li$	3835	^{3}H: 1472, ^{7}Li: 480	*Yes*
^{nat}Gd	$^{\mathrm{nat}}Gd(n,\gamma)$	49700	*Conversion electron* 29– 191	*Yes*
^{157}Gd	$^{157}Gd(n,\gamma)^{158}Gd$	259000	*Conversion electron* 29– 182	*Yes*
^{235}U	$^{235}U(\mathrm{n},\mathrm{f})$	681	*Fission Products*	*Yes*

Table 1-2: Neutron kinetic energy classification (reproduced from [5])

Neutrons	*Energy range*	*Wavelength [Å]*	*Velocity [m/s]*
Ultra-Cold	$\leq$ 300 neV	$\geq$ 500	$\leq$ 8
Very Cold	300 neV - 0.12 meV	52.2 – 26.1	7.5 – 152
Cold	0.12 meV - 12 meV	26.1 – 2.6	152 – 1515
Thermal	12 meV - 100 meV	2.6 - 0.9	1515 - 4374
Epithermal	100 meV - 1eV	0.9 - 0.28	4374 - 13.8 10^{3}

Consider the scale of the wavelengths in Table 1-2. The wavelengths of thermal and cold neutrons are comparable to the interatomic spacing within crystals or the bond length of biological macromolecules. Similarly to x-rays, neutron diffraction is used to study a materials structure and produce indirect images [6]. As with radiography, x-ray and neutron diffraction are complementary analyses. While x-ray diffraction is suited to probe a shallow structure or superficial feature, neutrons are more penetrating and can probe the bulk crystallographic properties of a material.

High flux thermal neutron sources[i] used for imaging are either provided by a research reactor or a spallation source. Research reactors designs are dissimilar to power reactor designs. The objective of typical nuclear power reactors is the efficient moderation and use of fast fission neutrons to continue the chain reaction, and the extraction of the resulting heat. Such a neutron source design is counterproductive towards producing a large flux of external thermal neutrons source for imaging. So, research reactors developed for neutron science utilize highly enriched nuclear fuel and small cores sizes to produce continuous neutron fluxes on the order of $10^{14} - 10^{15}\ n/cm^{-2}/s^{-1}$. These neutrons are directed into external beamlines for energy selection and various advanced measurement applications [4]. Alternatively, spallation neutron sources accelerate protons to highly energetic speeds (~GeV) to bombard a heavy metal target, creating spalled neutrons. The proton beam current

---

[i] The topic of sources for neutron production is both vast and complex. This brief section is only intended to introduce the reader to the concepts that are relevant to neutron imaging, and is by no means intended to be a thorough description of neutron sources. Refer to Chapter 2 of [4] for further information on neutron sources.

can be either continuous or pulsed onto the metal target. Most accelerated proton beams possess a power in the kW to MW range [4]. Regardless of the source, the majority of beamlines utilize a neutron beam with a Maxwellian spectral distribution around thermal (25meV) energies for imaging applications [7].

Within the last 30 years, continuous and pulsed neutron sources such as the High Flux Isotope Reactor (HFIR) and the Spallation Neutron Source (SNS) at the Oak Ridge National Laboratory (ORNL), the China Spallation Neutron Source (CSNS) operated by the Institute of High Energy Physics (IHEP), the Japanese Spallation Neutron Source (JSNS) of the Japan Proton Accelerator Research Complex (J-PARC) in Japan, and the Swiss Spallation Neutron Source (SINQ) at the Paul Scherrer Institut (PSI), have been able to provide the neutron fluxes needed to support higher resolution neutron imaging [8]. In that time, neutron imaging facilities have impacted research on a variety of topics, including the growth of radiation detection crystals, multi-phase flow within fuel cells, next generation batteries, engineering materials, metallic additive manufacturing, biomedical, plant physiology, geosciences, diffraction contrast enhancement, and energy selective techniques [4] [9] [10] [11]. While it is worth acknowledging the recent success that neutron imaging has enjoyed, even higher-impact research is limited by the current spatial resolution provided by the available neutron sources and neutron detection instrumentation.

1.2 High Resolution Neutron Imaging

While x-ray imaging technologies are able to resolve features and reconstruct 3D tomographs at a submicron scale [12] [13] [14], the state-of-the-art spatial resolutions for neutron imaging is ~10 - 15 μm [7] [15] [16]. The neutron imaging research community emphasized the need to develop better detector technology, capable of reaching 1 μm spatial resolution, during the 10th World Conference on Neutron Radiography, 5-10 October 2014 [4] [17]. In particular, the following areas could be impacted if spatial resolution were further improved by an order of magnitude: combining imaging with diffraction and tomography [6] [18], observing scintillator crystal growth [19] [20], characterizing two-phase flow for fuel cells [1] [21] [22] [23] [24], mapping the lithium distributions in operating lithium-air batteries [25] [26] [27], performing bulk single crystal Laue diffraction [6], and investigating magnetism [28] [29]. High resolution neutron imaging, in particular, is the only means of observing some of these processes *in situ* and without disturbing them in a manner that may compromise the results.

1.2.1 Neutron Imaging Parameters

The image quality of a neutron radiograph (sharpness, contrast, noise, etc.) is determined by the unique parameters of the neutron source, detector/imager, and the readout.

1.2.1.1 Neutron Sources

To create sharp projections of an object with radiography, the incident flux should be a flat and parallel distribution that is orthogonal to the imaging plane. However, to produce thermal or cold neutrons for imaging, sources must first moderate the energetic neutrons produced from fission and spallation. Moderation results in randomly scattered neutrons emanating in all directions. Unfortunately, thermalized neutrons cannot be focused in a manner similar to charged particles. So, a parallel hole collimator (commonly referred to as the aforementioned beamline) is typically used to restrict the angular spread of the imaging neutrons to create a quasi-parallel beam, similarly to a pinhole camera. It is worth noting that optics capable of focusing thermal neutrons, referred to as Wolter mirrors, have been demonstrated as "microscope-like" image-forming lenses when positioned between an imaged object and a neutron imager [30]. Simulations suggest that Wolter mirrors may even be able to focus thermalized neutrons into a small field of view (FOV) further upstream in the collimating process [31]. However, the technology requires further development, where no current neutron source has yet integrated such optics upstream of the imaged object into a dedicated beamline for high resolution imaging applications.

The appropriateness of a neutron collimator for imaging use may be measured by the ratio of the length of the collimator (L) to the diameter of the collimator hole or aperture (D), see Figure 1-2; [ii] large L/D ratios will result in a narrower angular beam

---

[ii] Beamlines used for imaging applications typically employ adjustable aperture slits that can be closed to decrease D for higher spatial resolution, or opened to increase the imaging area for a larger radiograph.

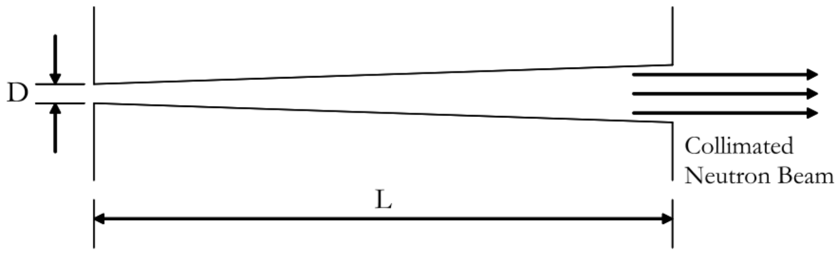

Figure 1-2. Divergent collimator illustrating the ratio of the collimator tube length (L) to its aperture diameter (D), or the L/D ratio [4].

spread, which facilitates a more accurate projection of the spatial features of an imaged object. Thus, thermal neutron flux intensity may be sacrificed through appropriately designed collimation as a tradeoff to improve image resolution. This is a major factor in imaging, which accounts for a portion of the discrepancy between the attainable spatial resolutions of neutron and x-ray sources. For example, current advanced neutron sources possess fluxes *at the imaging stages* near to $10^8\ n/cm^{-2}/s^{-1}$, which is five orders of magnitude below the neutron flux before moderation at the origin of the source. Even the most novel imaging beamlines in construction are targeting fluxes at the imaging stages around $\sim 10^9\ n/cm^{-2}/s^{-1}$ [32] [33]. Whereas, synchrotron sources like the Advanced Photon Source (APS) hosted by Argonne National Laboratory report irradiance above $10^{14} photons\ s^{-1} mm^{-2}$ at imaging stages [34]. Modern medical x-ray tubes produce over 100 kW of power for x-ray output [35]. Although direct comparisons are difficult, some sense of scale can be understood by recalling that the power of proton beams used to create the sources of spallation neutrons prior to moderation is typically between kW to MW.

1.2.1.2 Neutron Imagers

This dissertation explores the use of scintillation-based neutron imagers. The spatial resolution of scintillators used in thermal neutron imaging is typically limited in part by the design choice made in a tradeoff between the neutron detection, or conversion, efficiency and the desired spatial accuracy of the scintillation response. The scintillation light that results from the charged particle(s) produced by neutron conversion is emitted isotropically from the ionized scintillating volume. If this scintillation light is not guided, then determination of the exact location of the neutron interaction will be limited by the light spreading. Such uncertainty introduces systematic error which can be imperfectly corrected by methods that attempt to estimate the center of an interaction by fitting the gradient of the collected light from a single event. While utilizing a thicker, monolithic scintillator will increase neutron detection efficiency, it also decreases the spatial resolution of the radiograph, see Figure 1-3. Alternatively, a very thin, e.g., 10s of microns, scintillating conversion film may be used to limit the amount of spatial smearing that occurs, due to spreading of the light, before the light exits the scintillator to be readout by a photosensor. So, imaged scintillation for a single capture event will correspond to the orientation and length of the charged particle(s) track relative to the field of view. Still, the spatial resolution of thin scintillators is fundamentally limited by the variance introduced by the difference in the track orientations of the charged particle(s) emitted from neutron captures and the succeeding isotropic emission of scintillation light from neutron converters such as ^{6}Li, ^{10}B, and ^{157}Gd. Moreover, such a thin scintillator is very inefficient, resulting in perhaps unacceptably long imaging times. Thus, there is a clear need to marry the benefits of high neutron conversion efficiency and spatial resolution while also overcoming the neutron capture position uncertainty that results from charged particle track variance.

Focused development of structured, position-sensitive neutron detectors and accompanying post processing techniques have sought to overcome said spatial limitations. There are two popular types of position-sensitive designs used for

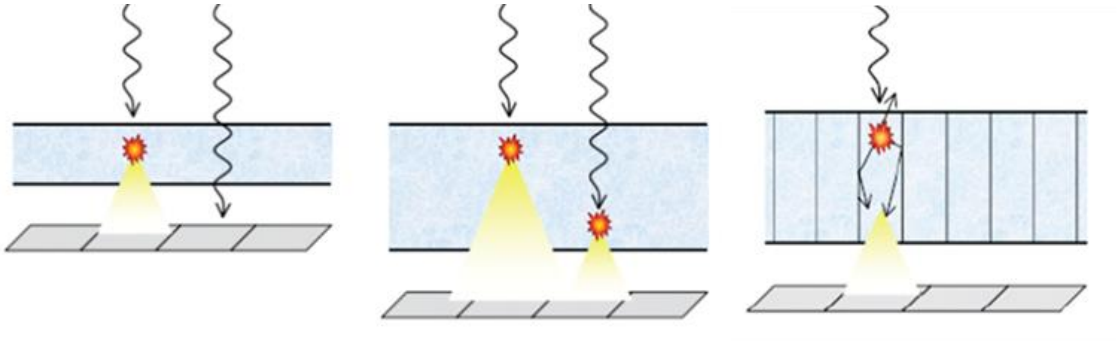

Figure 1-3. Illustration of the neutron conversion efficiency versus the accuracy of the positional response for a thin (*left*), thick (*center*), and structured scintillator (*right*). Schematic edited from an image that was previously hosted by Rad-icon Imaging Corp.

current high resolution neutron imagers. One approach uses scintillating screens, such as ^{6}LiF/ZnS and gadolinium oxysulfide ($^{157}Gd_2O_2S$:Tb), coupled to image intensifying optical setups to obtain high spatial resolution. A thin (several μm) structured scintillating layer with a highly enriched converter is used and can be optically segmented into pores to preserve position resolution [36]. Another successful approach abandons scintillators, and exploits Microchannel Plates (MCP) for imaging. MCPs are porous plates with glass capillaries coated with a secondary electron emitter. MCPs have been used for decades as electron multipliers, similarly to Photomultiplier Tubes (PMT) [37], see Figure 1-4. Because of their microstructured design, MCPs are regularly used as image intensifiers for optical light (when combined with a photocathode) and for direct detection of energetic photons and x-rays [38]. Within the last 30 years, application of the microscale positional response of MCPs has been expanded to include neutron imaging with significant research effort [39][40][41][42]. Neutron-sensitive MCPs incorporate a neutron convertor into the glass capillaries, see Figure 1-5. Combined with single event centroiding, neutron sensitive MCPs have been able to propel the state-of-the-art spatial resolutions of neutron imaging towards 10 μm [15].

Both of the approaches presented above introduce rigid structure to position captured neutrons with high resolution. While successful in providing current high resolution imaging, both technologies have drawbacks. The most efficient isotopically enriched screens are 10-39% efficient to thermal neutrons. High resolution MCP imaging is based on single event centroiding that requires complex and rate-limited

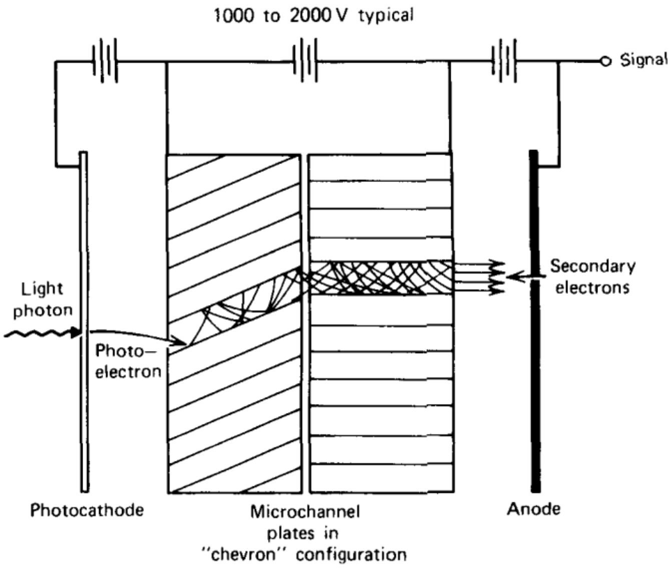

Figure 1-4. Elements of a PMT based on a MPC electron multiplication [37].

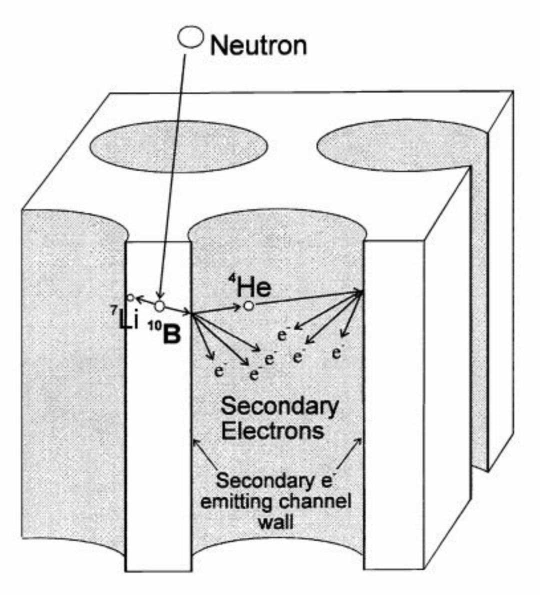

Figure 1-5. Schematic of neutron capture and conversion in a boron-rich MCP [40].

readouts, especially for large FOV radiographs.

The focus of this dissertation is to offer another, somewhat unconventional, approach towards micron resolution. In order to maintain neutron detection efficiency while continuing to improve spatial resolution, this research revitalizes the use of SCIntillating FIber (SCIFI) as a neutron imager, and potentially as neutron conversion charged particle trackers. To reach high resolution, a microstructured optical multicore SCIFI composed of scintillating ^{6}Li silicate glass cores with a cladding glass is used as a scintillation light guide, see Figure 1-6. Specifically, the well-known capture reaction for ^{6}Li, which emits alpha (α) and triton (t) particles back-to-back, ionizes primary and secondary electrons. Some of these electrons excite the Ce^{3+} activator, which, in turn, emits scintillation light at 395-432 nm in the near-UV/visible wavelength range. This light is transported through the neutron sensitive, microstructured waveguides to be observed by a photodetector. The fabrication technique described in Chapter 3 has the potential to generate multicore SCIFIs with active element pitch of order a few microns; this scale would allow for tracking the charged particles. This could, in turn, allow for estimating thermal neutron interaction locations with micron-level precision on an event-by-event basis, allowing one to overcome the inherent uncertainty that comes with the variance in the orientations of charged particle tracks in these scintillation detectors [43]. These concepts are discussed at length throughout the following chapters.

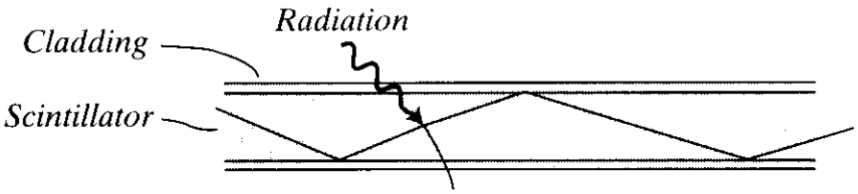

Figure 1-6. Cross section of a typical fiber scintillator. Some fraction of the emitted light is trapped by total internal reflection at the core-cladding interface [37].

1.2.1.3 Image Readout

The imager readout is important to preserving the quality of the image and increasing optical resolution. As described in Chapter 2, Chapter 3, and Chapter 4, there are usually three main stages for scintillator–based neutron imaging system readouts: 1) an optical magnification setup, 2) an image intensifier, and 3) a pixel based chip used as a digital camera for acquisition. Digital imaging has made substantial headway over the course of the last 20 years, and has allowed vastly improved post processing technics like event centroiding [15] [44]. Specifically, continued improvements to sensitivity, pixel size, and vertical shift rates (pixel readout speed) have caused Charge-Coupled Device (CCD) and Complementary Metal–Oxide–Semiconductors (CMOS) cameras to become the commonly preferred platform for neutron imaging. See Figure 1-7 for a typical setup of a neutron tomography system that makes use of sample rotation, a scintillator, and CCD. An optimal readout mechanism might seek to directly couple the SCIFI to a high resolution CCD chip, as suggested in Chapter 5. However, in the case of the SCIFI described above, directly coupling and aligning individual fibers to pixels is non-trivial, as is obtaining CCDs with micron-level pixel sizes. An ideal pixel pitch for such alignment would preferably be at most half of that of the fiber pitch.

1.3 Ce Doped Lithium Glass Scintillators

The neutron imaging presented in this dissertation relies on thermal neutron capture with isotopically enriched ^{6}Li Magnesium Aluminum Silicate (MAS) glass. The

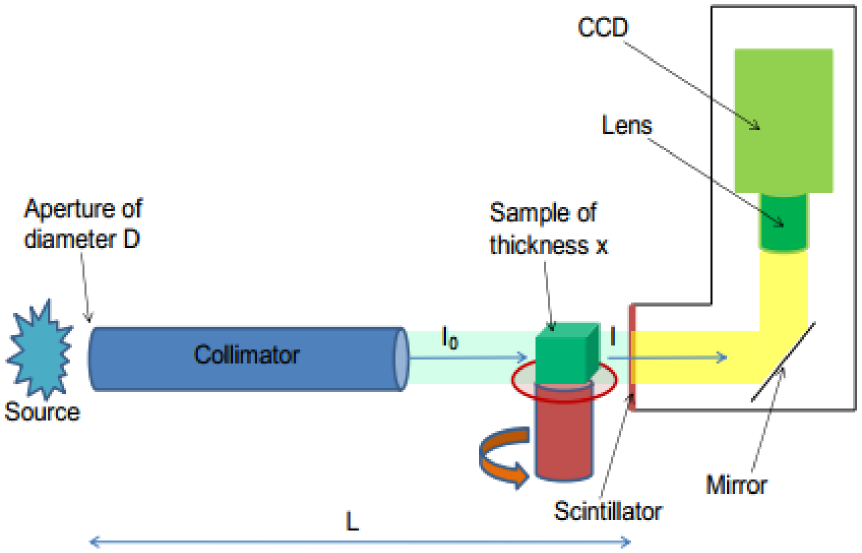

Figure 1-7. Example of a neutron imaging system capable of utilizing computed tomography in conjunction with rotation [27].

neutron reaction total cross section, σ_{tot}, for ^{6}Li is completely dominated at and below epithermal neutron energies by its capture cross section, σ_{cap}. Specifically, the relative order of magnitude of the $^{6}Li(n,\alpha)^{3}H$ capture reaction cross section is at least 3 times greater than the ^{6}Li elastic cross section, σ_{e}, for cold, thermal, and epithermal neutrons. According to the Evaluated Nuclear Data File (ENDF) published at the National Nuclear Data Center hosted by Brookhaven National Laboratory, at 0.025 eV, the ^{6}Li σ_{cap} and σ_{e} are 944 b and ~0.8 b, respectively [45]. Thus, it is often assumed that the radiographic neutron attenuation for the ^{6}Li MAS glass is a function of the $^{6}Li(n,\alpha)t$ capture reaction alone, where elastic scattering events can be neglected. The efficiency at which neutrons are stopped by Li-glass is typically referred to as a neutron detection, or (in the case of a neutral particle such as a neutron) conversion efficiency. Therefore, the thermal neutron conversion efficiency is essentially a function of the Li weight percent, enrichment, and the physical dimensions of the scintillator.

Although ^{10}B has a larger cross section, ^{6}Li has two important advantages as a neutron absorber for high resolution imaging. The first advantage is that the $^{6}Li\ (n,\alpha)\ ^{3}H$ reaction does not produce additional gammas that could contribute to the background. The second advantage is that the length of ^{6}Li conversion particle track is suited to the architectural scale of structured detectors, such that the orientation of the emission can be observed (provided enough light can be collected).

The seminal research and development of a scintillating glass that was sensitive to slow neutrons began by seeking to overcome the energy transfer difference between an amorphous glass matrix and long range ordered crystal structure. Primarily, in order to create a scintillating glass with good scintillation efficiency, the energy of an excited activator must not be absorbed by local ions or non-scintillating sites near to the activator site. In general, the discrete near-ultra violet (UV) emission of trivalent cerium (Ce^{3+}) is not strongly absorbed by most amorphous glasses. A Ce doped MAS glass is essentially transparent to its own scintillation light.

1.3.1 Conversion, Activation, and Scintillation

Following neutron capture on ^{6}Li, the α and t particles are emitted back-to-back, sharing a combined kinetic energy of 4.78 MeV, where the α gets 2.05 MeV and the t gets 2.73 MeV (see Figure 1-8). These charged particles are slowed and stopped by the Coulombic force of the charged bodies in the glass medium being traveled through following emission. In this way, the surrounding Li silicate glass matrix is ionized, creating primary and secondary electrons. For lithium enriched MAS glass, an α will travel ~7 μm and the t will travel ~40 μm [46]. These track lengths are comparable to those found using SRIM-2013 [47] with the composition of aluminosilicate glass defined for GS20 as reported by [46], with the addition of 6.941 weight (amu) of Li, and a compound density of 2.5 g/cm^3.

The resulting ionized primary and secondary electrons diffuse through the composite glass matrix with cylindrical radii of ~0.0196 μm and ~0.0648 μm, from the α and t, respectively [48]. Those electrons that escape recombination at the ^{6}Li conversion sites along the saturated track and avoid traps within the glass matrix can

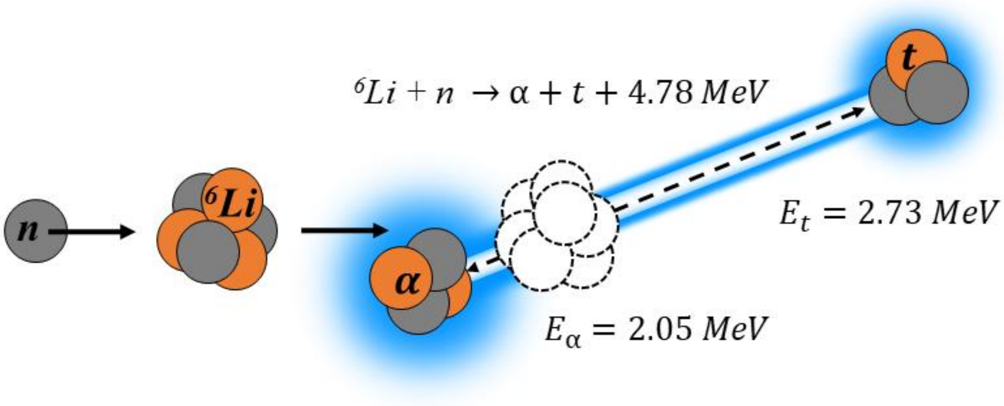

Figure 1-8. Schematic of the reaction between a neutron (n) and a ^{6}Li atom, producing the α and t conversion particles.

induce scintillation by exciting Ce^{3+} centers. Excited Ce^{3+} sites scintillate between 390-420 nm, with a peak at 395 nm wavelength via the available Ce^{3+} $4f \rightarrow 5d$ transition. As mentioned, the near-UV emission of Ce^{3+} is transparent to its own scintillation. So, the probability of excitation and scintillation should increase as the Ce activator concentration within the glass increases, without the typical concentration quenching effects present in a crystal structure. However, the absorption of ceric (tetravalent, Ce^{4+}) ions overlaps both the absorption and emission of cerous (trivalent, Ce^{3+}) ions, resulting in serious quenching effects when ceric ions are present in significant concentration within a glass scintillator. Therefore, strict control of the melting procedure during the scintillator creation is maintained to minimize the concentration of ceric ions.

1.3.2 Light Yield

The processes used to create Li-glass, and the concentrations of its constituents, can be highly variable. Therefore, the precise light yield of a specific Li-glass scintillator is unique to that batch of glass. The light yield of GS20, the most common type of Li-glass, is typically cited as 6,000 photons per thermal neutron capture (ph/n_{th}). This value may underestimate the actual light yield of most Li-glass scintillators. Scintacor Ltd. (Cambridge, United Kingdom), the current owner of the well-recognized GS20® trademark, claims 6,000 ph/n_{th} [49] and cites the work of Spowart from 1969 [50]. Yet, over the last 50 years, significantly larger scintillation light yield values for Li-glass have been reported and cited.

Often references that do not report a measured light yield value instead cite the 6,000 ph/n_{th} value from an indirect source that then cites other sources. This citation cycle often leads back to Spowart's work [50], which actually claims a light yield of 6,700 ph/n_{th}. As an example, consider recent research [51] from 2016 that cites the 6,000 value from a widely cited paper [52] from 2001, which in turn cites a scintillation materials catalog from the former Nuclear Enterprises Ltd [53]. A copy of that catalog from 1990 was unearthed. It was noticed that the value the catalog cited was 6,700 ph/n_{th}, and it was referenced from Spowart [50]. Some modern research directly cites the 50-year-old 6,000 value [54]. Other work has rounded the value up to 7,000 ph/n_{th} [55] [56].

In terms of light yield uncertainties for amorphous scintillators, a 12% rounding error may be acceptable for some applications. However, Spowart went on to empirically determined the total number of ion pairs created following neutron capture, and calculated the effects of recombination, energy transfer to the glass, and luminescence efficiency on the light yield. He revised his light yield estimate to ~7855 ph/n_{th} in 1976 [46]. Referencing experimental results for alpha excited Li-glass [57], Ottonello separately deduced a 8,000 ph/n_{th} light yield [58]. The explicit value and use of light yield within this work will be described in detail in Chapter 4.

1.4 Associated Particle Imaging

Accurate detection and characterization of Special Nuclear Material (SNM) remains a challenging goal as passive signatures characteristic of SNM can be somewhat easily shielded. Sufficient shielding can be used to decrease the Signal-to-Noise Ratio (SNR) of passive signatures to the level of or below that of the natural background radiation. Associated Particle Imaging (API) is an advanced imaging technique that is based on correlating a fast neutron produced by a fusion reaction with an associated particle. Typically this associated particle is an alpha particle. Since neutrons readily penetrate high Z materials, radiographic/tomographic images of shielded objects can be reconstructed by observing the attenuation of transmitted fast neutrons. Thus, active integration using API has been successfully implemented for a variety of security applications, and it has specifically demonstrated the ability to detect SNM in cases where the characteristic passive gamma signatures may be purposefully hidden [59] [60] [61]. Similarly, the progressive application of active API technology, like the Dynamic Albedo of Neutrons (DAN) instrument in operation on the NASA Curiosity with a pulsed neutron generator, has been suggested as a means to boost the SNR for surface based measurements of elemental composition and abundance of water [62][63].

API relies on the kinematics of common fusion reactions to time tag a neutron headed towards an object for interrogation with the detection of an associated particle that is emitted in the opposite direction at the same time. For example, in the case of the Deuterium-Tritium (D-T) reaction, an alpha (the associated particle) and a neutron are emitted back-to-back following fusion:

$${}_{1}^{2}D + {}_{1}^{3}T \rightarrow {}_{2}^{4}He + {}_{0}^{1}n + 17.589 MeV$$

Since the imparted kinetic energies of the alpha and neutron are known to be 3.540 and 14.049 MeV, respectively, the time-of-flight (TOF) of the particles can be calculated. So, if the emitted alpha is detected at a specific time and position with a position-sensitive photosensor, then the associated neutron produced from that fusion event can be time-correlated to that alpha (tagged) and its direction of travel can be estimated. Thus, the neutron transmission information related to the attenuation caused by the density and isotopic composition of an object can be extracted from the measured TOF of tagged neutrons, which are detected in the opposite direction. Figure 1-9 offers an illustration of how such a system may look, and is taken from [64], wherein Cates provides a thorough introduction and detailed explanation of API systems.

One API system, the Thermo-Scientific API 120, utilizes a D-T generator to produce $\sim 2 \times 10^7 n/s$. Inside of its vacuum is a Ce doped Yttrium Aluminium Perovskite (YAP:Ce) scintillator for alpha detection. The spatial and temporal resolution of the embedded YAP detector used to tag the neutrons within the API system is convolved into the resolution of the reconstructed images of the assayed object. Unfortunately, the x-ray background accompanying the D-T neutron production rate has been found to introduce increased uncertainty to alpha particle positioning and timing with the YAP scintillator when the generator is run at full current and flux. Since API depends on fast neutron detection, the achievable reconstructed image resolutions produced are on mm – cm scales, not μm as previously discussed for high resolution imaging of thermal or cold neutrons.

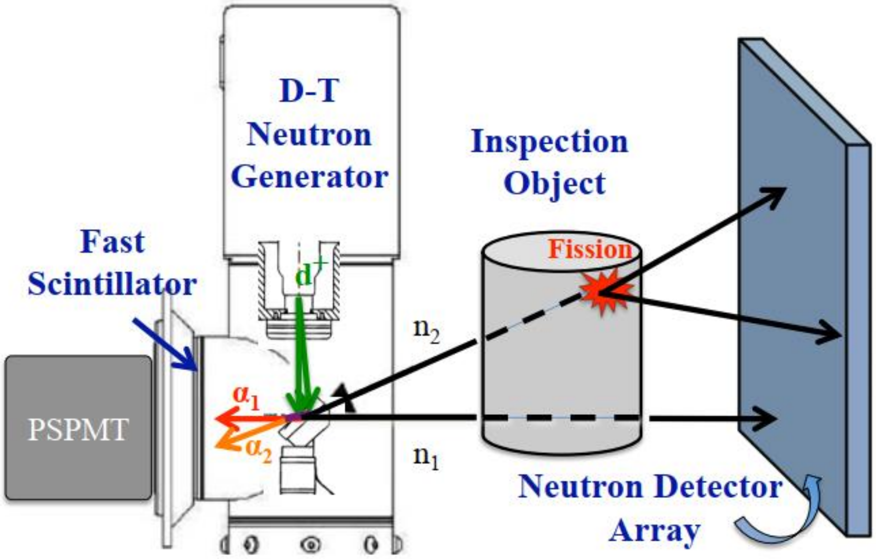

Figure 1-9. Illustration of the associated particle technique using an imaging system based on a D-T neutron generator with an associated particle detector (generator, object, and array not to scale) [64].

1.5 Original Contributions

This section calls out the novel findings of the research and development performed for the doctoral studies within this dissertation. Prior to the research reported for these doctoral studies, work was performed to simulate and develop glass scintillator microfiber arrays. A summary of the significant findings of this previous work are included in the Appendix.

With regard to the neutron imager development, the first of its kind, an all solid multicore SCIFI possessing 7-10 μm diameter Li-glass cores was fabricated at a 70% packing fraction. The $^{6}Li(n,\ \alpha)t$ reaction SCIFI light yield was estimated at $7{,}700 \pm 1{,}000$. Neutron radiographs had an isotropic resolution of ~25 μm of across the faceplate for 375 minutes of exposure. The ultimate resolution of ~16 μm was obtained after applying a FFT filter. At this time, and to the knowledge of the author, this is the best spatial resolution obtained for a Li-glass based neutron imaging device.

With regard to diffusion studies to enable improved neutron imaging, attempts were made to create a near-surface, neutron-sensitive scintillating region of a thicker monolithic glass and an alpha sensitive scintillating region of a thicker single crystal, and the activation energies of Ce within these materials were measured for the first time. The Ce diffusion activation energy within the Li-glass and YAP were found to 4.26 ± 0.55 eV and $1.02\ \pm\ 0.10$ eV, respectively. The valence state of the Ce diffused into the glass was estimated with experimental measurements. Enhanced radiation reduction of the Ce, caused by intense alpha bombardment, was indirectly observed.

1.6 Dissertation Overview

First, the design, fabrication, and evaluation of Li-glass multicore fiber for high resolution thermal neutron imagers is investigated. Initially, developmental trials and neutron/gamma discrimination observations for the initial square-packed, multicore SCIFI design are discussed in Chapter 2. Neutron scintillation in the form of increased integrated charge collection as a function of scintillation fall time is discriminated from background radiation at imaging beamlines. Radiographic images later confirm this finding.

The fabrication process of the proof-of-concept, hexagonal-packed, multicore SCIFI design and an evaluation of its radioluminescence and chemical stability are provided in Chapter 3. It is demonstrated that microstructured optical fiber scintillators have some of the benefits of thicker scintillators that possesses high neutron conversion efficiency, and thinner scintillators that physically bound scintillation photons with good spatial resolution. The scintillating Li-glass cores of the hexagonally packed design have ~8.5 µm diameters and an 11 µm pitch. For this study, a total of 500 m of an all–solid glass composite multicore fiber, at a 70% actively scintillating core packing fraction, is drawn. Luminescence analysis of the Li-glass shows that the glass remains active and scintillates with the characteristic $4f \rightarrow 5d$ transition of the Ce^{3+} activator following fiber drawing. EDS is used to examine the transport of Li absorber and Ce activator from the Li-glass into the multicore cladding. It is inferred from Na transport that the heating cycle for the fiber fabrication is likely driving Li into the cladding. The heavier Ce is directly observed to be immobilized within the cores.

Scintillation characteristics of a SCIFI faceplate are estimated, and ultimate spatial resolution for the current multicore is measured in Chapter 4. Radiographic images later confirmed this finding. The $^{6}Li\ (n,\alpha)\ ^{3}H$ reaction SCIFI light yield is estimated at $7{,}700 \pm 1{,}000$ photons. Neutron radiographs have an isotropic resolution of ~25 µm of across the faceplate for 375 minutes of exposure. An ultimate spatial resolution of ~16 µm is obtained after applying a FFT filter. The microscale architecture of the multicore design may facilitate charged particle tracking on a single neutron capture event basis, where enough light is collected along the ~47 µm ionized track.

Second, diffusion studies to enable improved neutron imaging were conducted. The thermal diffusion of the Ce^{3+} activator into ^{6}Li glass is presented along with its application for fiber optic neutron imaging in Chapter 5. The properties of cerium diffusion are assayed with RBS, and the activation energy of Ce within the silicate is calculated. Radiation-induced color centers form on the diffusion samples as an effect of using the ion beam for these measurements. The valence state of the diffused cerium is then assayed as a function of depth with X-ray Photoelectron Spectroscopy, and the signal from cerium for the color centers is compared to the unirradiated sample surface.

A similar diffusion process is then adopted for use with YAP ($YAlO_3$:Ce) in Chapter 6. The activation energy of Ce diffusion into YAP, resulting polycrystalline phase structure, and optical properties of transmission, and X-ray and α luminescence are investigated. The usefulness towards API is related to inform future synthesis of novel surface scintillating YAP alpha detectors.

Finally, Chapter 7 provides a summary of the conclusions drawn from these investigations, highlights the significance of the work, and provides recommendations for continued research.

Chapter 2

Fabrication of a Square Packed Multicore Fiber for Neutron Imaging

2.1 Abstract

[iii]Optical fibers have been successfully utilized for point sensors targeting physical quantities (stress, strain, rotation, acceleration), chemical compounds (humidity, oil, nitrates, alcohols, DNA) or radiation fields (X-rays, β particles, γ-rays). Similarly, bundles of fibers have been extremely successful in imaging visible wavelengths for medical endoscopy and industrial boroscopy. This work presents the progress in the fabrication and experimental evaluation of multicore fiber as neutron scattering instrumentation designed to detect and image neutrons with micron level spatial resolution.

2.2 Introduction

Optical fibers have found numerous applications in distributed and point sensors aimed at measuring physical measurables (most notably strain, temperature, rotation and acceleration), chemical compounds (ranging from humidity to explosives, combustibles and biological compounds like proteins or DNA) or

---

[iii] Chapter 3 is a reprint of the material as it appears in *25th International Conference on Optical Fiber Sensors IEEE* 2017. A*uthors:* M.E. Moore, X. Zhang, X. Feng, G. Brambilla, J.P. Hayward. The dissertation author was the primary investigator and author of this paper.

radiation fields (X-rays, β particles, γ-rays). As far as the monitoring of heavy charged particles and high energy photons is concerned, detection is often achieved by exploiting scintillation. An incident radiation field enters a glass matrix and generates highly energetic charged particles that dissipate their kinetic energy into the ionization of the matrix atoms. The dissipated energy may be partly transferred to a dopant (typically rare earths, like Ce), which emits scintillation light in the visible/near UV when de-exciting. Scintillation light can then detected and related to the incident radiation by conventional photomultipliers or charged coupled devices (CCDs) [65] [66] [67].

Scintillating glasses have been introduced into fiber cores to provide remote sensing capabilities [68] for a variety of high energy fields including, X-rays, γ-rays and charged particles [69] like protons or α particles. Neutrons represent more of a challenge, as they do not possess charge. Their detection often relies on nuclear absorption reactions that produce charged particles that can then be detected through conventional scintillation processes [70].

In our work, neutrons are detected by exploiting their well-known reaction with ^{6}Li (see Figure 2-1), which generates two charged particles (α and tritium), which can then interact with the scintillating medium. The alpha and tritium particles have a total combined kinetic energy of 4.8 MeV which excites the Ce^{3+} atoms in the glass, which in turn emit light in the 395-432 nm wavelength range. The absorption cross section for ^{6}Li is dependent on the neutron energy, with the highest probabilities at cold/thermal energies.

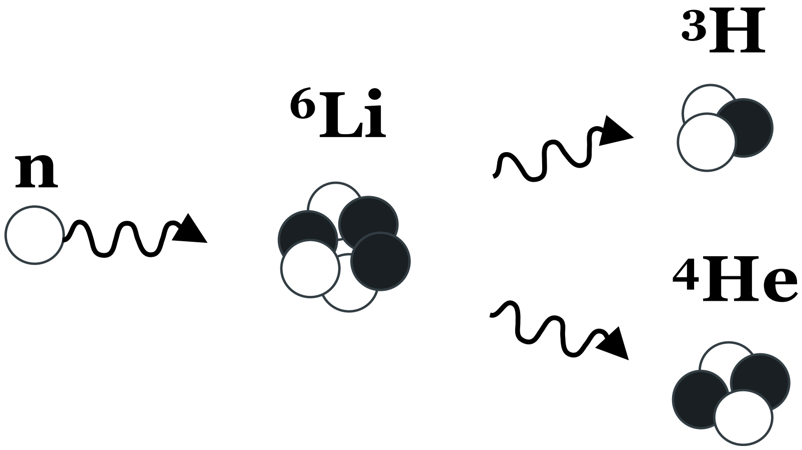

Figure 2-1. Schematic of the reaction between a neutron (n) and a ^{6}Li atom, producing tritium (^{3}H) and an α particle (^{4}He).

Bundles of fibers have been extremely successful in imaging visible wavelengths for medical endoscopy and industrial boroscopy, but the relatively low density of fibers has produced limited neutron imaging capabilities [71]. While high resolution X-ray imaging is able to resolve features at the nanoscale, the state-of-the-art for neutron imaging research is ~15 μm [16]. Here we present the progress in the fabrication of multicore fiber designed to enable high spatial resolution for neutron imaging applications in science and engineering.

2.3 Optical Fiber Fabrication

The multicore optical fiber was fabricated through stacking unit elements composed by Guardian Glass (Nucsafe Inc., Oak Ridge, TN, USA), a scintillating glass, as core and a silicate glass as cladding. The core was doped with isotopically enriched ^{6}Li for the detection of neutrons and Ce^{3+} for scintillation. The cladding had a composition similar to the LLF1 glass (Schott AG, Mainz, Germany). The two glasses were chosen because of their similar thermal properties that allow for co-drawing. The core glass, provided in a cylindrical rod with a diameter of 7.5mm, was inserted into a cladding tube with an external square cross section. The set of core/cladding rod-in-tube was caned to an external diameter of 730μm (Figure 2-2 (a)) at which the core had a diameter of 460 μm. The square cane was then stacked into a square array illustrated in Figure 2-2 (b). The fused array was consolidated in a furnace to produce a monolithic square preform (Figure 2-2 (c)) before being drawn into the fiber. The fiber had a width ranging from 126 μm to 160 μm.

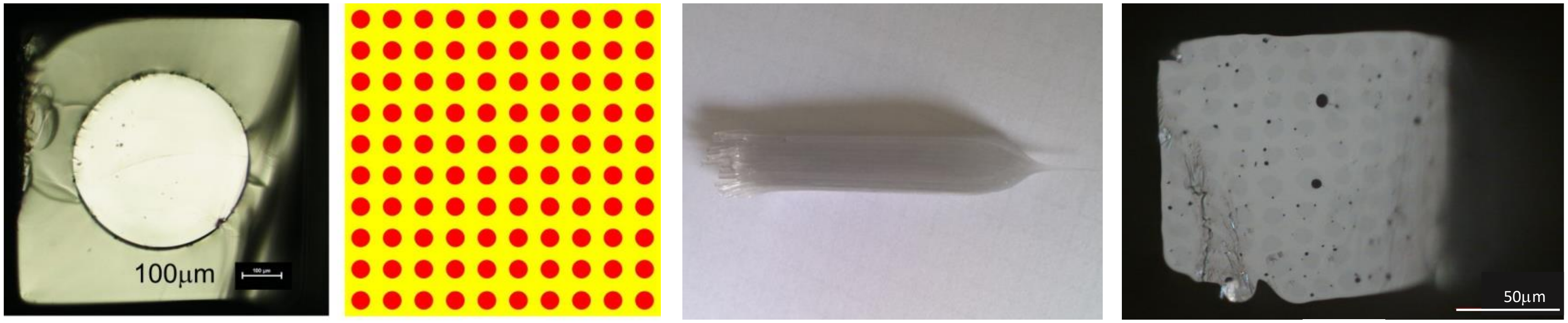

(a) (b) (c) (d)

Figure 2-2. (a) Optical photo of elongated core/cladding square cane. The side length of the cane is 730 µm and the core diameter is 460 µm. (b) Schematic of stack of 10x10 canes before final draw. (c) Photograph of the stack. On the right it is possible to see the neckdown region where the preform is pulled into a fiber. (d) Optical photo of ^{6}Li glass multicore fiber. The fiber width is 140µm, while the core diameter is 7 µm.

Figure 2-2 (d) shows a cross section of the final multicore fiber, which presents a number of microbubbles, resulting from the cavities left in the preform during consolidation. As already observed in other scintillating fibers, the presence of small bubbles is not believed to be detrimental to the fiber operation in that it increases the numerical aperture the fiber cores, thus decreasing the core cross talk. However, uniformity is required for ideal high resolution neutron imaging.

Since a larger field of view was desired with which to detect neutrons, an array of scintillating fibers was produced. In order to create an array of the fiber, it was loaded onto a glass plate with a rigid UV curable epoxy for further processing. The glass plate was then cut into two pieces, stacked together, and the top glass plate ground away. After re-assembly, the new two layer array was then cut in half and re-assembled to produce a four layer array. This process was repeated to create a 64 by 64 array of the fibers with a thickness of 1.7 mm. The array was finished by polishing the surface, cutting the array from the glass, and leaving glass sidewalls in place for support.

2.4 Testing with Thermal Neutrons

To determine how the drawing process has affected the scintillation performance of the Guardian Glass core and to verify that scintillation light is being efficiently channeled with micron-level architecture, the fiber array was assayed with a cold neutron source. Testing was carried out at the High Flux Isotope Reactor's CG-1D beamline at Oak Ridge National Laboratory, Oak Ridge TN, USA. Initially, a nominal background was observed when a calibrated Hamamatsu photomultiplier tube

(PMT) R9779 was placed in the beamline cage without the fiber array. The entire surface of the fiber array was then secured to the PMT window, wrapping it first with Teflon and then black tape. The response of the fiber array to the background (neutron shutter closed), and to the neutron beam (neutron shutter open) was observed. Scintillation was clearly seen for both cases (see Figure 2-3). The response to the neutron beam displays an increased integrated charge distribution. Thus, cold neutrons clearly exhibit a higher light output response than the gamma background radiation present in the beamline.

It was found that the PMT had an integrated charge response to a single photon of 122 ± 60 fC under a bias of -1,500 V. The neutron response yields an approximate photoelectron number of 246 photoelectrons. Previous analysis of a larger monolithic Guardian Glass sample with dimensions of 23.88 mm (diameter) by 2.85 mm (thickness) established that Guardian Glass can be expected to produce ~9,000 photoelectrons per thermal neutron capture [43]. The difference in light output between the two experiments is a result of the difference in scintillator form—monolithic crystal vs. thin fibers—and the small surface area of the scintillator in contact with the PMT window. The Guardian Glass cores in the fiber array had an approximate surface area of 15.7 mm^2, compared to the bulk sample's 447.9 mm^2.

After the PMT measurements confirmed the presence scintillation, a SBIG CCD STF-8300M with a Canon MP-E 65 mm f/2.8 1-5x lens was focused to the mirrored fiber array. Since the emission wavelength of Ce^{3+} is in the 395–432 nm wavelength range, focusing was accomplished using blue light, which has a 450–495 nm wavelength

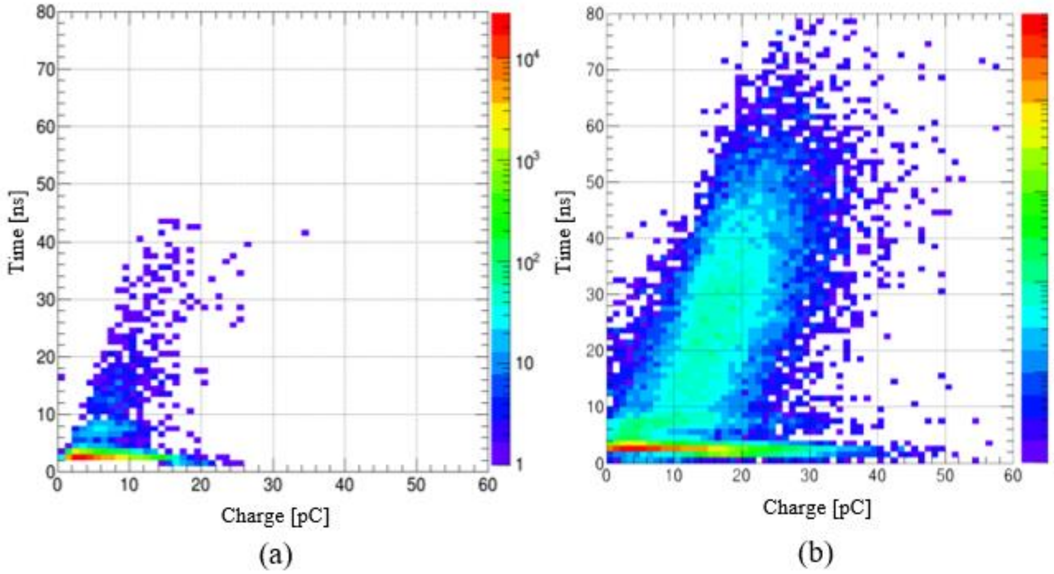

Figure 2-3. PMT response to the presence of scintillation in the fiber array at CG-1D to (a) background radiation, in the beamline, and (b) the neutron beam.

range. From the blue light image, an absolute system resolution was obtained by measuring the line spread function. By analyzing the epoxy bond gaps of the glass plating in several locations, it was determined that the ultimate resolution of the setup was approximately 10 μm at 8% contrast.

Without changing the focus of the system, 91 images with 600 s exposure times were taken in the neutron beam. A cadmium-coated edge was placed in the path of the neutron beam to observe the edge response (see Figure 2-4). These images were processed so bright outliers of 50 gray count and above are replaced by the median of the pixels in the surrounding area for each image to remove cosmics and gamma-rays that interacted directly with the Multi-Channel Plate (MCP) and the CCD device itself. Then all runs were stacked with a median filter which again reduces noise in the active image by replacing each pixel with the median of the neighboring pixel values. Twelve images with 600 s exposure times were taken with the system with no neutron beam (shutter closed) for a total of 2 hours. This background data was handled with a median filter after removing outliers as done previously, and normalized to 600 s of beam time. The background image was subtracted from the neutron beam image to produce an image of the neutron light without inherent bias and dark noise from the CCD. While the response to the cadmium coated edge does further demonstrate the sensitivity of the fiber array to cold neutrons, unfortunately, the edge was not thick enough or close enough to the fiber array to allow for a resolution measurement of the scintillation light.

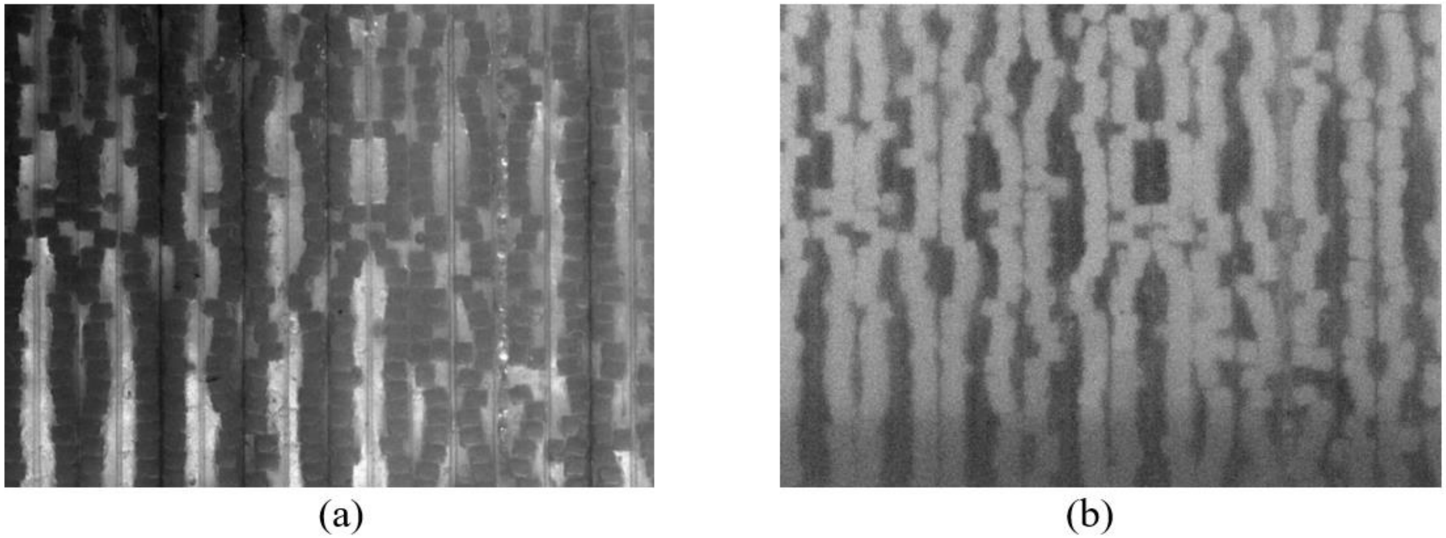
(a) (b)

Figure 2-4. (a) Blue light image of the scintillating fiber array with 10 µm resolution, (b) Processed scintillation light image of the array normalized to an exposure time of 600 s, less scintillation light can be seen on the bottom of the image. This shadow was caused by the attenuation of the cold neutrons by the cadmium coated edge.

2.5 Future Work and Conclusions

Using lessons learned from the measurements at CG-1D, we are working on a new design and improved characterization setup. We are creating a new generation of microfiber with improved packing fraction of cores, ~40%, and a higher NA value, ~0.44. Additionally, we are characterizing an Intensified CCD coupled to a UV sensitive optical system, stationed on a negative stiffness vibration isolator, capable of resolving μm features. At 10% of the Modulation Transfer Function (MTF), the resolvable spatial frequency is ~3.3 cycles/μm with blue light.

Chapter 3

Characterizing a Proof-Of-Concept Hexagonal Packed Multicore Fiber Neutron Imager

3.1 Abstract

[iv]This work presents the fabrication and experimental evaluation of instrumentation designed to enable higher spatial resolution neutron radiography for those performing research at neutron scattering facilities. Herein, we describe a proof-of-concept array of microstructured silicate fibers with ^{6}Li doped cores that shows progress towards a design for μm resolution neutron radiography. The multicore fiber was fabricated by drawing stacked unit elements of Guardian Glass (Nucsafe Inc., Oak Ridge, TN, USA), a ^{6}Li scintillating core glass, and a silicate cladding glass. These structured fibers function as an array of sub-10-μm waveguides for scintillation light. Measurements have shown a significantly increased integrated charge distribution in response to neutrons, and the spatial resolution of the radiographs is described by edge response and line spread functions of 48 ± 4 μm and 59 ± 8 μm, respectively.

[iv] Chapter 5 is a reprint of the material as it appears in *Nuclear Inst. and Methods in Physics Research, A* 2018. A*uthors:* M.E. Moore, J. Lousteau, P. Trtik, H.Z. Bilheux, D. Pugliese, D. Milanese, A.T. Simone, G. Brambilla, J.P. Hayward. The dissertation author was the primary investigator and author of this paper.

3.2 Introduction

The properties of novel X-ray opaque materials, like those used in energy storage systems, precision manufacturing technologies, aerospace components, and metallic additive manufacturing, are often described using simulation tools lacking experimentally grounded models, and are based on first-principle calculations and theoretical assumptions alone. Thus, ongoing material characterization relies on neutron scattering instrumentation to verify performance predictions and add structure to future models. Despite the successes that neutron scattering science facilities have achieved in recent years, even higher-impact research into microstructure evolution, thermodynamic, and mechanical properties of advanced materials is sometimes limited by the current spatial resolution of neutron sensing instrumentation.

Recent improvements in neutron sensing instrumentation have enabled a few modern neutron scattering facilities to reach the current state-of-the-art spatial resolution of approximately 10-25 μm [15]. However, progress towards μm resolution remains a challenging goal for the neutron imaging community for two primary reasons.

Firstly, thermal neutron fluxes at even the most novel user facilities are much lower than similar X-ray imaging sources. For example, the raw power of several tens of W/cm^2 is regularly reported at advanced X-ray sources like Advanced Photon Source (APS) at Argonne National Laboratory. This power corresponds to a range of fluxes that conservatively start several orders of magnitude greater than the estimated novel thermal neutron flux of approximately $1.2 \times 10^9\ n/s/cm^2$ at the ODIN neutron imaging beamline planned at the European Spallation Source (ESS) [33].

Secondly, the efficiency of thermal neutron sensitive scintillators is in competition with the spatial resolution. Thick scintillators (mm scale) have higher efficiencies and, therefore, can produce high contrast radiographs in less time than thin scintillators (μm scale). However, a thick scintillator will have poor spatial resolution, as the position of captured neutrons is smeared throughout the scintillating volume. Conversely, thin scintillating screens and films bypass spatial resolution smearing by reducing the thickness of scintillating medium at the cost of efficiency. Still, the spatial resolution of unstructured thin scintillators is fundamentally limited by the variance introduced by the difference in track orientations of the charged particles emitted from neutron captures and the succeeding isotropic emission of scintillation light from neutron converters such as $^{6}\mathrm{Li}(n,\ ^{3}H)$, $^{10}\mathrm{B}(n,\alpha)$, and $^{157}\mathrm{Gd}(n,\gamma)$. Thus, there is a clear need to marry the benefits of high efficiency and spatial resolution while also overcoming the neutron capture position uncertainty that results from charged particle track variance. Some of our prior work based upon Monte Carlo simulation suggests that tracking these charged particles on an event-by-event basis could allow one to overcome this limiting uncertainty [15] [43].

Not long after the seminal work on neutron scintillating glasses [46] was published, scintillating fiber optic glass faceplates were being researched for particle tracking applications in high energy physics experiments in 1983 [72]. Three years later, the first results of a neutron scintillating fiber (SCIFI) tracker were reported [73]. In

1994, the first neutron radiograph, of a pierced sheet of Gd, taken using a SCIFI array was published with resolvable features on the order of several 100s of μm [58]. Since that time, SCIFIs have been researched for remote radiation dosimetry and neutron sensitive fusion applications [67] [68] [69]. More recently, interest surrounding coupling optical fiber tapers to existing scintillator based neutron imaging setups has grown with novel 11 μm resolution results [74]. However, in the last 24 years, it appears that no work has been done to build upon the original concept of the SCIFI tracker.

We propose the use of microstructured scintillating optical fiber arrays, capable of heavy charged particle (HCP) tracking via waveguiding scintillation light following neutron capture, for high resolution neutron imaging. Specifically, we utilize the well-known capture reaction for Li-glass ^{6}Li (n, α), emitting alpha (α) and triton $({}^3H)$ particles back-to-back that ionize primary and secondary electrons, exciting a Ce^{3+} activator, which in turn emits scintillation light at 395-432 nm in the near-UV/visible wavelength range. This light is transported through the neutron sensitive microstructured waveguides and is observed by a photodetector, see Figure 3-1. Provided that the collected and converted light has a sufficient signal to noise ratio (SNR), one should be able to observe the tracks of these particles and precisely estimate the locations of neutron capture reactions [43].

In our first generation proof-of-concept array, we attempted to use air capillaries in the cladding layer to maximize the refractive index difference between the Li-doped glass core and the cladding. While the lead oxide cladding glass was mechanically

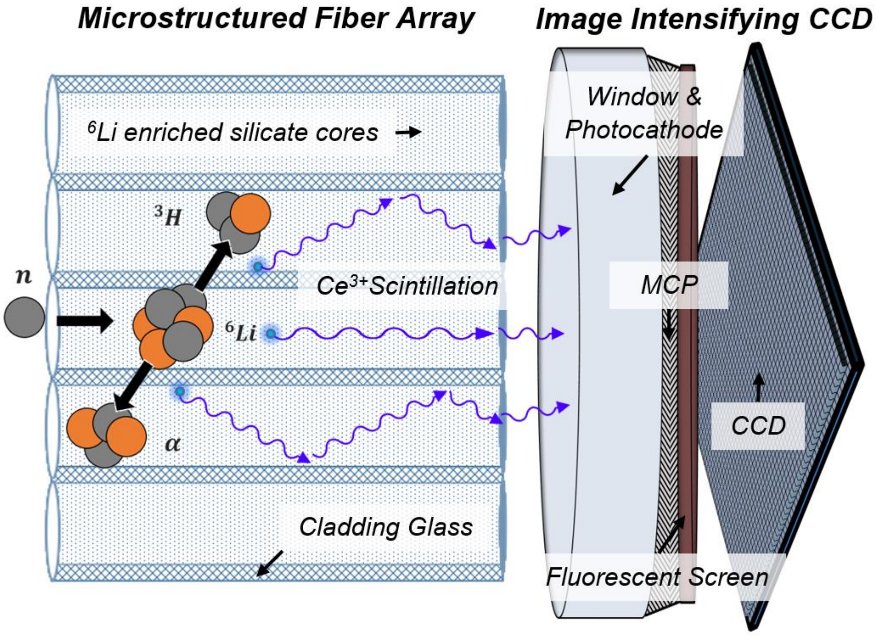

Figure 3-1. Enriched lithium-6 glass fibers that are doped with cerium absorb thermal neutrons, emit scintillation light, and act as optical waveguides to channel the scintillation light for imaging. They are surrounded by a cladding of lower refractive index. While an image intensifying CCD is our selected choice for a photosensor in this proof-of-concept study, it is possible that a different photosensor may be more appropriate in order to scale to a larger area.

compatible with the Li core glass, the air capillaries tended to collapse, so we moved to an all-solid glass design. With the all-solid design, we have made several attempts to better match the thermal fiber pulling properties with the optical properties to achieve the best active scintillating volume and refractive index difference insofar as possible. This work describes the fabrication and characterization of this next generation, proof-of-concept neutron SCIFI tracker.

3.3 Fabrication

To fabricate the neutron SCIFI, a multicore design was used. A rod of ^{6}Li-loaded glass with properties similar to GS20 [46] (fabricated by Nucsafe Inc., Oak Ridge, TN, USA) was inserted in an extruded optical glass cladding tube. Canes of Li-glass cores, embedded in the optical cladding glass, were drawn and then stacked into an array of some geometry. This array of canes, the preform, was pulled into a single multicore fiber. For this neutron SCIFI to act as a successful waveguide, the refractive index of the core, n_{co}, must be larger than the cladding refractive index, n_{cl}. While Li-glass has $n_{co} = 1.55$, a desirable cladding candidate should have $n_{cl} \leq 1.5$ [73]. Additionally, to create a uniform and regular microstructure, the glass viscosities must be matched for fiber drawing. Previous trials of ours have led to a better understanding of difficulties associated with matching both optical and thermal properties of glass fiber while maintaining the chemical stability required for scintillation. An early attempt to create a square multicore neutron SCIFI, described in detail in [74], yielded an irregular array of cores that had a refractive index almost equal to the chosen cladding. Although drawing was possible, issues related to glass devitrification during fiber pulling significantly decreased the fiber guiding properties, undermining the neutron resolution. Alternatively, the N-FK5 SCHOTT glass makes a more attractive cladding glass with an n_{cl} equal to 1.5 and a seemingly compatible transition temperature, (T_g). However, our initial canes of Li-glass and N-FK5 crystallized during drawing due to an incompatible codrawing temperature for the glass viscosities.

The fabrication of our current multicore fiber began with the extrusion of an N-KF9 cladding tube. A cylindrical glass billet with a 29 mm diameter and 35 mm height and a stainless steel die was used during the extrusion process. A 4 kN force was applied to the die and the glass billet while the glass was held in a furnace at an onset temperature of 650°C (true glass temperature of 620°C). Some metallic inclusions were observed inside the extruded glass. Next, the Li-glass rod (11.7 mm diameter) was inserted into a 100 mm long section of the extruded N-KF9 tube, and drawn using the preform drawing method. To determine the optimal drawing temperature, the Li-doped silicate glass, T_g, was experimentally established with differential scanning calorimetry (Netzsch DSC STA 449 F1 JUPITER). The measurement was carried out with a heating rate of 5°C/min up to 1300°C in sealed Pt/Rh pans using ~ 30 mg of fine grain sample, providing a value of $T_g = 470 \pm 3$°C. So, the fiber drawing took place at a furnace onset temperature of 800 °C (730 ±10°C glass temperature) under a flow of N_2 at 2 l/min. The preform was fed into the furnace at a speed of 1 mm/min, and the fiber was drawn at a speed of 5.4 m/min under a tension of 15 g. About 500 m of fiber were drawn from the preform, resulting in a fiber with an outer diameter and a core diameter of 185 ±4 μm and 150 ±4 μm, respectively.

The fiber was then cut into 2,700 separate 120-mm-long pieces and stacked as a hexagonal array. This array was then thermally consolidated into a single unit at 640°C and the N-KF9 tube (13 ±0.2 mm OD/ 11.4 ±0.2 mm ID), used to jacket the Li-glass cores, was extruded under the same conditions previously described for the outer cladding tube. The resulting preform was then drawn into a single multicore fiber 910 ±10 μm in diameter with individual cores possessing 7–10 μm diameters, see Figure 3-2. The hexagonal circle packing geometry allows for the highest fill fraction (active scintillating volume) of circles (cores) to remaining space (cladding), $\frac{\pi\sqrt{3}}{6} \approx 90.7\%$, provided the pitch of cores is equal to the diameter of the cores. Given a conservative estimate of the average cladding spacing between cores of ~2 μm, we estimate that the active scintillating volume of our hexagonal multicore structure is ≈ 70%. Thus, we have found that this multicore design enables uniform core spacing at a 70% active volume, while also allowing for sub-10-μm individual core dimensions.

3.4 Experimental Evaluation

Following fiber drawing, it is necessary to establish that our neutron SCIFI still scintillates as expected. Thus, the radioluminescence emission spectrum of an unpolished Li-glass rod, used for the core glass, was measured for an *On Side* (diameter) and an *On End* (length) case. The diameter of the unpolished Li glass rod

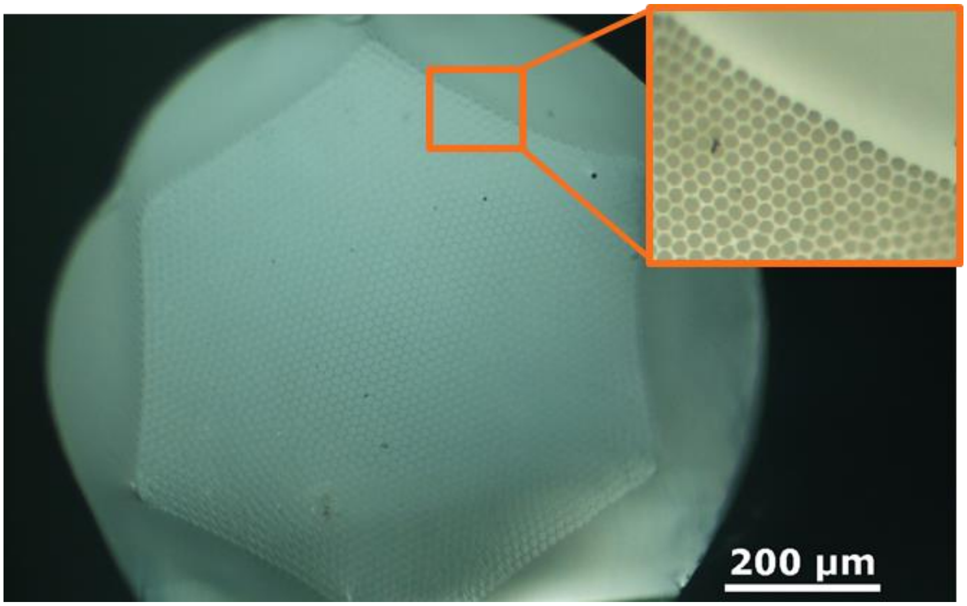

Figure 3-2. Photographed cross section of a cleaved end of a single multicore SCIFI (hexagonal) inside of its outer jacket (round).

was 10 mm with a length of 150 mm. A standard emission peak of Ce^{3+} scintillation light near to the 395 nm peak emission was observed for the *On Side* case, see Figure 3-3. For the *On End* case, the emission peak contracted 15 nm in the near-UV region. Here, the self-absorption effects of the overlapping Ce^{3+} and Ce^{4+} emission and absorption bands are observed when the scintillation light is transported further for the *On End* case. In Figure 3-3, these unpolished rod results are compared to the arrays of multicore SCIFIs, with and without the outer jacket removed; refer back to Figure 3-2 for an image of a single multicore fiber possessing an outer jacket. The SCIFI arrays were 1 mm thick with a 5 x 5 mm surface. The SCIFI arrays were measured on end, as a faceplate. After undergoing the aforementioned heat processing, the SCIFI emission behaves as expected for Ce^{3+} scintillation. The SCIFI had a slightly broadened emission, 3-5 nm, compared to the *On Side* case for the Li-glass rod.

Having verified that the scintillation mechanism is behaving as expected, it is essential to characterize any transport of the Ce activator from the core to the cladding via thermal diffusion to ensure that scintillation light is being produced within the core glass. So, Energy Dispersive X-ray Spectrometry (EDS) was used to examine the atomic concentrations of dopants in cane cross-sections with a Zeiss EVO MA15 Scanning Electron Microscope. The canes of the Li-glass cores cladded with N-KF9 were embedded in epoxy, and EDS line scans were acquired across the ends of the canes. The results of the EDS line scans are shown in Figure 3-4, where Mg inside of the core glass can be seen as the boundary between the core and cladding. No

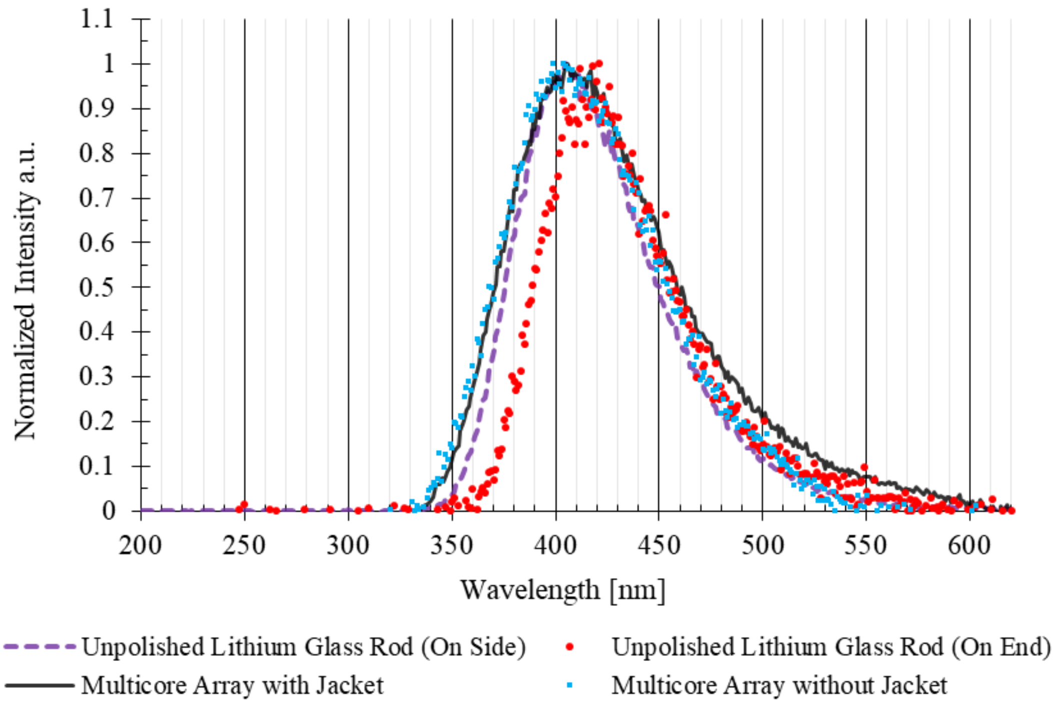

Figure 3-3. Radioluminescence spectra characteristic of Ce^{3+} activator emission for the unpolished ^{6}Li glass rod (unprocessed) and the multicore arrays (drawn into fibers) with and without outer jackets.

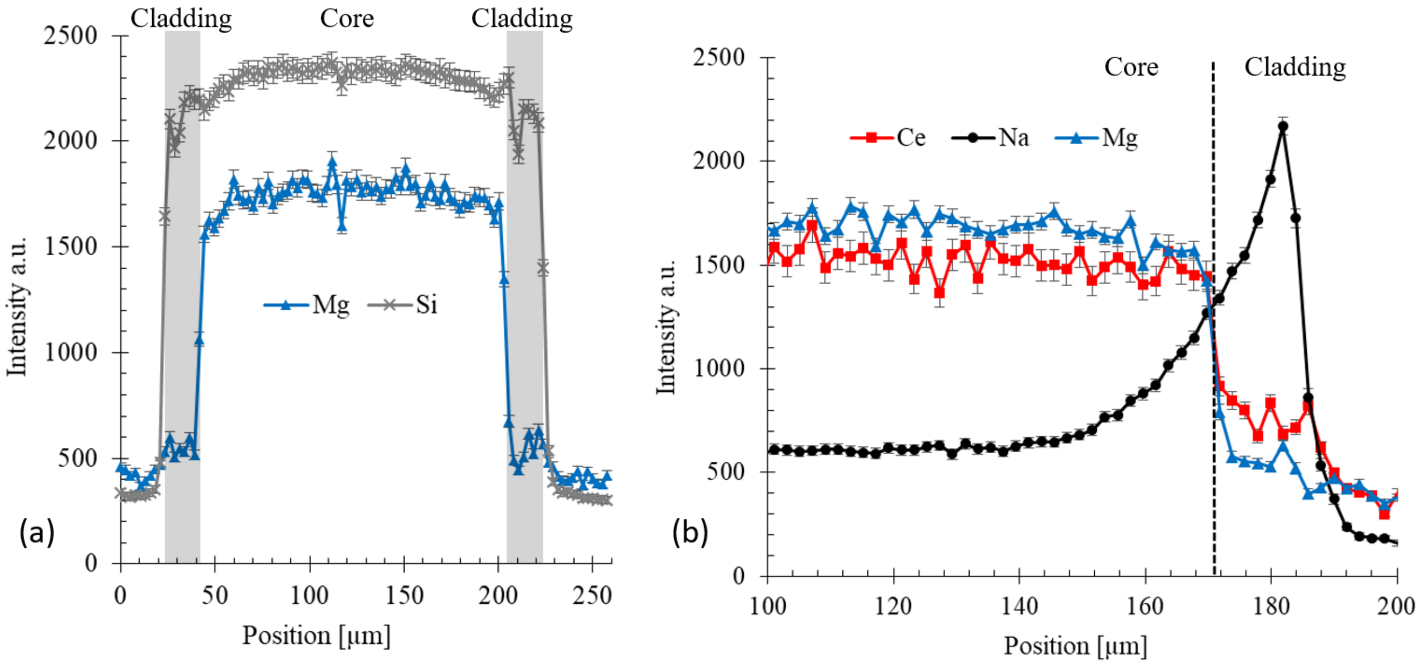

Figure 3-4. (a) EDS line scan across the entire cane where the core (Mg) and core/cladding (Si) components can be seen, and (b) spectra of the core-cladding interface for Mg, Ce, and Na.

decrease, below standard deviation, for the Ce concentration in Li-glass cores at the near-cladding position was observed. EDS point scans targeting 4 randomly selected Li-glass cores, at 3 positions each, correctly detected a Ce concentration of 2.4 $\pm$0.2 wt.%. No Ce was detected when point scans targeted the cladding with a lower detectable limit set to 0.1 wt.%. So, the intensity of the Ce concentration in the cladding and surrounding epoxy is assumed to be background. Thus, Ce was well bound within the core glass during fiber drawing. Again, the fiber was drawn at a 730 $\pm$10°C glass temperature, 260°C above T_g, with any given segment of fiber experiencing approximately 10 min of heating. Previous work of ours has shown that the mobility of Ce in Li-glass, heated at temperatures between 500-600°C for 5 hr with a subsequent 24 hr anneal, resulted in a few μm of Ce diffusion [76]. Thus, the quasi-immobilization of Ce for the short heating duration agrees with our experimental data.

If a significant quantity of the ^{6}Li absorber is in the SCIFI cladding, then neutron captures in the cladding could decrease overall light output, and potentially create $\pm$ 3 μm position smearing. So, it useful to know how the ^{6}Li absorber is diffusing within the multicore. However, EDS systems are fundamentally insensitive to atomic numbers < 5 due to the absorption of low energy X-rays within the detection window. X-Ray Photoelectron Spectroscopy could be used to search for Li in the cladding, but it would not provide an accurate concentration depth profile. Such a technique would require micron scale accuracy when removing core from cladding, and while probing the depth of the cladding. Instead, the mobility of another alkali metal, Na, is particularly interesting because of its chemical similarity, comparable ionic radius, and mobility to the Li absorber in the core glass. The diffusion of Na within Li enriched silicate, ^{7}Li/^{6}Li $= 0.04526$, and Na self-diffusion within 0.33 Na_2O, 0.67 SiO_2 glass has been shown to be closely comparable [77][78]. Additionally, more recent analysis indicates that the activation energy for Li diffusion remains comparable to Na, specifically inside of aluminosilicate glasses; where mixed alkali effects will not immobilize Li or Na [79][80]. The self-diffusion of Na within the cladding glass and its diffusion of 30 ± 4 μm into the core can be clearly seen in Figure 3-4. Although the EDS line scan intensities do not represent relative concentrations between elements, the Li absorber is very likely diffusing in a similar manner to Na from the core into the cladding.

Preliminary studies on gamma/neutron discrimination performance of the Li-glass within the previous square multicore SCIFI described in [74], were conducted at the CG-1D neutron imaging beamline at the High Flux Isotope Reactor (HFIR) at Oak Ridge National Laboratory (ORNL) [81]. The response of the previous square multicore SCIFI array to background radiation (cold neutron flux $< 1 \times 10^1\ n/s/cm^2$ at target with neutron shutter closed), and to the neutron beam (cold neutron flux at $\sim 1 \times 10^7\ n/s/cm^2$ at target with neutron shutter open) was observed with an R9779 PMT. The scintillation light was separable from electronic noise or Cherenkov light generated in the PMT window, both in magnitude (integrated charge) and fall time, where the longer fall times are characteristic of scintillation caused by the Ce^{3+} dopant. While scintillation was clearly seen for both cases, the response to the neutron beam displayed an increased integrated charge distribution as the array exhibited a higher light output response to cold neutrons than the gamma background radiation present in the beamline. Due to the low effective active scintillating volume of the previous square packing used (~27%), the majority of energy deposited in the multicore from the charged particles was not producing scintillation light. The current hexagonal design allows for nearly triple the amount of energy to be deposited into the scintillating core glass.

Radiographs were taken with the current hexagonal multicore fibers using the Swiss Spallation Neutron Source at the Paul Scherrer Institut (PSI). Images were acquired with the Neutron Microscope (NM) at the Pulse OverLap DIffractometer (POLDI) beamline. The use of the NM at the POLDI beamline was uniquely desired due to the requirements of the optical system needed for this experiment. Specifically, the NM possesses the magnification and numeric aperture to enable a nominal pixel size of acquired images of 1.3 μm, and a true spatial resolution of about 5 μm [82]. Additionally, the optics have μm-level repeatable positioning, and are sensitive to near UV Ce scintillation. Using the NM at the POLDI beamline is also beneficial due to a lower gamma background compared with other beamlines, a thermal/cold neutron spectrum from 1.1– 5 Å, and a flux at the sample position of $6 \times 10^6\ n/s/cm^2$ [83].

A diffused, blue light source was used to optically focus onto the ends of hand-cleaved and polished single multicore fibers. Al tape was then used to enclose the scintillator. Open Beam (OB) images were taken to focus the optics to the scintillation light. A quantity of 20 images with 300 s exposures were acquired of the OB. A gadolinium-based Siemens Star (SS) [84] was then positioned in front of the active area of the scintillator and imaged.

Eighty (80) images of the SS with 300 s exposure were acquired. Due to decreased thermal neutron flux, 2 OB and 11 SS images were removed prior to post processing. The remaining SS images, with outliers removed, were divided by the OB background, and summed. The resultant image was transformed with a bilinear clockwise rotation of 90° for analysis. The resolvable spokes of the SS can be seen in Figure 3-5. The resolution of the 2 mm fiber can be estimated via inspection of the highlighted region of the SS spokes possessing approximately 50 μm spatial features. Referencing the 10% to 90% contrast transition for the Edge Response Function (ERF) of the spoke in the highlighted region, a 48 ± 4 μm resolution was found. Fitting a Gaussian to the Line Spread Function (LSF) of the same region, a FWHM measurement yields 59 ± 8 μm spatial resolution.

3.5 Conclusions and Future Work

Li-glass cores with 7-10 μm diameter have been drawn into 500 m of an all-solid glass composite, multicore fiber at a 70% packing fraction. The Li-glass remains active and scintillates as expected following drawing. The Li absorber shows some diffusion into the cladding, but the Ce activator is largely bound during the fabrication process. Hand-cleaved and polished single fibers of lengths 2-5 mm have resolved features on the order of 10s of μm while utilizing the Neutron Microscope. Ideal light collection in these same fibers should allow for ≤ 20 μm resolution. To increase

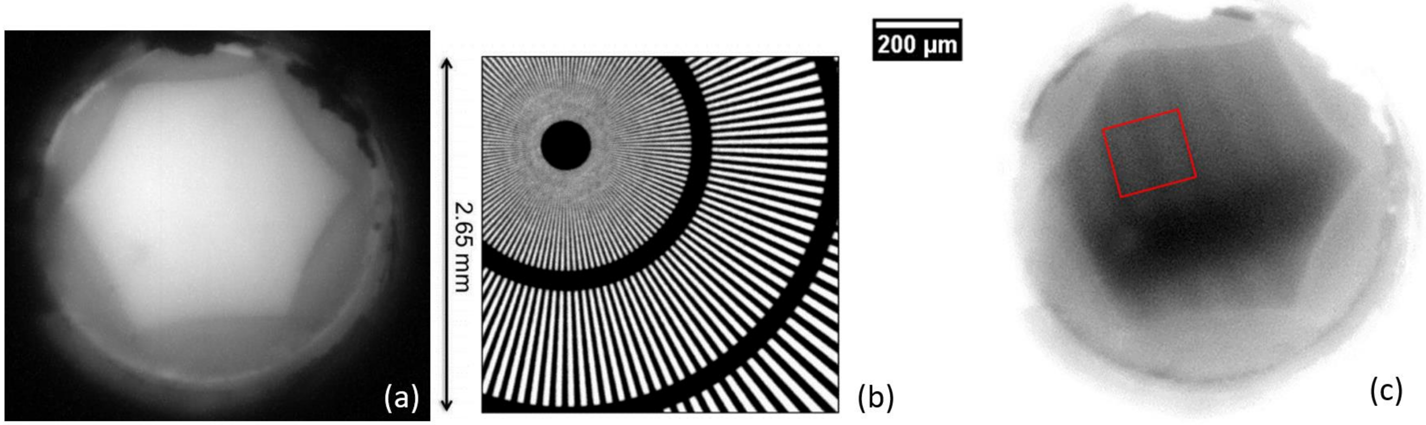

Figure 3-5. (a) OB neutron radiograph taken with a 2 mm thick multicore neutron SCIFI, (b) visual test object reference, PSI's Gd SS taken with the NM in [81], and (c) neutron radiograph of the SS acquired after aforementioned post processing, with the region of interest highlighted.

spatial resolution, the core glass must be drawn to smaller sizes which should be possible with the current fabrication process. Image contrast improvement requires the use of a lower refractive index cladding material. Moreover, fabrication without an outer cladding jacket will allow for easy array assembly.

Near term work is planned to evaluate the radiographic spatial resolution of an array of 100 multicore neutron SCIFIs with a 5 x 5mm field-of-view. This is a comparably thinner design (1mm thick), with outer jacket removed, and it has a well-polished surface. Since a larger field-of-view was desired for evaluation of imaging performance, the multicore fiber outer jacket was ground away, and a 10×10 array was stacked together. Assembly was finished by securing the array with structural glass plate siding and polishing the surfaces, see Figure 3-6.

Meanwhile, a novel phosphate glass cladding, possessing a refractive index of $n_c < 1.53$, is being used for another neutron SCIFI fabrication. This cladding is expected to allow for more than twice the current amount of scintillation light to remain internally bound. We plan to draw the multicore fiber using the phosphate cladding with a goal of 2 μm diameter Li-glass cores while remaining at a packing fraction $\geq 70\%$.

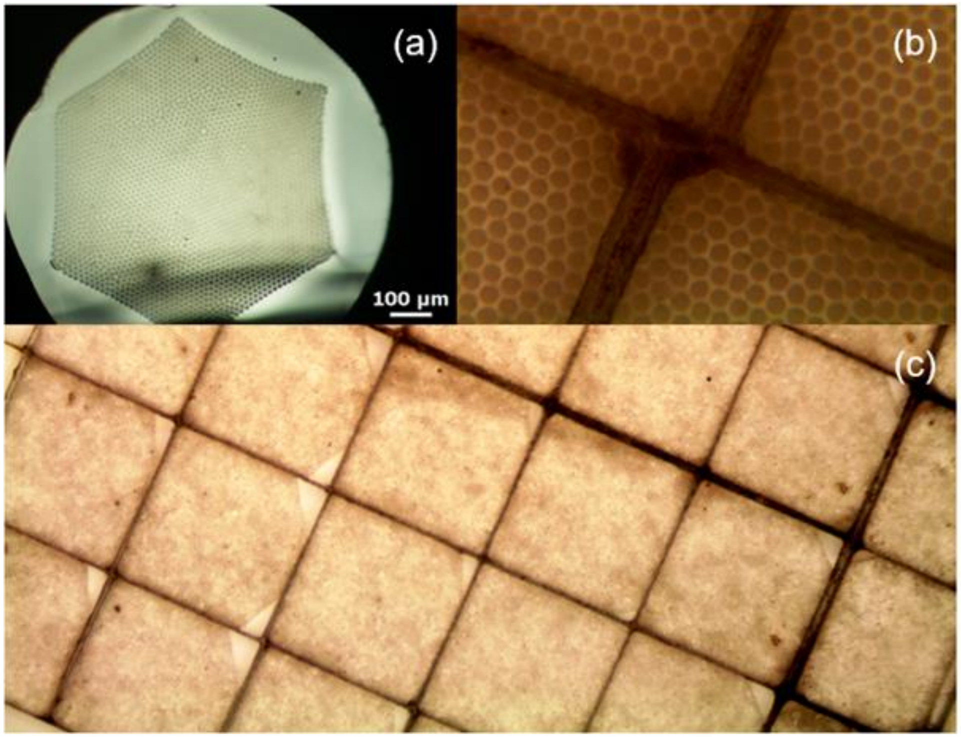

Figure 3-6. Microscope photos of the (a) cross section of a microstructured multicore fiber with scale, (b) stacked multicore fibers with outer cladding removed with 8 ± 1 μm core diameters, and (c) polished faceplate surface of a multicore SCIFI array with 0.5 x 0.5 mm pixels

Chapter 4

High Spatial Resolution Neutron Imaging with SCIFI Faceplate

4.1 Abstract

[v]The improvement of neutron imaging towards and beyond the microscale is a well-documented need for the iterative characterization and modeling of numerous microstructured X-ray opaque materials. This work presents the recent progress in evaluating a SCIntillating FIber (SCIFI) proof-of-concept towards micron-level thermal neutron radiography. These SCIFIs are composed of ^{6}Li-enriched silicate glass cores doped with a Ce activator. The cores possess ~8.5 μm diameters and ~10 μm pitch following fiber drawing with a cladding glass into an all-solid multicore fiber. A polished 5 mm × 5 mm array of 100 microstructured multicore SCIFI pixels was fabricated into a 1 mm thick faceplate. The neutron efficiency and light yield of the faceplate are characterized as functions of the 7.38 weight percent of Li_2O, thickness, and the 70% active volume. It was determined that approximately 39% of a thermal neutron (2 Å) beam can be absorbed by the faceplate. The $^6Li(n,\alpha)t$ reaction is estimated to produce 7,700 $\pm$ 1,000 scintillation photons per event, referencing light collection from ^{241}Am irradiation of the faceplate. Simulations

---

[v] Chapter 6 has been submitted to a peer-reviewed journal for publication of the material. A*uthors:* M.E. Moore, P. Trtik, J. Lousteau, D. Pugliese, G. Brambilla, J.P. Hayward. The dissertation author was the primary investigator and author of this paper.

suggest that on average 17.5 ± 1.4% of these photons will be transported to an end of the fiber array for a thermal beam, with at least 7.2% of that total scintillation light being confined into the fiber cores in which it originated. The SCIFI faceplate was integrated into the Neutron Microscope (NM) at the Pulse OverLap DIffractometer (POLDI) beamline located at the Paul Scherrer Institut to image a Siemens star test object. Processed neutron radiographs acquired with the proof-of-concept faceplate resolved features at a state-of-the-art resolution of 16.1 ± 0.5 μm. The potential for even high resolution designs having smaller pitch or different cladding material is discussed.

4.2 Introduction

The current thrust to improve neutron imaging resolutions towards and beyond the microscale is motivated by the need to support advance neutron scattering facility users in the characterization and modeling of a growing list of novel, microstructured, X-ray opaque materials [4] [9]. For example, high resolution neutron imaging supports models of diffusion-based Li transport and crystallographic texture control of metallographic surfaces for the flourishing fields of advanced energy storage and additive manufacturing [27] [85]. Incremental improvement for neutron imaging for related applications over the past 2 decades stems from the realization that the spatial resolution of unstructured neutron imagers is fundamentally limited by the variance introduced by charged particles emitted from neutron conversion. Focused development of structured neutron position sensitive detectors, such as patterned powder converter screens and microchannel plates (MCP) accompanied by post processing techniques, like event centroiding, sought to overcome this limitation. Nowadays, advanced neutron scattering facilities are able to resolve features on the order of 10 - 20 μm with the use of state-of-the-art neutron imaging instrumentation [15] [74] [86]. Yet, continued progress towards micron level imaging remains a challenging goal as the intensity and linearity of thermal neutron fluxes limits radiographic spatial resolution compared to X-ray sources.

In order to increase neutron detection efficiency while improving spatial resolution, we have revitalized the use of SCIntillating FIber (SCIFI) as neutron imagers, and potentially, as neutron conversion charged particle trackers. The SCIFIs are fabricated with the rod-in-tube fiber drawing technique. A Ce doped ^{6}Li enriched silicate glass (Nucsafe Inc., Oak Ridge, TN, USA) that is chemically similar to the well-known GS20 glass is used as the core, and the SCHOTT glass N-KF9 as cladding. These ^{6}Li glass cores have an approximate 8.5 μm diameter and 10 μm pitch following fiber drawing into an all-solid multicore fiber at the University of Southampton's Optoelectronics Research Centre. Nearly 2,700 scintillating ^{6}Li glass cores are contained inside of 1 multicore fiber with a 70% packing fraction inside of the multicore fiber jacket.

Our SCIFI-based neutron radiography relies on thermal neutron attenuation with enriched ^{6}Li. The neutron efficiency and subsequent light yield are functions of the 7.38 weight percent Li_2O as well as the active scintillating volume of glass, and the molar concentration of its constituents. Following thermal neutron absorption on ^{6}Li, an alpha and triton are emitted back-to-back in the $^6Li(n,\alpha)t$. For our glass, the track length of the α is ~7 μm and for the t it is ~40 μm [46]. These track lengths are comparable to those found using SRIM-2013 [47] with the composition of aluminosilicate glass defined for GS20 as reported by [46], with the addition of 6.941 weight (amu) of Li, and a compound density of 2.5 g/cm^3. The resulting ionized primary and secondary electrons diffuse through the composite glass matrix with cylindrical radii of ~0.0196 μm and ~0.0648 μm, from the α and t, respectively [48]. Those electrons that escape recombination at the ^{6}Li conversion sites along the saturated track and avoid traps within the glass matrix can induce scintillation by exciting Ce^{3+} centers in the glass cores. Several cores may be partially activated these electrons along the charged particle tracks. The Ce^{3+} emission peak within ^{6}Li-glass is centered at λ ~ 395 nm. The near-UV scintillation is then emitted isotopically into 4π where angle-dependent-refraction totally bounds a percentage of light within the SCIFI. The bound light and the light that is transmitted to the neighboring cores and cladding are then transported to an exit surface of the multicore SCIFI to be read out by an optical system and a camera/CCD/CMOS, illustrated in [87]. A well-polished 5 x 5 mm array of 100 microstructured multicore SCIFI pixels was fabricated into a 1 mm thick faceplate, see Figure 4-1. The complete fabrication details and initial experimental evaluation of a single multicore SCIFI, as well as related research history are described in our recent paper [87].

In this paper, we report of the characterization of this multicore SCIFI faceplate through a combination of simulations and measurements. Section 4.3 describes

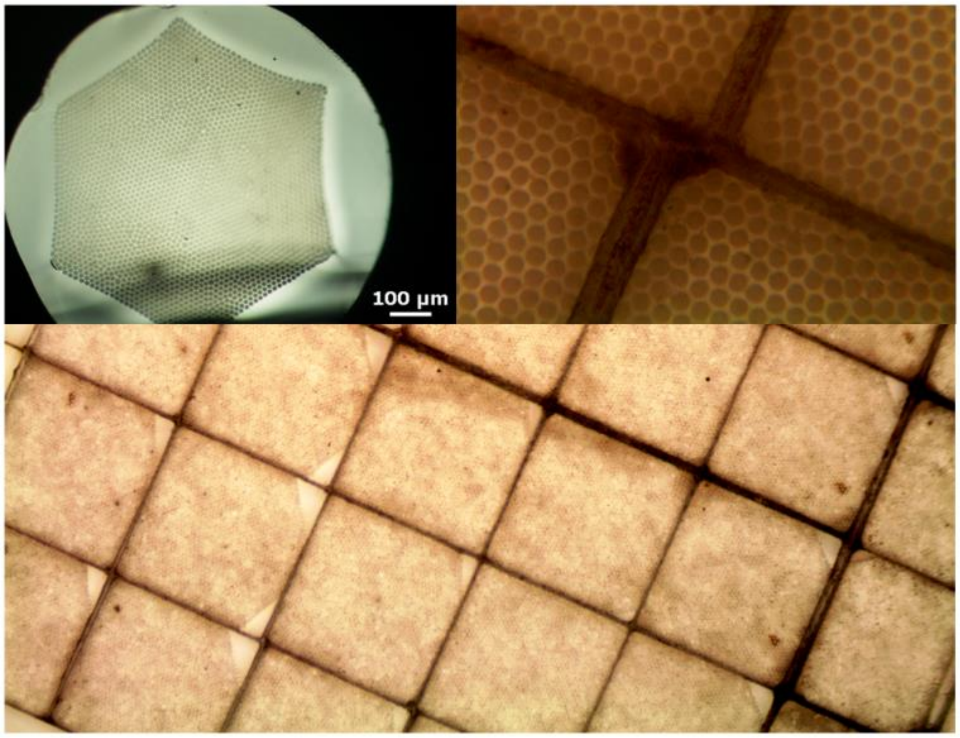

Figure 4-1. Microscope photos of the cross section of a microstructured multicore fiber with scale shown (*top left*), the stacked multicore fibers with 8.5 μm core diameters (*top right*), and the polished faceplate surface of a multicore SCIFI array with 0.5 x 0.5 mm pixels (*bottom*).

simulations of the scintillation light transport from thermal neutron conversion and an experimental estimate of the light yield of the SCIFI faceplate. Section 4.4 describes our experimental setup for neutron imaging. Section 4.5 presents our imaging resolution results. Section 4.6 gives conclusions as well as our expectations for further development of similar SCIFI neutron imaging instrumentation.

4.3 SCIFI Neutron Imager

The resolution of neutron images produced by the SCIFI is determined in a large part by the capacity of the optical fiber to collect the scintillation light inside of the SCIFI cores. Given that the scintillation wavelength is significantly smaller than the dimensions of the SCIFI multicore, light propagation is effectively modeled in terms of total internal reflection (TIR). When the refractive index of a fiber core, n_{core}, is greater than the refractive index of the fiber cladding, n_{clad}, scintillation light incident on the cladding will be captured into the core through TIR. The difference $n_{core} - n_{clad}$ is associated with a numerical aperture (NA) and a critical angle, θ_c, with respect to the normal of the surface, which determines the fraction of scintillation light guided with the SCIFI core. Modeling the TIR transport process is crucial towards understanding the ultimate potential for even higher resolution designs. In an ideal design, in which $n_{core} \gg n_{clad}$, negligible light transmission into the cladding matrix of the multicore fiber, as well as reduced inter-core cross-talk, would allow for one to image the end of the faceplate and resolve the ^{6}Li glass cores from the cladding with excellent contrast. Such an image would possess a spatial resolution limited by the pitch of the ^{6}Li glass cores at any frequency. In reality, the production of an actively scintillating microstructured multicore fiber requires matching a host of thermal, mechanical, and chemical properties, in addition to selecting ideal refractive indexes [88].

The precise n was measured for the monolithic ^{6}Li glass rod at five different wavelengths (633, 825, 1061, 1312 and 1533 nm) by a prism coupling technique (Metricon, model 2010). Ten scans were performed for each measurement with an estimated error of approximately $\pm$ 0.001. The measured refractive index values are reported in Table 4-1. A 3rd order Sellmeier equation was fitted to the measured refractive indexes (see Figure 4-2) to determine the n_{core} for the emission of the Ce^{3+} doped ^{6}Li glass within our simulations:

$$n(\lambda)^2 - 1 = \frac{A\lambda^2}{\lambda^2 - B^2} + \frac{C\lambda^2}{\lambda^2 - D^2} + \frac{E\lambda^2}{\lambda^2 - F^2}$$

where the values $1.285, 1.315 \times 10^{-2}, -1.051 \times 10^{-4}, 3.911 \times 10^{-1}, 1.327 \times 10^{-2}$, and 4.472 were found for A, B, C, D, E, and F, respectively. It was observed that the estimated n_{core} value of 1.55 for Nucsafe ^{6}Li glass matched to the commonly quoted value for GS20 at λ~395 nm. The N-KF9 cladding glass possesses a n_{clad} approximately equal to 1.54 at the peak scintillation emission. Applying Snell's law, the θ_c of the SCIFI waveguide is 83.49°. The other physical properties of N-KF9 (PN 523515.250) can be readily found in SCHOTT's Optical Glass Data Sheets. Again, the specific glass compatibility and fiber drawing process is described in detail in [87].

Table 4-1: Refractive index values for ^{6}Li-glass

Wavelength [nm]	$n \pm 0.001$
633	1.524
825	1.519
1061	1.515
1312	1.512
1533	1.509

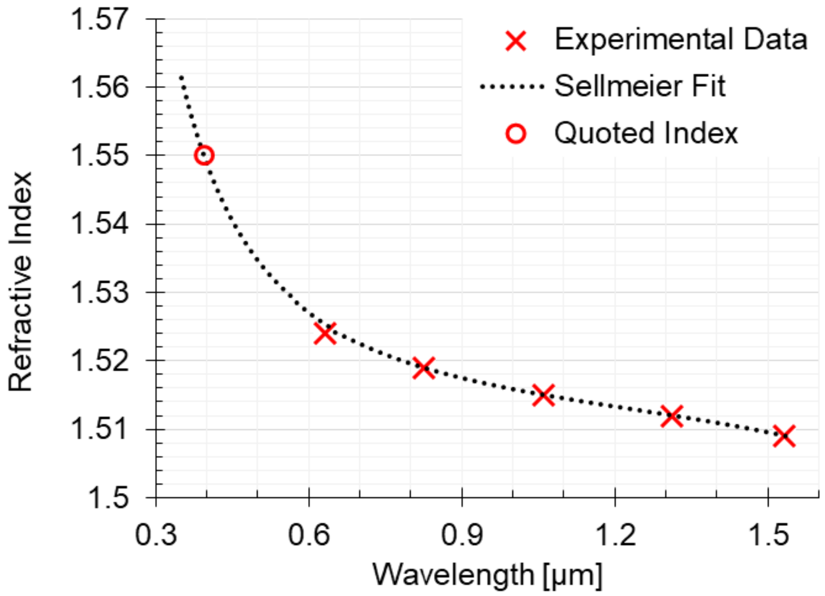

Figure 4-2. Sellmeier fit of the measured refractive indexes for the ^{6}Li glass. The error is smaller than the data points (see text).

4.3.1 Simulated Light Transport within the Multicore Structure

A model of the total averaged light transport to the exit, or imaged surface, of the faceplate is required in order to estimate an effective light yield. So, light propagation in the multicore architecture was simulated with the ray-tracing software Zemax OpticStudio 15.5 [89]. Three tasks were necessary to model the total light transport through the multicore SCIFI with Zemax: 1) define the materials and draft the architecture, 2) simulate the scintillation light source, transport, and detection, and 3) estimate the average total transported light as a function of distance to the imaged exit of the faceplate.

4.3.1.1 Material Definitions and Architecture

Using the Sellmeier fit described and the commonly reported density and thermal properties of GS20, the Li-glass material definition was added to the Zemax software material library. The default material definitions for N-KF9 found in Zemax's SCHOTT Material Library were used for the multicore cladding. Two-hundred-seventeen (217) cylindrical volumes of the defined ^{6}Li glass (dimensions of 4.25 μm radius and 1 mm length) were hexagonally packed within the N-KF9 cladding (dimensions of 100 μm radius and 1 mm length) with an 11 μm pitch, see Figure 4-3. The ^{6}Li cores were embedded within the cladding material with the exiting ends of cores exposed. A completely absorbing mock imaging surface of dimension 0.2 mm × 0.2 mm was centered 1 μm away from one end of the multicore fiber. The absorbing surface was created with an effective pixel size of 200 nm × 200 nm.

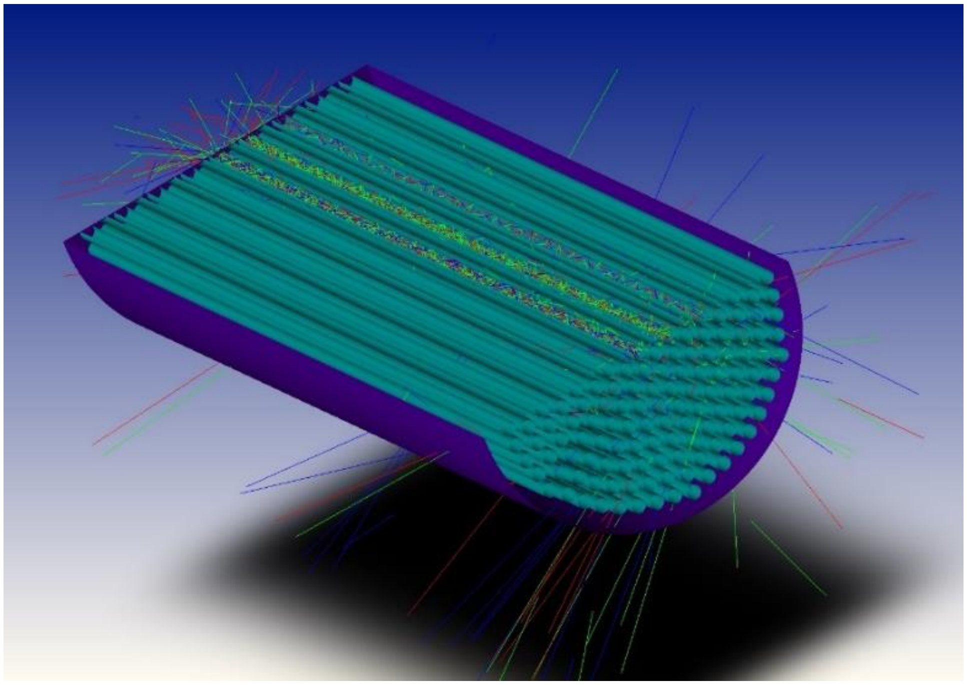

Figure 4-3. Cross-sectional image of the SCIFI Zemax model for 217 cores of ^{6}Li glass cores embedded in N-KF9 cladding with mock scintillation light source.

4.3.1.2 Simulated Scintillation

Ce^{3+} scintillation light was non-sequentially simulated using volumetric light sources with isotropic emission within the core glass. The light sources possessed discrete wavelengths of 395, 410, and 420 nm that were weighted to represent the observed emission of the SCIFIs, as discussed in more detail later. Mock scintillation along the charged particle tracks was simulated considering columnar light sources with lengths of 7 μm and 40 μm and radii of ~0.0196 μm and ~0.0648 μm, described earlier for the α and t, respectively. The volume of the columnar sources was rotated perpendicular to the length of the multicore fibers. The light from these sources was then non-sequentially transported to the absorbing detector, see Figure 4-4. Likewise, the columnar sources were simulated for a scenario in which the charged particles were emitted in the direction parallel with the length of the fibers. For particles produced inside of a core, emitted back-to-back, and simulated by a random orientation of the columnar sources partially ionized an average of 3 ^{6}Li-glass cores. A disk-shaped light source, with a length of 0.02 μm and a radius of 40 μm, was used to simulate the light transport for isotropic emissions from the origin of the model.

4.3.1.3 Light Transport

The average total light absorbed at the detector for the disk source, and the sum of the perpendicular and the parallel cases was tallied at incremental distances away from the detector. Total light was tallied, not only guided light, to better represent the number of photons incident on the photosensor during light yield measurements. A

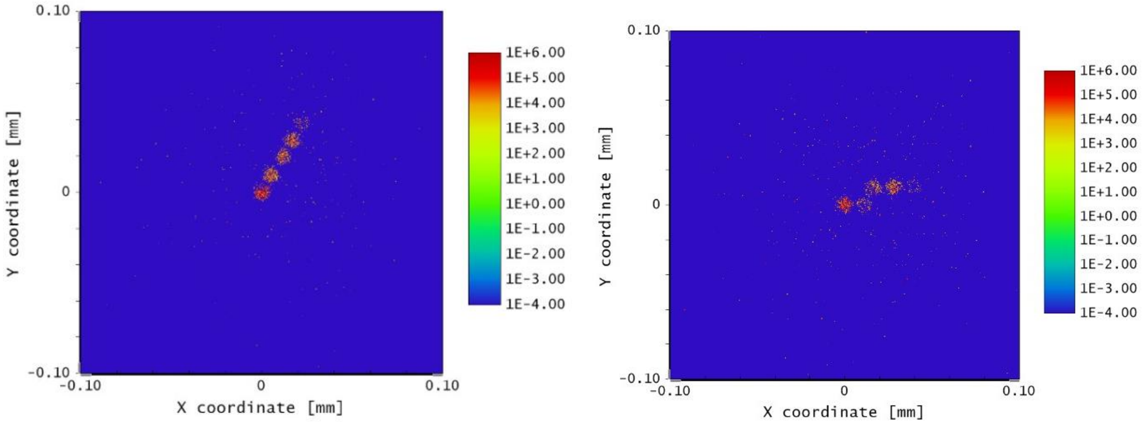

Figure 4-4. Simulated charged particle scintillation tracks of the thermal neutron capture on ^{6}Li emitted perpendicular to the multicore fiber 0.522 mm away from the detector at 60° (*top*) and 10° (*bottom*) relative to the abscissa.

fit to light transport of these simulated cases was made to estimate the percentage of photons transported to the detector outside of the exit of the fiber for neutron conversion scintillation at any given position within the 1 mm thick faceplate, see Figure 4-5. The expected percentage of transported light remains between 50% and 7.2%; the percentage is fundamentally limited by the maximum 2π geometry close in to the detector and the critical angle for TIR light produced 1 mm away from the detector.

4.3.2SCIFI Faceplate Light Yield Measurements with ^{241}Am

The total light yield responses from GS20 to either ^{241}Am irradiation or thermal neutron conversion are nearly identical when considering the dominant fast component of the scintillation light decay. This is because the total energy present and able to be transferred via ionized electrons to the supposed uniform concentration of Ce activator sites available in the ionized track volume of a 5.486 MeV alpha has been shown to be comparable to that of a thermal neutron absorption reaction $^{6}Li(n,\alpha)t$ for GS20 glass. Pulse shape and light yield measurements have verified this observation [90]. Thus, the ^{241}Am source could therefore be used to measure light yield from a known ionization location in a scale of minutes compared to the days required for thermalizing the available ^{252}Cf neutron source to record the same number of neutron events captured at random locations. In order to account for any discrepancies between the two yields, a conservative error representative of the difference in ionized volumes is propagated. These ionization volumes have been

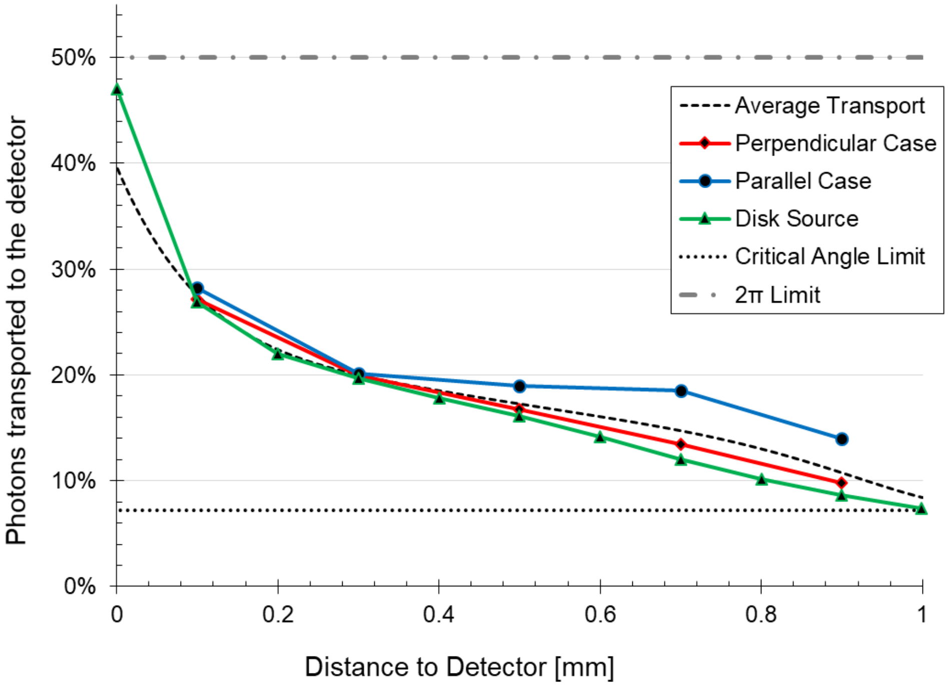

Figure 4-5. Simulated light collection for averaged charged particle emissions for various geometries as a function of distance transported.

estimated at $5360 \times 10^{-16} cm^3$ and $4730 \times 10^{-16} cm^3$ for the ^{6}Li absorption reaction and an ^{241}Am alpha, respectively [48]. A linear relationship between the two ionization volumes would underestimate the higher likelihood of recombination for the slower moving 2.04 MeV conversion alpha compared to the 5.486 MeV alpha, and thereby overestimate the potential difference in light yield. Thus, at maximum, one would expect the light yield value of ^{241}Am alpha to be within a 12% error of the $^6Li(n,\alpha)t$ reaction.

Light yield measurements were conducted to better understand the specific scintillation properties of the Nucsafe ^{6}Li glass within the faceplate. To collect the photons, a surface of the SCIFI faceplate was coupled to a R4998 Hamamatsu photomultiplier tube (PMT) with silicone grease. A 1 μCi ^{241}Am source was placed on opposite surface, then both source and faceplate were secured to the PMT window with Teflon tape. Inside of a light tight dark box, the PMT setup was biased to -1825 V and its signals were sent to a CAEN DT 5720 digitizer. The waveforms from individual alpha events were collected with a 300 ns window. Comparison between the energy histogram obtained from the waveforms revealed that X-rays from the ^{241}Am source contributed to approximately 0.97% of the total integrated charge. The integral charge of 260,000 alpha waveforms was then averaged to obtain an average integrated charge collected from the SCIFI faceplate in response to a 5.486 MeV alpha. It was found that an integrated charge, C_{int}, of 16.7 $\pm$ 0.2 pC could be expected per alpha.

Digitized reference plots for the PMT's gain, G_{PMT}, radiant sensitivity, RS, and quantum efficiency, QE, and the previously measured radioluminescence response of the faceplate, were used to estimate an average number of photons collected at the PMT window across the emission spectrum, see Figure 4-6. The peak emission wavelength of the SCIFI faceplate is 405 nm, as seen in the radioluminescence spectrum, which is near to the typical emission of Ce^{3+} for GS20 scintillating glass. Zemax simulations of columnar light sources 23 μm in length, representative of the 5.486 MeV alphas, were run to determine the expected percentage of photons that are transported from the alpha event to the photodetector. For this case, it was estimated that an average light transport, LT, of 7.4% of the scintillation photons would reach the PMT window. Thus, light yield was estimated by

$$LY = \frac{C_{int}}{G_{PMT} \cdot e \cdot QE \cdot RS \cdot LT}$$

where G_{PMT} is 1.2×10^6, QE is 20.6%, RS is 74%, and the charge constant of an electron, e, is $1.602 \times 10^{-19} C$. LY was estimated at ~7,700 photons per 5.486 MeV alpha. Thus, we would expect to collect 7,700 $\pm$ 1,000 photons per thermal neutron conversion. Nucsafe's ^{6}Li glass is reported at a 15-30% higher light output as compared to the 6,000 photons per thermal neutron conversion that is frequently cited for GS20 [91]. It should also be noted that the ionization energy lost by the ^{241}Am alpha to the cladding glass is assumed to be equivalent to the energy lost by the

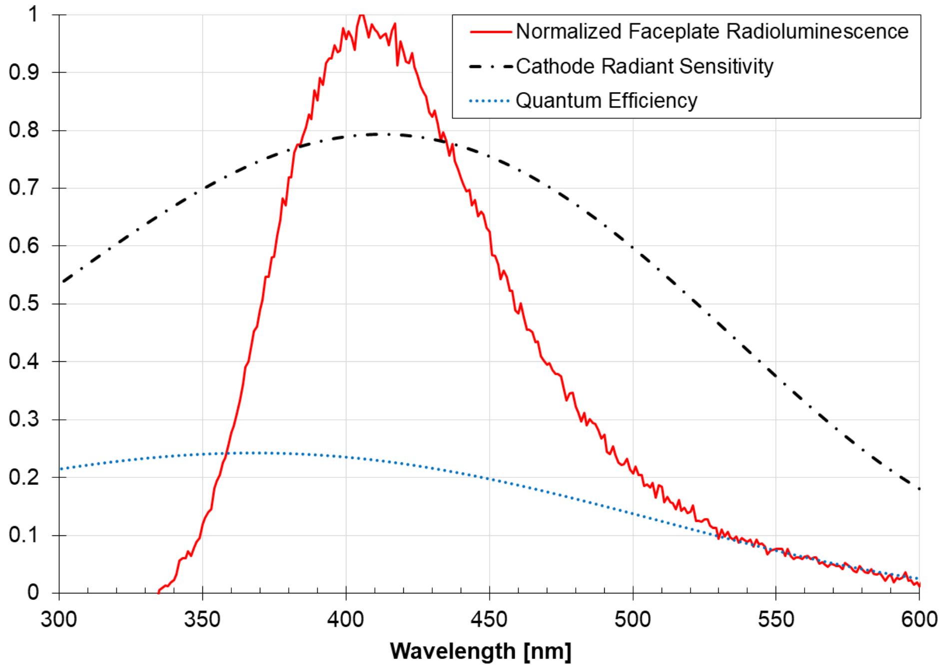

Figure 4-6. Normalized SCIFI faceplate radioluminescence plotted against the specific QE and radiant sensitivity of the PMT.

conversion particles in the SCIFI faceplate due to the random trajectories both encountering the same packing fraction.

4.3.3 Neutron Conversion Photons

The neutron conversion efficiency of the SCIFI faceplate was determined empirically in basic terms using the dominant $^{6}Li(n,\alpha)t$ absorption cross section, σ_{abs}, of 940 barns ($10^{-24}\,cm^2$) for 2 Å wavelength thermal neutrons. The attenuation is expressed by the Beer-Lambert law, $I = I_0 exp^{(-\Sigma \mu_i x_i)}$, where I_0 and I are the incident flux and transmitted flux of neutrons at iteration i, at x thickness for an attenuation coefficient μ. The attenuation coefficient is calculated as $\mu_i = \sigma_{tot} N_A c_i$, where σ_{tot} is the total thermal neutron cross section for the SCIFI faceplate, N_A is Avogadro's Number, and c_i is the molar concentration at i. Because the ^{6}Li absorption cross section is dominant, it is assumed that σ_{tot} is ~ σ_{abs} of ^{6}Li. Referencing the 7.38 weight percent Li_2O at a 95% ^{6}Li enrichment and 2.5 g/cm^3 density, the concentration of ^{6}Li atoms in the Nucsafe core glass is $\sim 7.575 \times 10^{21} atoms/cm^3$. So, the attenuation coefficient is 7.121 cm^{-1}. We note here that Nucsafe glass has nearly half of the ^{6}Li atom centration that is typically reported for GS20, resulting in an attenuation coefficient value of roughly half. Recalling the ~0.7 active volume at any given cross-section the attenuation of the SCIFI faceplate for a thermal neutron beam is,

$$\frac{I}{I_0} = exp^{(-0.7 \cdot 7.121\,cm^{-1} \cdot 0.1)}$$

Since the thickness of the faceplate is 0.1 cm, one would expect 39% of the thermal neutron beam to be absorbed in the detector. Further, the average depth of neutron absorption is about 0.479 mm into the SCIFI or 0.521 mm away from the imaging surface of the detector. Plotting the average light transport fit against neutron attenuation, it is found that ∼17.5% of the 7,700 scintillation photons will reach the imaging surface of the SCIFI at the average depth of neutron absorption, see Figure 4-7.

4.4 Experimental Setup

The SCIFI faceplate was imaged at the Pulse OverLap DIffractometer (POLDI) beamline at the Swiss Spallation Neutron Source (SINQ) hosted by the Paul Scherrer Institut (PSI). POLDI utilizes a thermal neutron spectrum of 1.1– 5 Å with a maximum flux at the imaging target of about $10^8\ n/s/cm^2$, where the beam aperture was adjusted to provide a L/D ratio of ∼240 [83]. The Neutron Microscope (NM), a high resolution and numerical aperture optical microscope, was used to image our SCIFI faceplate. Distinctively, the NM possesses a magnification and numeric aperture, described in [82] [92], that enables a nominal pixel size of acquired images down to 1.3 µm, and a true spatial resolution of about 5 µm. The faceplate was substituted in for the gadolinium oxysulfide ($^{157}Gd_2O_2S:Tb$) (Gadox) scintillating screen typically used with the NM [36]. Due to the thickness increase of the SCIFI faceplate compared to the Gadox screen developed for the framework of the NM, focusing on the end of the faceplate was nontrivial. As done previously [87], a diffused blue light source was

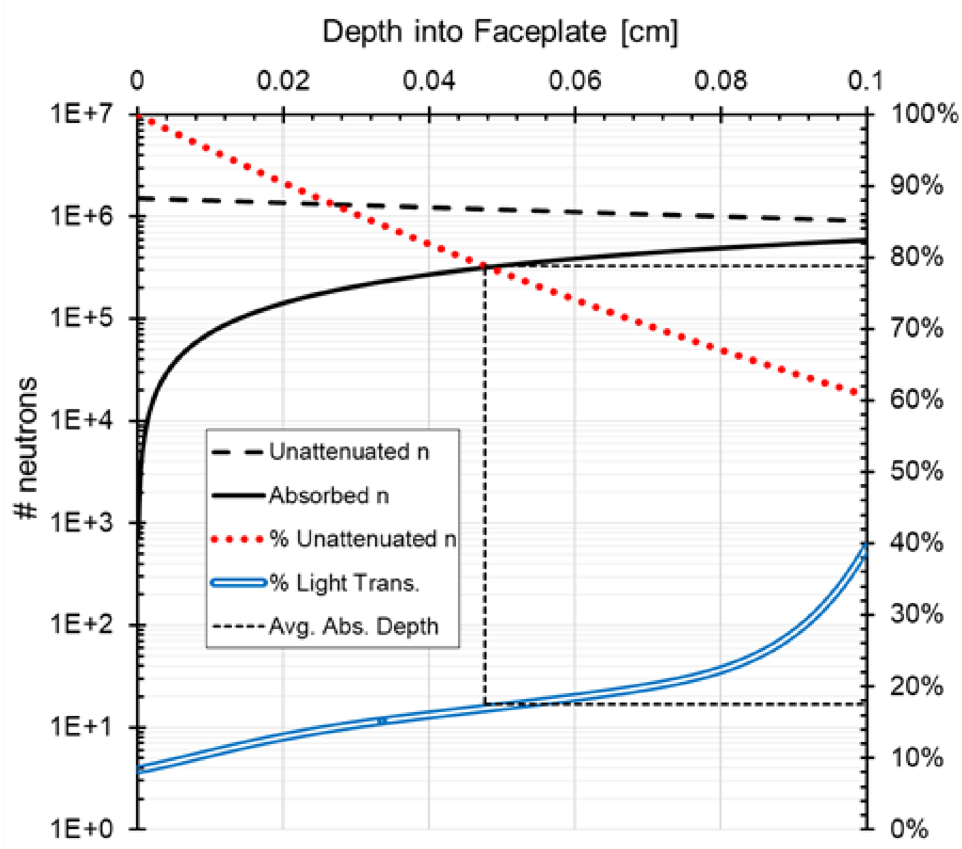

Figure 4-7. Thermal neutron attenuation as a function of depth into the SCIFI faceplate plotted against the fit of average light transport to the imaging surface of the simulated detector.

used to optically focus the microscope onto the imaging surface of the faceplate. After optical focusing, Al tape was used to seal the faceplate in the light-tight adaptor for imaging.

With the SCIFI in place, the dark field (DF) and open beam (OB) images of the scintillator alone were first acquired. DF and OB acquisitions are images of the scintillator sealed within the light tight adaptor without an imaging object with the neutron beam shutter closed and shutter open, respectively. These images are acquired to reduce the influence of the neutron beam intensity gradient, background radiation, inhomogeneity of the faceplate, and inherent imaging readout noises on the resolution of the neutron radiographs during post processing. In order to match the beam shape for the aperture slit positions for a 240 L/D ratio, the acquired field of views were down selected from the possible 5.5 × 5.5 mm to 2.6 × 4.4 mm, corresponding to 936×1584 pixels in the x and y directions, where a $2.\overline{77}$ µm effective pixel size was calculated from the acquired images. Two DF images and 120 OB radiographs were acquired with 300 s exposures at a 50 kHz and 16-bit readout rate. A large number of OB images were taken to compensate for the pulsed mode of SINQ that shares the high intensity proton accelerator beam for the production of ultracold neutrons, and other fluctuations in the beam current. A PSI Siemens star neutron imaging test target was then positioned directly in front of the Al capped SCIFI faceplate [84]. Seventy-five (75) neutron radiographs of the star were acquired with 300 s exposures for a total exposure time of 375 min.

4.5 Results

ImageJ software, an open source scientific image analysis tool, was used to process the acquired images [93][94]. Background radiation at the beamline and cosmic interactions with the CCD camera often speckle neutron radiographs with comparatively high grey count values in relative small pixel areas. To remove bright outliers from these interactions, all images compared a median grey count value of a 2 pixel neighboring radius of every pixel to a 25 grey count threshold for deviation. If a pixel exceeded this threshold, then it was replaced with the median value of the neighboring pixels. The DF and OB images were processed first to make the previously described corrections. After removing the bright outliers from the 2 DF image stack and the 120 OB image stack, each stack was projected to create a third z axis with ImageJ. The so-called z projections allow one to compare the value of a pixel at a specific x and y location to all of the other pixels at that same location across the stack of images, i.e. across the z axis. The z projection for the median grey count of every pixel, or the median image, was created for the DF and OB stacks. Next, the bright outliers for the 75 radiographs of the Siemens Star were removed in the same way described above. Then each image in the radiograph stack was divided by the intensity of the median DF and OB images' pixel grey count values. The sum of the z projection for the resulting stack of background corrected radiographs was then calculated to create a 300 s normalized radiograph of the star.

The isotropic resolution across the SCIFI can be estimated at ~25 μm by inspecting the resolved features of the resulting radiograph, see Figure 4-8 (*left*). A Fourier transform bandpass filter was used to smooth the radiograph by directionally blurring large and small structures separately. To extract a definitive maximum spatial resolution for the SCIFI faceplate, the highlighted region of the radiograph was transformed with a bilinear clockwise rotation of 10° and analyzed for the unfiltered and filtered image, Figure 4-8 (*right*). The inverted contrast of the highlighted Siemens star spoke was summed across the pixels in the y direction and plotted against the x distance with an error associated with the rotation and filtering. Ultimately, full width half maximum (FWHM) of 17.9 ± 0.4 μm and 16.1 ± 0.5 μm were obtained from Fourier peak fits to the spoke's line spread for both the unfiltered and filtered radiograph, respectively, see Figure 4-9.

4.6 Discussion and Outlook

The Zemax transport model described represents averaged values for scintillation light emission. For example, while it is most likely that 3 ^{6}Li-glass cores will be partially ionized by the charged particles from the $^6Li(n,\alpha)t$ reaction, the number of cores can range between 1 and 6. As the number of ionized cores increases, the amount of ionization energy lost also increases as the particles travel through greater distances of cladding. So, in the unlikely event that 6 cores are ionized, the total number of scintillation photons produced is lessened and divided amongst more cores. A similar situation occurs when alphas are produced close to the "wall" of a core, and are emitted towards one of the cladding vertices of the hexagonal packing structure. However, such situations have a small impact on the averaged light

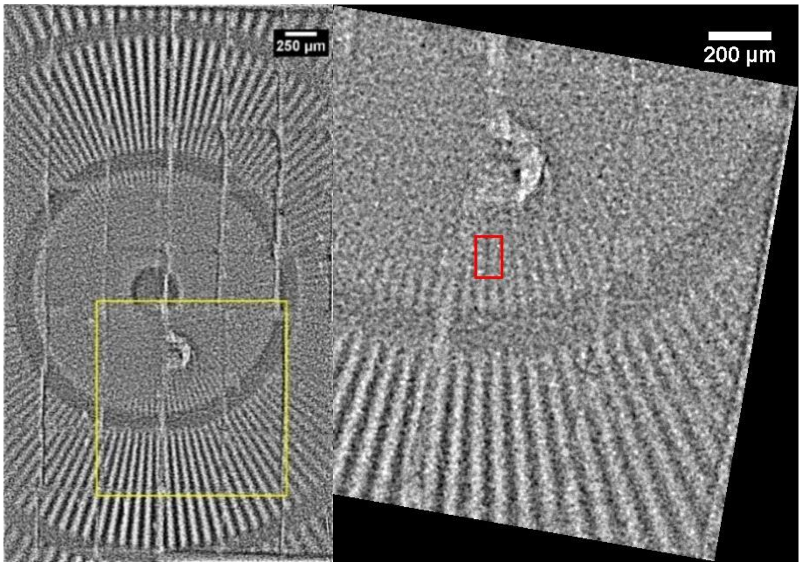

Figure 4-8. Neutron radiograph of PSI's gadolinium-based Siemens star processed with a Fourier Filter (*left*), and an enlarged region of interest with ~16 µm feature highlighted (*right*).

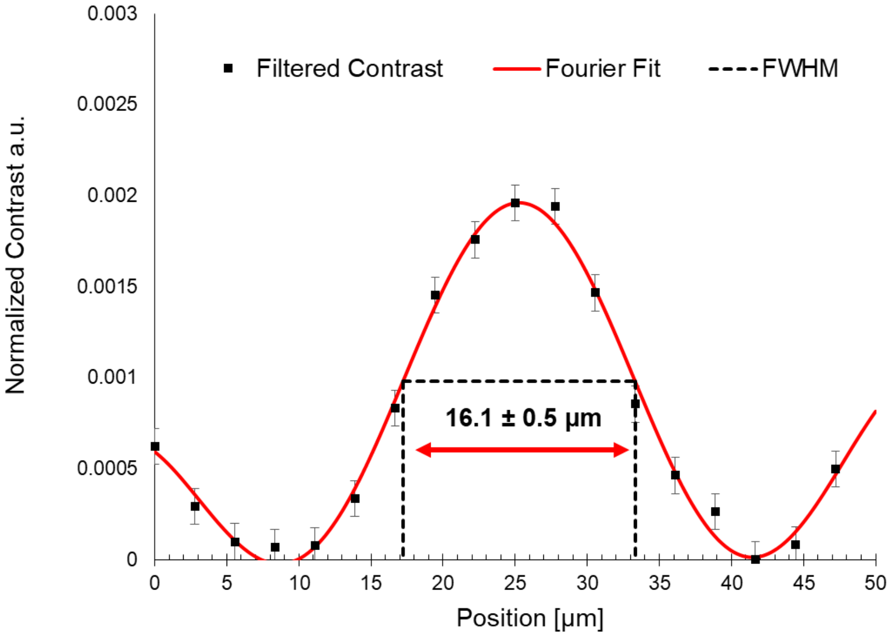

Figure 4-9. Line spread Fourier fit of measured contrast for resolved Siemens Star spoke with the FWHM denoted for the filtered radiograph.

emission since they represent rare events. So, the TIR transport model may be used to anticipate the photon collection of future iterative designs of the SCIFI with smaller core pitch or in the case of thicker faceplates. However, a full modal analysis is still required to describe the superposition of propagating modes with a mode field diameter, which differs from the physical geometrical dimensions resulting in light coupling between different cores. Integrating this understanding of transport with future background sensitivity and inter-core optical cross-talk studies will be crucial towards deconvolving charged particle tracks with advanced post processing techniques as described in [43].

The unfiltered spatial resolution measured is roughly equal to twice the pitch of the core packing. The ratio of the TIR light to simulated average total light is approximately equal to 7.2:17.5. In theory, this would suggest that at ∼50% of the modulation transfer function, a similar multicore design with a core pitch of 500 nm would be capable of resolving features on the order of 1 μm. Beside the scale of the architecture, the proof-of-concept design itself has ample room for optimization. For example, the current design could be improved upon by simply adding a reflective coating to the surface of the faceplate that is not imaged. Although not as simple, selecting a compatible optical cladding with a lower n_{clad} value would increase the contrast of the multicore fiber. An increase in single core numerical aperture would not only enhance light collection in individual cores, but it would also reduce any intercore optical crosstalk. Both of these features could improve the imaging performance of the SCIFI. Additionally, the possibility of directly coupling a optic SCIFI taper to a readout chip, imaging window, or even MCP touts potential light collection efficiencies that will be ever more important as the imaging community continues to probe increasingly smaller scales. Finally, event centroiding and deconvolution of particle tracks inside the multicore are post processing abilities that may also be applied to further improve the spatial resolution of an optimized light-guiding SCIFI neutron imager.

While currently limited primarily by the long exposure times required to overcome measured low contrast, the all-solid-state SCIFI design performs near to the current state-of-art spatial resolutions without event centroiding or other complex post processing techniques. Of course, the SCIFI-based radiography that we have demonstrated is one of several approaches for the advancement towards and beyond microscale neutron imaging. The use of scintillating screens, such as ^{6}LiF/ZnS and Gadox, coupled to image intensifying optical setups for high spatial resolution neutron imaging is popular among advanced neutron scattering user facilities due to their high neutron conversion efficiency and excellent light yield [81] [36] [95]. Additionally, neutron sensitive MCPs have become more common for high resolution setups, and have been successfully combined with Timepix/Medipix active sensor readouts for high temporal and spatial resolution measurements [42] [96] [97]. Yet, SCIFIs remain a cost effective, scalable, and neutron efficient imaging tool with a promising outlook for the future.

4.7 Conclusion

We have described the characterization of a SCIFI array via measurements and simulations in an effort to understand its current performance and the future potential for similar designs. The $^6Li(n,\alpha)t$ reaction light yield of 7,700 ± 1,000 photons per event was estimated with ^{241}Am irradiation of the faceplate for the Nucsafe glass. This measurement confirms that the expected light yield of the ^{6}Li glass has not deteriorated during multicore fabrication. Neutron radiographs of a PSI Siemens Star neutron imaging test target yielded an isotropic spatial resolution of ~25 μm of across the imaging surface of the SCIFI with 375 minutes of exposure. Here both the spatial and temporal resolution suffered from a nonuniform pixel stacking/polishing within the faceplate. However, specific regions of the faceplate resolved sub-20 μm features. The ultimate resolution for the ^{6}Li glass SCIFI faceplate of ~16 μm was determined by fitting the line spread of these features with a Fourier peak fit. To the authors' knowledge, this resolution is the best reported result for a ^{6}Li-glass-based or a multicore SCIFI-based neutron imager.

Chapter 5

Thermal Diffusion of Mixed Valence Ce in ^{6}Li Glass

5.1 Abstract

[vi]The creation and characterization of Ce doped surface regions in ^{6}Li enriched silicate glasses for cold neutron detection is described. A diffusion layer of a dried solution containing cerium III acetylacetonate hydrate was thermally diffused into monolithic glass samples under a reducing atmosphere. The diffusion characteristics of the mixed valence cerium compound were assayed with Rutherford Backscattering Spectrometry. The Ce diffusion activation energy within the glass was found to be 411 ± 53 kJ/mol (4.26 ± 0.55 eV). Radiation induced color centers formed on the diffusion samples as an effect of using alpha bombardment measurements. The ratio of Ce valence states of the diffused cerium was assayed as a function of depth with X-ray Photoelectron Spectroscopy, and the signal from Ce for the color centers was compared to the unirradiated sample surface.

5.2 Introduction

Neutron imaging is a unique utility for nondestructive analysis, specifically where cold neutrons are able to penetrate many dense materials, while remaining sensitive

---

[vi] Chapter 7 is a reprint of the material as it appears in *Journal of Non-Crystalline Solids* 2018. A*uthors:* M.E. Moore, H. Xue, P. Vilmercati, S.J. Zinkle, N. Mannella, J.P. Hayward. The dissertation author was the primary investigator and author of this paper.

to low atomic mass materials [98]. This results in the ability to assay an object even when it is found inside of an X-ray opaque housing material. Enabled by advanced neutron sources available internationally, neutron imaging is progressing the scientific community's understanding of advanced materials, next generation energy storage systems, precision manufacturing technologies, aerospace components, metallic additive manufacturing, plant physiology, and geosciences [4].

In spite of all the successes that neutron scattering science facilities have enabled in recent years, even higher-impact research is limited by the current spatial resolution of neutron detection devices. While X-ray imaging can resolve spatial features well below the micron level, the state-of-the-art for neutron scattering instrumentation is approximately 10-15 μm. High resolution neutron imaging represents a challenge since neutrons do not possess charge. So, their detection often relies on nuclear capture reactions that produce heavy charged particles (HCPs) that can then be detected using scintillation materials. Currently, the spatial resolutions of cold neutron imaging methods are fundamentally limited by the variance introduced by the tracks of these charged particles. Therefore, we are developing and experimentally characterizing micro-structured arrays of scintillating ^{6}Li silicate optical fibers that are capable of particle tracking. In past work, we used simulation and modeling to investigate an approach to reach spatial resolution down to ~1 μm using a scintillating lithium loaded glass microfiber array in combination with charged particle tracking, in order to determine the interaction site of each individual event [43].

Creating a thin region of scintillation (that could be tens to hundreds of microns thick, depending on the application) within a neutron-sensitive material could be used to avoid light loss arising from optically coupling conversion layers and scintillating films. Whereas some structured detectors such as patterned thin film, composites, and microchannel plate detectors have been researched for position-sensitive neutron detection, little effort has been made to create selective scintillating regions within structured detectors. This is likely because most commercially available glass scintillators, such as ^{6}Li enriched silicates, are drawn from a melt that uniformly contains an activator, with Ce being one of the most common activators used in neutron sensitive glasses. More specifically, cerium (III) oxide, Ce_3O_2, constitutes ~0.1 of the molar ratio or 3.8–4.6 weight % in the melt of common lithium and boron loaded glass scintillators [99] [46] [100].

As seen in Figure 5-1 the proof-of-concept system employs an Intensifying Charge Coupled Device (ICCD), which is sensitive to single photons, to collect the scintillation light. However, placing an ICCD directly into a neutron beam line is deleterious, sometimes irreparably, to the photosensor. To avoid light loss and to prevent damage to the photosensor, we intend to directly couple a bent, microstructured fiber array to the photosensor (see Figure 5-2). However, neutron captures along the arc of the bent fibers will create position confusion, as there would not be a one–to–one relationship. To avoid this loss of spatial resolution, we propose to selectively dope Ce as an activator into only the ends of the fibers. This concept is being investigated through controlled diffusion of Ce^{3+} into the surface of undoped, samples produced

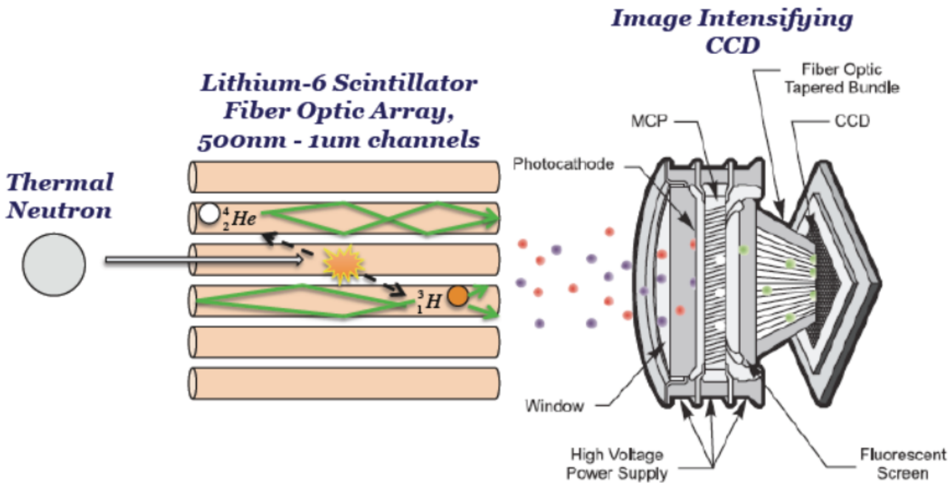

Figure 5-1. When neutrons are absorbed by the ^{6}Li loaded glass microfibers, the resulting reaction emits an alpha and a triton back-to-back. The heavy charged particles produce scintillation light, which is channeled down a waveguide comprised of the ^{6}Li glass cores surrounded by optical cladding glass, to be collected at an ICCD.

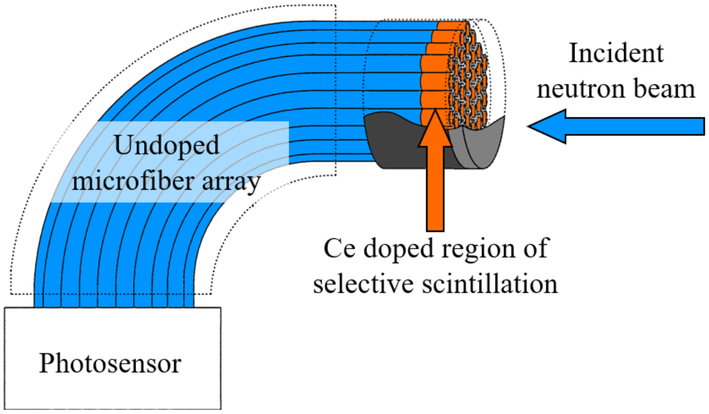

Figure 5-2. Illustration of a high resolution lithium-glass microfiber array, selectively doped only at the neutron detection end, designed to function as a waveguide to bend and taper scintillation light towards a position sensitive photosensor. Schematic edited from [101].

without the Ce activator, ^{6}Li loaded glass (fabricated by Nucsafe Inc., Oak Ridge, TN, USA) that is similar to the well-known GS20 scintillating glass.

In our recent research [102], we showed that Ce metal can be thermally diffused into the surface of undoped ^{6}Li-loaded glass. After using an AJA sputtering system to coat samples of monolithic ^{6}Li loaded glass with Ce metal, the samples were each heated, and the diffusion profiles of Ce for different heating temperatures (500–600 °C) and durations (1–4 hr) were studied using Rutherford Backscattering Spectrometry (RBS). From experimental results it was observed that: 1) longer annealing times are required to reach micron-scale diffusion depths, 2) more controls are necessary to allow uniform charge transport across the insulating glass samples, and, most importantly, 3) while sputtering from metallic Ce results in moderately successful thermal diffusion into the lithium-glass, it does not allow for precise control of the Ce charge state in the glass. This work addresses these issues by evaluating selective doping techniques using controlled thermal diffusion of a Ce (III) acetylacetonate solution into the surface of undoped, ^{6}Li-loaded glass. Herein, we present our doping technique, the results of micron-scale Ce diffusion concentration and depth assayed with RBS, an analysis of trivalent Ce content via X-ray Photoelectron Spectroscopy (XPS), and the creation of radiation-induced defects related to the reducibility of Ce^{IV} to Ce^{III}.

5.3 Fabrication Methods

5.3.1 Diffusion Layer

Since trivalent Ce is needed for scintillation, we used a Ce liquid solution that is unreactive with air, and is therefore expected to be better capable of maintaining the 3+ charge state throughout diffusion. Specifically, cerium III acetylacetonate hydrate [$Ce(acac)_3(H_2O)_2$] (Aldrich Prod. No. 381403), commonly referred to as “Ce acac,” is used to coat our undoped ^{6}Li loaded glass with a Ce diffusion layer. Since Ce acac powder is not able to be sputtered, coating is accomplished from a liquid form. To find a stable solution, Ce acac was dissolved into several solvents, yielding success with a toluene solvent. The solution was not viscous enough to be spin coated onto the samples in a reasonable timeframe. So, the solution was directly air dried onto the glass for the first batch (B1) of 6 irregular monolithic undoped ^{6}Li loaded glass samples (S1-S6). The synthesis was later refined by drying 24 mg of the Ce acac precipitate from the toluene solution in an open air-beaker at 80°C, similar to the work described in [103], where the dehydration stability of Ce acac was noted. The brownish amber precipitate was dissolved back into 0.5 mL of acetone and 15 mL of toluene before again being air dried onto the surface of a second batch (B2) of 4 monolithic undoped ^{6}Li loaded glass samples (S0-S3). Drying is expected to be responsible for an approximate $\leq 30\%$ loss of the Ce concentration [104].

5.3.2Active Reduction during Annealing

Most samples in B1 and B2 were annealed in a two step, drive-in and soak, heat cycle process. The annealing was performed in a MTI GSL1500X High Temperature Vacuum Tube Furnace with pressures around several mTr while flowing a nonflammable 2% H and 98% N reducing gas mixture. None of the B1 samples possessed visual clarity as the initial diffusion layer coating readily blackened. With the aforementioned changes to the diffusion layer that coated onto B2 samples, the samples better retained some transparency. Four samples in B2 were thermally annealed in two heat cycles, the drive-in and soak cycles at pressures between 5-10 mTr. The drive-in annealing temperatures ranged from 525°C to 600°C, and lasted for 5 hr. The soak annealing temperature was 510°C, and lasted for 24 hr. The 510°C temperature was chosen for the soak because it lies between the GS20 glass transition temperature (499°C) and the softening temperature (522°C). It was readily observed that visual transparency suffers under the described heat cycle at drive-in annealing temperatures above 550°C under the described heating conditions. It should also be noted that sample B2S1 slid slightly during the heating cycle, resulting in slight curved deformation.

5.3.3Capping

To make use of RBS and XPS measurements, the insulating glass samples required a conductive capping to avoid surface discharge under irradiation and outgassing. To stop excessive straggling of backscattered particles for RBS, the coating cannot be too

Table 5-1: Sample heating conditions

Batch	Sample	Drive-In Temperature [°C]	Drive-In Duration [hr]	Soak Temperature [°C]	Soak Duration [hr]
B1	S1	550	5	510	24
	S2				0
	S3	600			24
	S4				0
	S5	650			24
	S6				0
B2	S0	525	5	510	24
	S1	550			
	S2	575			
	S3	600			

thick at the sample surface, but a surface capping thickness should allow reasonable electrical conduction to avoid charge accumulation and sparking that may be damaging under ion irradiation. Thus, the samples were capped by DC sputtering graphite using an AJA International ATC Orion-5 confocal magnetron sputtering system at the Micro-Processing Research Facility at the University of Tennessee, Knoxville (UTK). The thickness of the capping was independently measured using Atomic Force Microscopy (AFM) at the Advanced Microscopy and Imaging Center at UTK. Both B1 and B2 samples were mounted to a glass microscope slide for sputtering using Kapton tape. The profiles of the graphite film edges that were exposed after removing the tape were then examined with AFM at multiple points on the glass slide (see Figure 5-3). An average graphite capping thickness between 10-15 nm was observed.

5.4 RBS Analysis

A 3 MV tandem accelerator was used to perform alpha RBS ion beam analysis of the samples at the UT-ORNL Ion Beam Materials Laboratory [105]. A silver-based paint was applied to the back side of the B1 and B2 samples (see Figure 5-4), and the samples were adhered to a RBS sample holder using C and Cu tapes to further allow for electrical conduction away from the samples' surface. The RBS Si detector energy was first calibrated using the backscattering surface signal from Au on a SiN film with a Si substrate at alpha energies of 4.5, 3.5, 3.0, and 2.0 MeV. An alpha energy of 4.5 MeV or 3.5 MeV was used for B1 and B2 samples, respectively, using a scattering angle

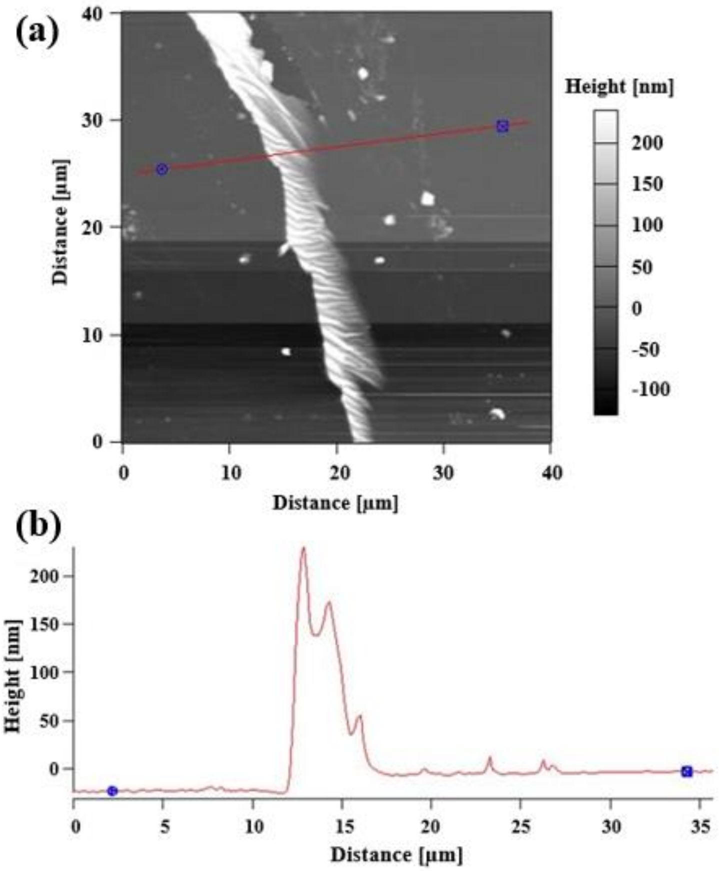

Figure 5-3. (a) Image of a graphite film edge deposited onto the microscope slide that was used to mount the B1 samples, (b) Atomic force microscopy height profile trace, shown in (a).

Figure 5-4. Illustration of sample positioning for RBS measurements

of 155°, and an exit angle of 25° relative to the incident beam direction. A constant alpha particle flux of 1.5×10^{13} cm^{-2} s^{-1} was incident on both the B1 and B2 samples. The ion fluence on each beam spot, which is 1 mm^2, was about 1.8×10^{16} cm^{-2}. The alphas that do not scatter are predominantly deposited at ranges deeper than 10 µm into the glass. Thus, accumulation of He ions has negligible effects on the close-to-surface region of the glass that contains the Ce diffusion profile. The backscattered counts are normalized between samples using the acquisition time and the estimated number of incident particles times the solid angle, in steradians, of the detector. Residual surface layers of the Ce acac coating were not removed prior to capping the B1 samples, which resulted in non-uniform target surfaces of the B1 samples. Diffusion layer non-uniformity on the samples' surface caused the O and Si signals to interfere with the Ce diffusion profile and led to increased spectral backgrounds. After making the aforementioned sample preparation changes to the B2 samples, the RBS spectra contained a clean region of interest for the Ce profile as seen, for example, in Figure 5-5. The uniformity of the samples was examined by comparing the spectra collected in different target regions for each sample. No significant differences were observed in the collected spectra based upon location selection.

At an alpha energy of 3.5 MeV, the backscattering count from alphas on Li and C atoms results from non-Rutherford collisions [105]. Thus, error is introduced at backscattered alpha energies below 1 MeV. Additionally, the effects of straggling and unscattered alphas are more pronounced at deeper depths where the concentration of the targeted Ce atoms is low. Thus, below 0.01 at.%, the concentration of Ce is

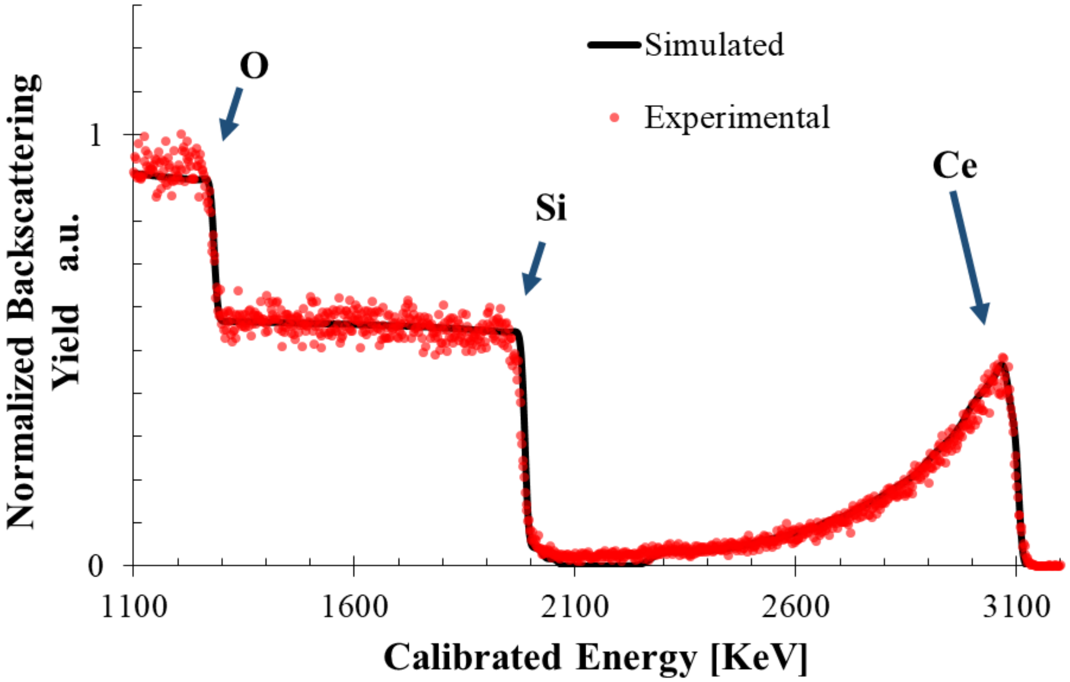

Figure 5-5. RBS spectrum for B2S2 measured using 3.5 MeV alphas with labeled element plateaus, simulated atomic concentration fit using SIMNRA. The associated error is smaller than the data markers.

assumed to be negligible due to the resolution limit of the RBS measurement. Fitting the RBS spectra with atomic concentration profile layers was accomplished with the SIMNRA code [106] which simulates elastic recoil detection and performs Nuclear Reaction Analysis (NRA). No reference samples are needed in order to determine the atomic percentage of Ce, because the Rutherford backscattering cross-sections are well defined in the SIMNRA code. A modified molecular composition of Soda-Lime Glass, as defined by SRIM-2013 [47] [107], with the addition of 6.54 at.% of Li, and a compound density of 2.5 g/cm^3 was used for the purposes of calculating atom concentrations of the diffusion profiles.

By fitting approximate diffusion coefficients, we can calculate the activation energy and pre-exponential factor via the Arrhenius equation. Thus, to estimate the diffusion coefficients, the normalized Ce concentrations are plotted as a function of depth for the B2 samples, then the B2 data sets were fitted to a standard profile for extended source diffusion,

$$C\,(x,t) = \frac{1}{2} C_0 \times erfc\left(\frac{x}{2\sqrt{Dt}}\right)$$

where $C\,(x,t)$ is the concentration of Ce as a function of diffusion depth, x, and time, t, C_0 is the initial surface concentration of Ce for an individual sample, $erfc$ is the complementary error function, and D is the diffusion coefficient. Using a nonlinear model for this equation to estimate D with constrained C_0 values, a fit was generated by minimizing standard error, t-statistic, and P-values for each B2 sample, see Figure 5-6. The extended source diffusion model was first fit to the soak temperature, and

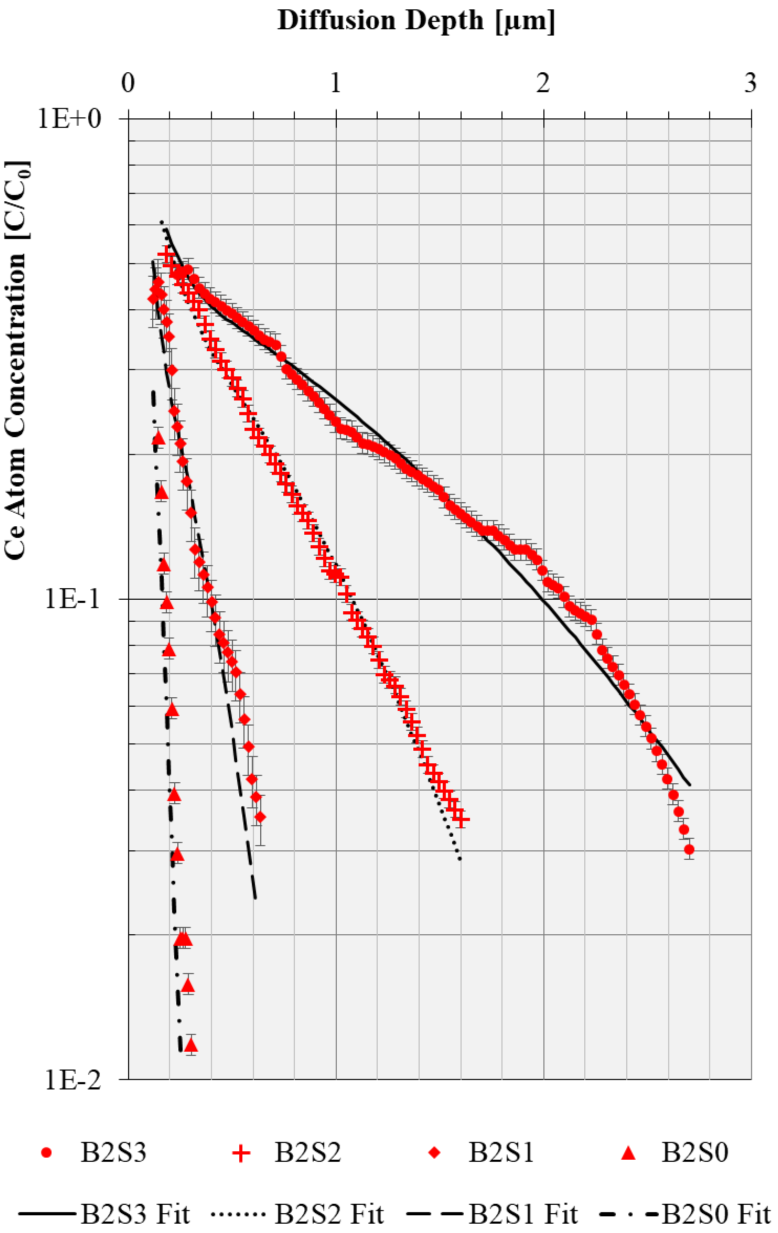

Figure 5-6. Surface normalized Ce concentration as a function of diffusion depth fit with the standard profile for extended source diffusion.

then to the drive-in temperatures. The fits clearly capture the near surface diffusion region, yet as the error increases with the square root of the concentration (counts), the trend diverges from the experimental data at greater diffusion depths. Because the soak annealing time was longer than the drive-in, at temperatures below glass softening, the experimental results for diffusion possess a linear trend further from the sample surfaces.

After fitting the 4 samples with an approximate diffusion coefficient associated with its annealing drive-in temperature and the 1 soak temperature, see

Table 5-2, we can calculate the activation energy and pre-exponential factor. The phenomenological Arrhenius relationship for this case of diffusion can be represented as:

$$D = D_0 \exp\left(-\frac{Q_d[J]}{RT}\right)$$

This can be rewritten as

$$\log D = \log D_0 - \frac{Q_d}{2.3R}\left(\frac{1}{T}\right)$$

where $Q_d[J] = \frac{2.3R}{K_B} Q_d[eV]$, D_0 is the pre-exponential factor, Q_d is the activation energy for diffusion, R is the gas constant, T is the absolute temperature in K, and K_B is the Boltzmann constant. Using these relationships, a weighted linear regression was performed to fit a trend to the 5 diffusion coefficients as a function of the inverse temperature for B2 samples (see Figure 5-7). The pre exponential diffusion factor and activation energy of Ce within the lithium loaded glass were found to be 4×10^{-13} m^2/s (95% confidence bounds are ± an order of magnitude) and 411 ± 53 kJ/mol 4.26 ±

Table 5-2 : Ce diffusion coefficients for ^{6}Li-loaded glass

Annealing Temperature [°C]	Diffusion Coefficient [10^{-17} m^2s^{-1}]
510	1.3 ± 1
525	3.3 ± 1
550	26.4 ± 5
575	196.4 ± 56
600	670.8 ± 140

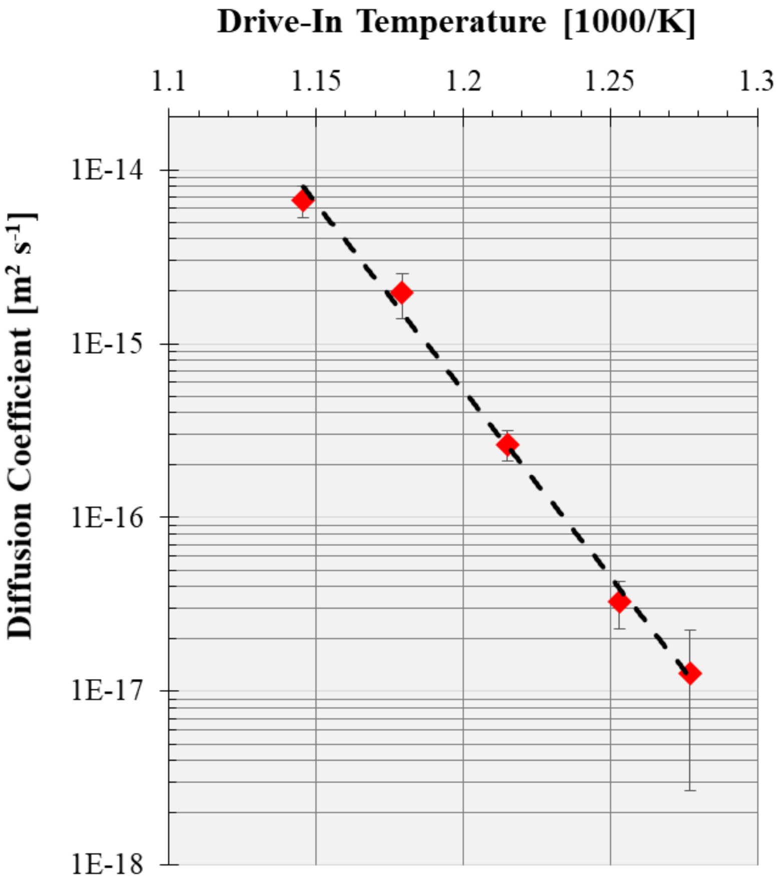

Figure 5-7. Ce acac solution diffusion coefficients for thermal diffusion within the ^{6}Li-loaded glass under a reducing environment.

0.55 eV, respectively. The goodness of the linear fit is described as the sum of squares due to error: 0.02546, R-square: 0.9952, root mean squared error: 0.09212.

5.5 XPS Analysis

In the case of the proposed neutron sensitive glass fibers, HCPs are produced from neutron captures, primary and secondary electrons are ionized in the wake of the HCPs and migrate through the glass until some become trapped, and, in turn, excite trivalent Ce, Ce^{+3}, stimulating scintillation. This well-known Ce scintillation process requires the trivalent transition state of Ce. Unfortunately, Ce^{+3} readily oxidizes to tetravalent Ce, Ce^{+4}, which has an overlapping absorption band with the Ce^{+3} emission that is believed to inhibited light yield [46][108]. So, it is vital to characterize and increase the relative concentration of Ce^{+3} compared to Ce^{+4} for the Ce diffusion layer and as a function of depth.

In the case of XPS, an X-ray source is used to eject core-level electrons with a specific kinetic energy (KE). The KE of any ejected electron is dependent on the Binding Energy (BE) of the electron according to

$$KE = h\nu - BE$$

where h is the Planck constant (6.62×10^{-34} J s), and ν is the frequency of the absorbed X-ray. The BE peaks in a spectrum are characteristic of the atomic structure, electron orbital, and chemical environment, among other factors. In this work, an Al $K\alpha_{1,2}$ (1486.6 eV) X-ray source was employed, and the corresponding XPS measurements were used to study the 3d spin-orbit region of the valence of the Ce acac solution thin film. Core-level spectroscopy of Ce oxide spectra, like other rare earth compounds, is governed by atomic multiplet effects, where the Ce $3d_{5/2}$ and Ce $3d_{3/2}$ spin-orbit components of the Ce^{3+} and Ce^{4+} mixture are superimposed. To determine the Ce valence state ratio in the diffusion layer, we note the presence or absence of the Ce^{4+} 916.7 eV BE peak, which is separated by means of spectral deconvolution. The deconvolution of spectra was accomplished following the method that was presented in [109].

5.5.1 Thin Film Diffusion Layer

To determine the ratio of the valence states in the Ce diffusion layer, the Ce acac solution was pipetted and dried onto a brushed Cu foil substrate to create a thin film. The Ce thin film was then assayed with the Advanced Photoelectron Spectrometer facility at the Joint Institute for Advanced Materials. For decomposition, a cleaved piece of Ce_2O_3 (Aldrich Prod. No. 342955) was then measured as a XPS spectral reference for the Ce^{+4} contribution to the 3d region (see Figure 5-8.) Using the Origin 2017 software package (OriginLab, Northampton, MA), a ‘U 2 Tougaard’ background was subtracted from the reference sample spectrum. Both the Ce^{+4} reference sample and Ce thin film specimen spectrum were acquired with the same parameters to allow for identical spectral data processing and direct comparison.

Due to the presence of the 916.7 eV peak in the Ce thin film, it is assumed that the spectrum contains mixed valence states. As seen by the blue line in Figure 5-9, the Ce

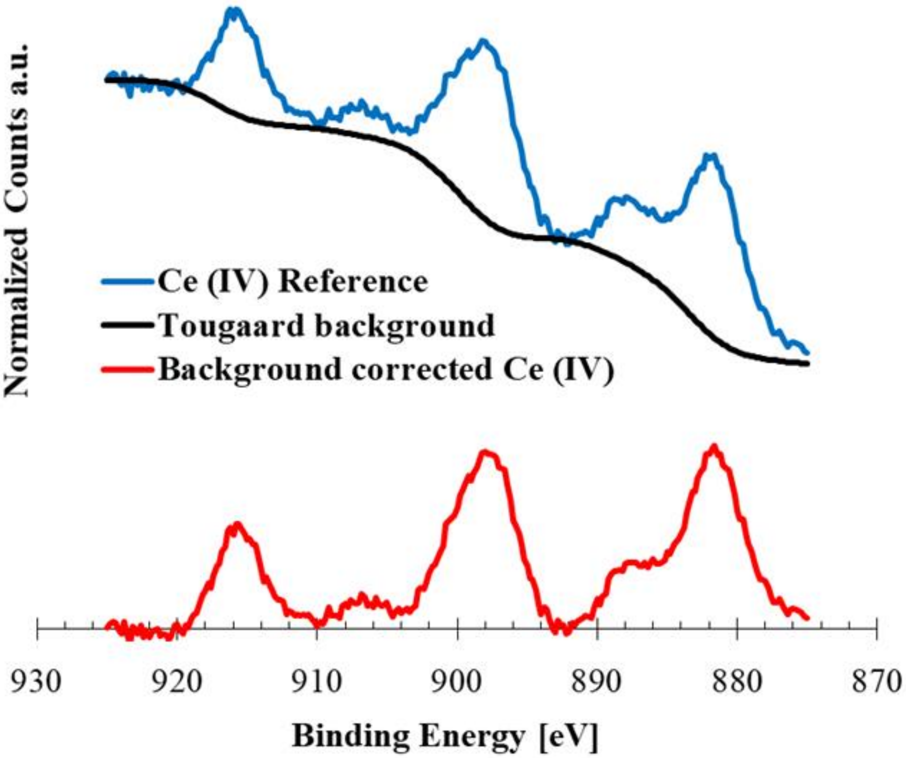

Figure 5-8. XPS spectrum of the Ce^{IV} reference sample with Tougaard background correction.

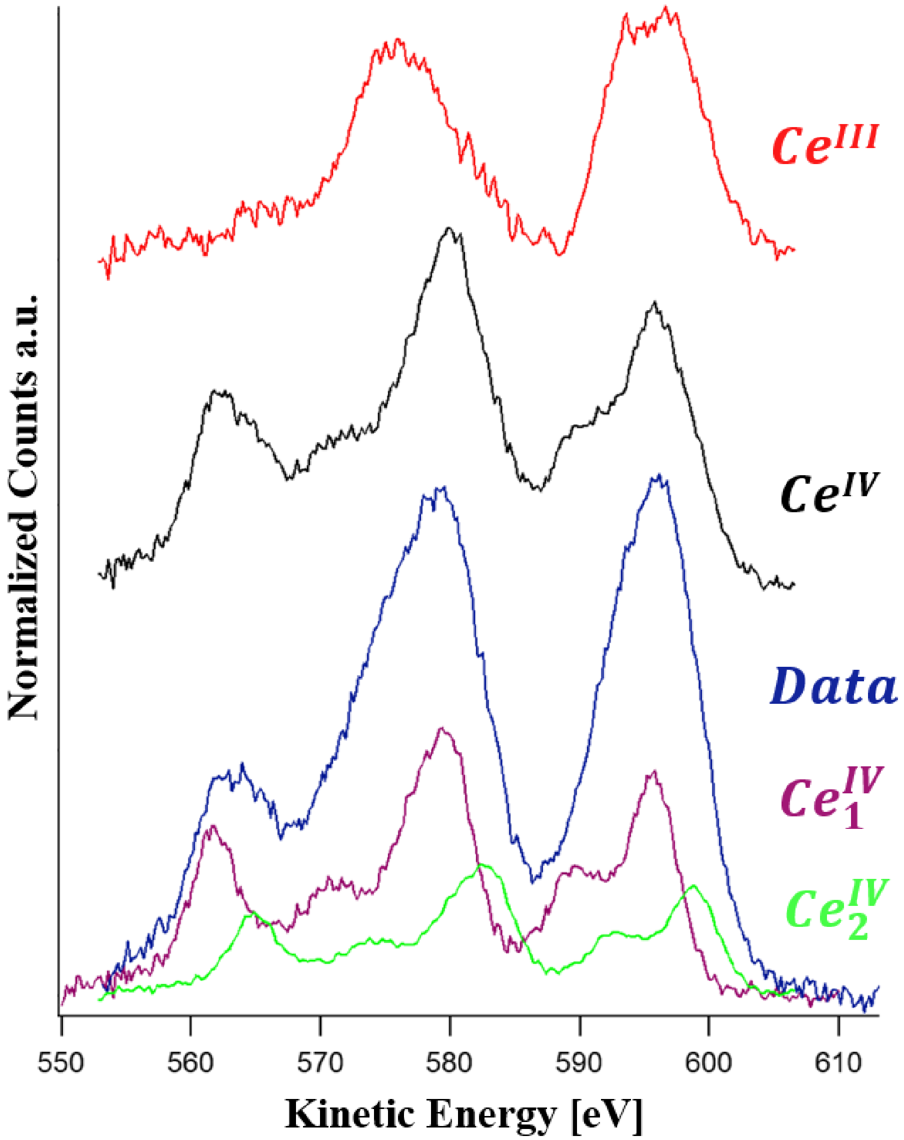

Figure 5-9. Normalized and Shirley background-corrected XPS spectra, where hν = 1486 eV, of the Ce thin film data and the spectral components used to deconvolve the concentrations of Ce^{III} and Ce^{IV}. See text for details.

thin film spectrum (labeled as *Data*) is given by a linear combination of components coming from Ce^{III} and Ce^{IV}:

$$Data = C\,(Ce^{III}) + C\,(Ce^{IV})$$

where the C values are the relative concentrations. The value of $C\,(Ce^{IV})$ is established empirically by normalizing the Ce^{IV} reference spectrum with the *Data*, and calibrating energy to match the position of the 916.7 eV BE peak. Normalization is performed to account for the order of magnitude increase of Ce at.% in the Ce^{IV} reference sample compared to Ce acac thin film. Since it is known that the intensity of the Ce^{+4} 916.7 eV peak cannot exceed the intensity, I, of the data, the relative concentrations of Ce^{III} and Ce^{IV} were determined as:

$$C\,(Ce^{III}) = \frac{I\,(Ce^{III})}{I\,(Ce^{III}) + I\,(Ce^{IV})}$$

$$C\,(Ce^{IV}) = \frac{I\,(Ce^{IV})}{I\,(Ce^{III}) + I\,(Ce^{IV})}$$

Because the 916.7 eV peak in the *Data* spectrum is considerably broadened, subtracting $C_B(Ce^{IV})$ from the *Data* results in the same slightly shifted characteristic peak for Ce^{IV}. If this result were due to either charging effects or the inhomogeneity of the Ce thin film, a general broadening of the entire spectrum would be seen. However, since this is not the case, it is hypothesized that two different chemical environments of tetravalent Ce exist: (1) mixed valence Ce throughout the diffusion layer, and possibly (2) a near surface oxide. Thus,

$$C\,(Ce^{III}) = Data - \; C\,(Ce^{IV})\,;$$

$$C\left(Ce^{IV}\right) = C\left(Ce_1^{IV}\right) + C\left(Ce_2^{IV}\right)$$

where environments (1) & (2) constitute 60 ±10% and 40 ± 10% of the Ce^{IV} concentration, respectively. Applying these equations to the case of the Ce thin film on the Cu substrate, it was found that $C\left(Ce^{III}\right)$ is 0.50 ± 0.12. Here, the reported uncertainty propagates from the relative error when measuring low concentrations, the assumed separation of the chemical environments used for decomposition, and the background subtraction. Two independent analyses of the data, handled with Shirley XPS background, yielded lower results, ~0.40, for the Ce^{III} concentration than when a U2 Tougaard XPS background was used, resulting in $C\left(Ce^{III}\right)$ equal to approximately 0.60. Combining the techniques, where the Tougaard method was used to handle the uncluttered Ce^{IV} reference spectrum, and the Shirley method was used to deconvolve the data, lead to an intermediate $C\left(Ce^{III}\right)$ value of approximately 0.50.

5.5.2Valence as a Function of Depth

Following the analysis of the Ce acac solution thin film used as the diffusion layer, the relative concentration of Ce valence states as a function of diffusion depth within the glass samples was examined. The spectra for the Ce 3d region of B1S3 were taken before using and in between using a sputtering gun, located within the spectrometer vacuum chamber, to remove approximately 100 nm/min from the sample surface. The XPS spectra were acquired before sputtering Ar at 500 eV with a 3 mA current, after 300 s, and after 600 s, as shown in Figure 5-10. The total at.% of Ce at the surface

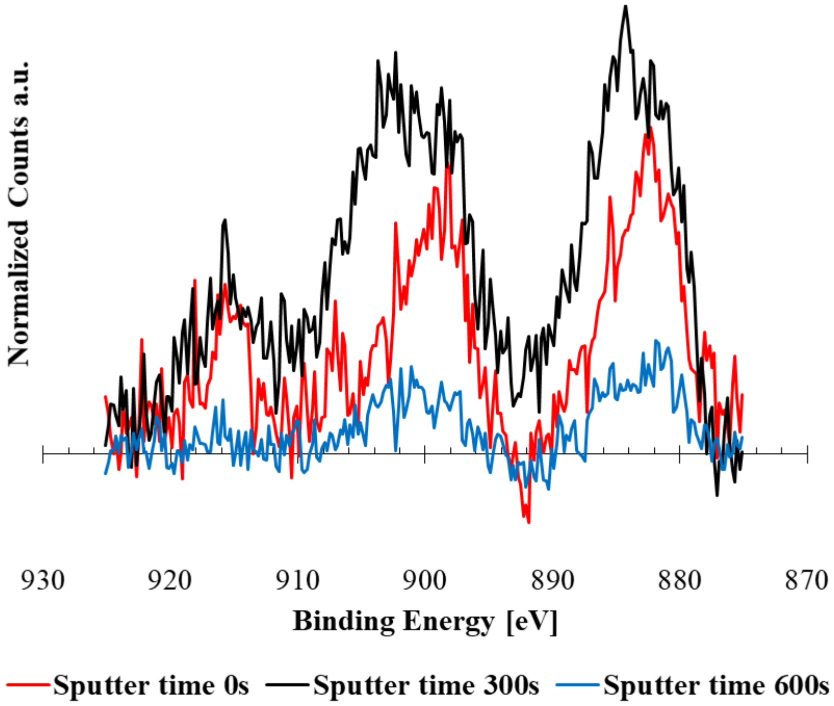

Figure 5-10. Normalized and Shirley background-corrected XPS spectra for B1S3 as a function of sputtering time.

of B1S3 is 6 ± 1 at.%, an order of magnitude less that the 70 at.% of Ce within the Ce^{IV} reference sample, which has a less complex XPS signal comprised of only 6 BE peaks from one valence state. Additionally, the counting statistics of quantifying Ce concentration suffer from more uncertainty as a function of depth due to the exponential nature of diffusion. Thus, estimates of 0.20 ± 0.10 Ce^{III} : Ce^{IV} at the surface layer and 0.30 ± 0.10 Ce^{III} : Ce^{IV} after 300 s of sputtering were made. The SNR for the 916.7 eV peak is 1.4, 3.0 and 0.6 before sputtering, after 300 s, and after 600 s of sputtering, respectively. Thus, it is likely that the Ce is almost entirely reduced. Via inspection, it is observed that sputtering away the graphite cap both broadens and increases the intensity of the Ce 3d region's signal.

5.5.3Valence of Radiation-Induced Color Centers

As advanced neutron scattering facilities aim to serve the neutron imaging scientific community, increasing the cold/thermal neutron flux of current beam lines is vital. It is known that at high doses, glass scintillators can begin to exhibit radiation damage that inhibits light yield. Specifically, the loss in performance of Ce-based Li silicate is believed to stem from the creation of absorption centers that attenuate the Ce^{3+} emission (395 nm) [36][110][111]. Li silicates are prone to absorption centers due to their cation disorder and non-stoichiometry. Irradiation of the ^{6}Li loaded glass will induce lattice defects, predominately F+ centers that trap electrons at oxygen vacancies [112]. For the sake of scintillation-based detection, the creation of color centers suggests near UV light absorption in Li silicates. Thus, as the coloring increases, the light reaching the photosensor gradually diminishes. In addition, there may also be interference with the processes that give rise to the emission of the scintillation light itself by introducing more trapping defects.

Following 10 minutes to hours of alpha backscattering, yellowish radiation induced color centers were formed on the surface of the B2 samples at both of the RBS beam spots for each sample. These color centers are ascribed to the creation of F+ centers. Assuming that the rate of coloring resulting from 3.5 MeV alpha radiation is proportional to the vacancies/ion created, then it is possible to estimate the time for the onset of coloring in a thermal neutron beam using the vacancies/ion created from the ^{6}Li (n, α) capture reaction in the glass. The ratio of vacancies created by thermal neutron capture compared to RBS alpha bombardment, A_{vac}, is estimated to be 1.27 via simple K-P calculation using SRIM-2013. Since 10 minutes of alpha backscattering irradiation corresponds to an average alpha particle fluence, Φ_{α}, of 9×10^{15} cm^{-2}, then

$$t = \frac{\Phi_{\alpha}}{A_{vac}\phi_{n}E_{th}}$$

$$E_{th} = (1 - e^{-\mu x})$$

where ϕ_{n} is the flux of the thermal neutrons at glass scintillator, E_{th} is the thermal neutron detection efficiency for thickness, x, and linear attenuation coefficient for neutron capture, μ. The current upper limit of ϕ_{n} at the target stations in neutron scattering facilities is about $1 \times 10^{9} cm^{-2} s^{-1}$, x is based on the 12 μm depth that RBS alphas penetrated the glass, and μ is 14.85 $cm^{-1}$for 0.025 eV neutrons at a ^{6}Li concentration of $1.58 \times 10^{22} \frac{atoms}{cm^3}$. Using these conditions, it is expected that coloring would occur after 13 years of continuous exposure.

XPS characterization of these color centers was performed to determine the effects of the alpha bombardment on the valence of the Ce content. A Mo mask was fabricated to ensure that the XPS beam spot was probing only either the irradiated or the as annealed portion of the sample's surface. Examining the Ce 3d region of the color center in comparison to the as annealed surface, it was observed that the Ce BE signal was only immediately observable in the color center. To ensure that the intensity of the Ce measurement was not caused by the removal of the inhibitive graphite capping via RBS alpha bombardment, samples B2S0 and B2S3 were sputtered with Ar, similarly to B1S3. It was observed that the Ce intensity from the radiation-induced color center was actually enhanced $70 \pm 10\%$ after 100 s of sputtering. After further sputtering, XPS measurements probed deeper until the SNR for intensity of the Ce signal dropped below the error of the counts, converging to a nominal silicate substrate spectrum, as shown in Figure 5-11. It should also be noted that B2S0 possessed the lowest concentration of Ce, approximately 1 at.%, of any of the annealed samples due to its low annealing temperature and the removal of surface residue prior to capping.

It is known that trapping holes at Si and Li vacancies will create O anions. It has also been shown [113] that if a sufficient continuous supply of displaced O anions is provided, then enhanced reducibility in ceria is guaranteed. Thus, there could be competition between radiation-induced absorption centers and radiation-enhanced

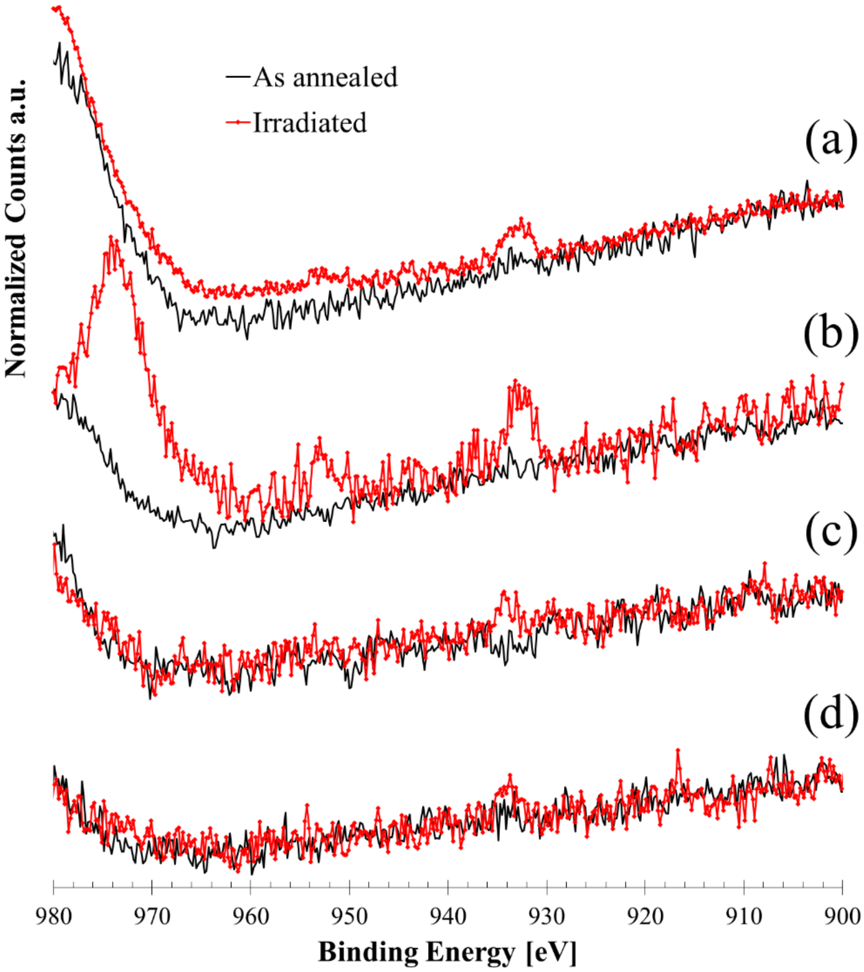

Figure 5-11. Normalized XPS spectra of the irradiated color center and the as annealed sample surface at a) 0 s, b) 100 s, c) 200 s, and d) 300 s of Ar sputtering on B2S0.

diffusion of O anions that drives oxidization and reducibility under high doses. An analysis with SRIM-2013 suggests that 160–190 displaced O defects are created along the 12 μm track of a 3.5 MeV alpha. This penetration depth is in good agreement with the ranges found for ^{6}Li (n, α) inside of Li silicates [100]. Given the aforementioned alpha penetration angle for the B2 samples, the XPS measurements were probing closer to O defect reduced regions of the irradiated color centers as a function of Ar sputtering time. Examining the O 1s region of the XPS spectra, a secondary peak of displaced O defects is built into the irradiated surface, as seen in Figure 5-12. Thus, the concentration of Ce within the color centers of the sample was likely augmented by radiation enhanced diffusion of reducing anions.

5.6 Conclusions

Results of our experiments to dope the ^{6}Li loaded glass with an appreciable amount of trivalent Ce suggest that Ce can be thermally diffused at temperatures below 575°C without visual hazing or physical deformation of the glass under the described heating conditions. The activation energy for the Ce diffusion within the glass was found to be 411 ± 53 kJ/mol (4.26 ± 0.55 eV). With this activation energy, it is shown that 1 at.% Ce concentration diffused at least 1 μm with 5 hr of annealing at 550°C. Thus, an order of magnitude higher diffusion depth, or 10s of μm, should be expected following days of annealing at 550°C. For a unique application such as fabricating high resolution, cold neutron imaging detectors for advanced neutron scattering facilities, this length of time is not prohibitive. Upon examining the valence of the diffused Ce,

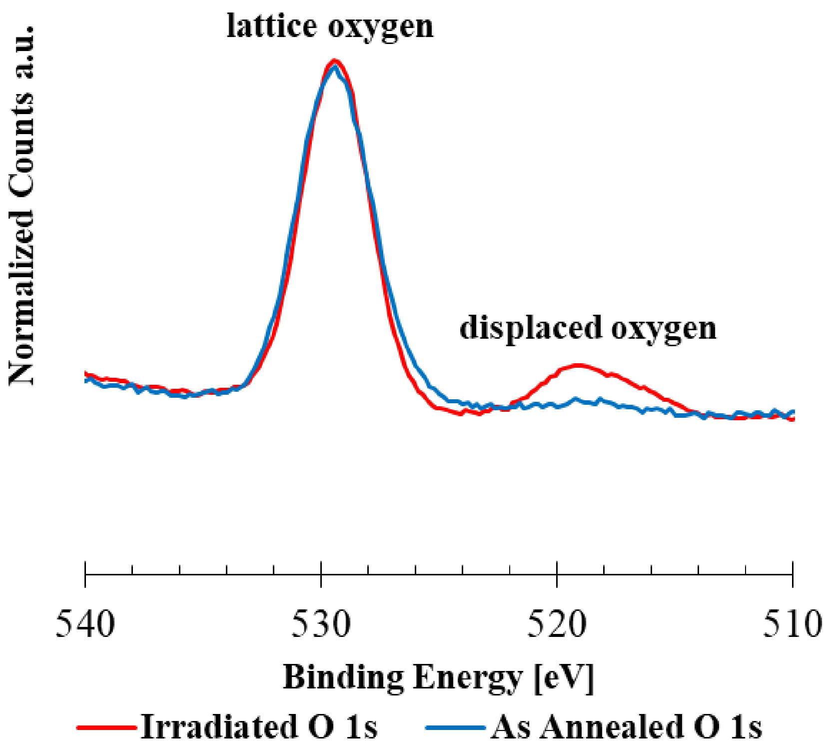

Figure 5-12. XPS spectra of the O 1s region for the irradiated and as annealed surfaces of B2S3

we estimate that a roughly similar ratio, 1:1 of Ce^{3+}: Ce^{4+} valence states exists within the diffusion layer. After annealing with a reducing atmosphere, it was shown that the $Ce4^{+}$: $Ce3^{+}$ ratio is greatest at the samples' surfaces, < 50 nm, 0.80 ± 0.10 $Ce4^{+}$: $Ce3^{+}$, supporting the assumption that a near surface Ce (IV) oxide layer exists. The SNR of the 916.7 eV peak as a function of diffusion depth suggests that Ce is increasingly reduced as it diffuses deeper, and the Ce content is almost completely reduced to Ce^{3+} at depths near 1 μm. Thus, a surface polishing technique applied in an inert environment is expected to be able to remove the layer of tetravalent Ce that accounts for much of its observed concentration.

While the formation of color centers is somewhat expected under prolonged high flux alpha bombardment, the suspected radiation-enhanced reduction of Ce within the silicate was not anticipated given the differences between the Li silicate and pure ceria. It was observed that the Ce intensity after sputtering away the surface layer from the radiation-induced color center was increased by $70 \pm 10\%$. This could suggest that radiation-enhanced reduction may assist in creating regions of selective scintillation within the proposed glass fiber scintillator, provided that the coloring is negligible or reversible. Future work will include use of the obtained activation energy to produce monolithic samples appropriate for efficient cold neutron detection and imaging and thorough characterization of the scintillation properties of samples in which the same Ce compound has been more deeply diffused.

Chapter 6

Thermal Diffusion of Mixed Valence Ce in $YAlO_3$

6.1 Abstract

[vii]Active radiation environments and high-rate backgrounds pose a significant challenge towards improving the detection and characterization of Special Nuclear Material (SNM) using Associated Particle Imaging (API). Ongoing research seeks to reduce the sensitivity of a charged particle, or associated particle, detector to x-ray background through the creation and characterization of an alpha-sensitive, Ce-doped surface region of Yttrium Aluminium Perovskite (YAP). A wet-chemical layer of trivalent cerium (III) acetylacetonate hydrate was thermally diffused with a reducing atmosphere into single YAP crystals for a temperature range of 800°C to 1500°C. The diffusion concentration profile of the cerium compound was assayed with Rutherford Backscattering Spectrometry (RBS), where the Ce diffusion activation energy and the pre-exponential factor within YAP were found to be 1.02 ± 0.10 eV and $9.7 \pm 2.0 \times 10^{-15}\, m^2 s^{-1}$, respectively. Resulting transient polycrystalline structural features at the surface of the YAP crystals were investigated with X-Ray Diffraction (XRD). YAP, Yttrium Aluminium Garnet (YAG), and Yttrium Aluminium Monoclinic (YAM) phases were identified, as well as contributions from

---

[vii] Chapter 8 has been submitted to a peer-reviewed journal for publication of the material. A*uthors:* M.E. Moore, C. Delzer, J. Watts, C. Redding, C. Xu, R.M. Collette, B.L. Musicó, S.M. McConchie, P.D. Rack, Y. Zhang, M.S. Koschan, C.L. Melcher, J.P. Hayward. The dissertation author was the primary investigator and author of this paper.

Y_2O_3, CeO_2, Ce_2O_3, and the metastable hexagonal polymorph of $YAlO_3$ (YAH). The luminescent response of the complex surface layer to x-ray and α excitement was examined as a function of annealing temperature. Radioluminescence emissions typical of the Ce^{3+} $4f \rightarrow 5d$ transition occupying both the Y^{3+} and Al^{3+} sites in YAP and YAG were observed. The brightness of the samples under alpha radiation increased as a function of diffused Ce concentration until the point of optical darkening.

6.2 Introduction

Interrogation of SNM with Associated Particle Imaging (API) relies on the detection of the D-T fusion products: an α particle (He^+) and a neutron, emitted back-to-back in the laboratory frame at energies of 3.5 MeV and 14.1 MeV, respectively. The Ce-doped Yttrium Aluminum Perovskite (YAP:Ce) scintillator has been shown to be an excellent α detector for API due to the fast component of its decay constant (~25 ns [114]) [114]) in response to α particles, as well as its robust chemical and mechanical properties. However, background radiation, whether it be from a dynamic background at a seaport of entry or from the D-T reaction itself, will negatively impact the performance of YAP scintillators used to detect the α particles [115].

X-ray production is an embedded side effect of neutron generation. X-rays of sufficient intensity and energy can interfere with the dead time and throughput of detecting prompt gammas following neutron activation of a target. More specifically, an X-ray emission with a peak around 70 keV has been identified within vacuum chamber systems similar to those employed with API [116]. In particular, x-ray production is significant in D-T generators. In [3], an x-ray emission with a peak around 70 keV was identified within vacuum chamber systems similar to those employed with API. The origin of these x-rays is associated with the ion tube used within neutron generators. The attenuation length of ion tube x-rays in YAP is between 0.5 – 1.2 mm, depending on the specific energy of the X-ray and the density of YAP crystal [117]. Thus, a significant quantity (60% or more) of the x-rays that are incident on a 1 mm thick YAP scintillator will interact via photoelectric effect or Compton scattering.

Shielding an α detector within a vacuum chamber from such x-rays presents a significant technical challenge and does not mitigate the effects of a hot and/or dynamic measurement environment. Reducing the thickness of the scintillator will certainly reduce the noise from background radiation, that is, until the structural integrity of the scintillator is compromised, especially in cases where the surfaces are etched [118]. Little success has been reported on the creation of an α detector significantly thinner than 1 mm, and robust enough to survive vacuum bake-out. So, to produce a scintillator insensitive to background radiation with a single optical plane, we propose to create a near surface, α-sensitive scintillating region of a thicker single crystal by doping an activator microns into the surface. Specifically, the thermal diffusion of Ce into a YAP crystal is investigated in this work.

Although roughly the same number of X-ray interactions would occur within an undoped YAP crystal (containing no Ce), only 1-2% of the interactions from 70 keV x-rays would cause scintillation in a crystal with a 10 μm thick activated surface layer of YAP:Ce. Meanwhile, calculations within SRIM [47] show that a D-T 3.5 MeV He^+ will stop within a YAP crystal after traveling ~7.6 μm. Thus, an α detector with a selectively activated 10 μm surface would remain sensitive to He^+, while detecting an order of magnitude fewer low energy x-rays. In this paper, we explore the diffusion of relatively large amounts of Ce into the near surface of YAP crystals and the subsequent optical and structural effects. Specifically, we report the activation energy for Ce diffusing into YAP, the optical transmission, Radioluminescence (RL), α response, and the resulting polycrystalline phase transformations of the annealed crystals.

6.3 Experiment Procedure

Undoped YAP single crystals with dimensions of 5×5×1 mm were sourced by Proteus Inc. (Chagrin Falls, Ohio) from Hangzhou Lambda Photonics Technology Co., Ltd. The density of the samples was reported as $5.37\ g/cm^3$, and the atomic density was estimated at $9.79 \times 10^{22}\ atoms/cm^3$. Our related research [102] [76] aimed at thermally diffusing Ce into an amorphous lithium silicate was referenced to create a diffusion layer. A 1:1 Ce^{3+} to Ce^{4+} mixed valence diffusion layer was created by heating, dehydrating, rewetting, and drying a cerium acetylacetonate hydrate [$Ce(acac)_3(H_2O)_2$], toluene, and acetone solution on the surface of the glass samples. This same process, described in detail in [76], was used to create the Ce dopant layer on the YAP samples for thermal diffusion.

6.3.1 Ce Diffusion

A CM Model 1730-12 horizontal tube furnace was used to anneal the YAP crystals at temperatures between 800°C to 1500°C for a 10 hr duration, see Table 6-1. A reducing atmosphere of nonflammable of 2% H and 98% N gas mixture was used to convert Ce^{4+} to Ce^{3+} at standard atmospheric pressure. A piece of electrical tape was present in the tube furnace during the heating cycle for S7, which contributed to darkening and affected reduction.

6.3.2 Conductive Capping

Rutherford Backscattering Spectroscopy (RBS) analysis of the Ce diffusion profile within the annealed crystals required a conductive capping layer to avoid sparking, surface discharge, and outgassing while under He^+ bombardment. Since RBS is both energy and angle sensitive, the capping must also be sufficiently thin to avoid additional lateral straggling of the He^+ particles during irradiation. The samples were coated with a thin (10s of nm) amorphous carbon layer using DC sputtering of a 50 mm diameter graphite target using 100 W, 5 mTorr Ar for ~20 minutes with an AJA International ATC 2000 sputtering system.

6.3.3 Rutherford Backscattering Spectroscopy

Ion beam analysis with α RBS was performed at the UT-ORNL Ion Beam Materials Laboratory using a 3 MV tandem accelerator [105]. An He^+ energy of 2.0 MeV was used at a scattering angle of 168° and an exit angle of 12° relative to the incident beam

Table 6-1: Heat cycle parameters for annealed samples

Sample	Ramp Up Rate [°C/min]	Anneal Temperature [°C]	Anneal Duration [min]	Ramp Down Rate [°C/min]
S1	20	800	600	10
S2	20	850	600	10
S3	20	900	600	10
S4	20	1000	600	10
S5	20	1100	600	10
S6	20	1200	600	10
S7	20	1300	600	10
S8	20	1400	600	10
S9	20	1500	600	10

direction. The Si α-backscattering detector was calibrated with $KTaO_3$, SiC, and $LiNbO_3$ substrates. Samples S1, S3, S5, S7, and S9 were initially examined with RBS, followed by S2 and S8. 25 μC charges were applied to each sample, and the live-time exposure was approximately 300 s. The samples were irradiated with a constant He^+ particle flux of 1.5×10^{13} cm^{-2} s^{-1} within a beam spot of 1 mm^2.

6.4 Results

6.4.1 Rutherford Backscattering Spectroscopy

2.0 MeV He^+ energy was selected to measure the diffusion concentration profile of Ce with good depth resolution. However, due to the high portion of energy lost to low mass number (A) elements, non-Rutherford collisions start to contribute error to the backscattered count around 1 MeV. The software SIMNRA [106], which simulates detection of elastic recoils based on Nuclear Reaction Analysis (NRA), was used to estimate the areal density of the crystals' constituent elements and the diffused Ce as a function of depth. The simulated areal densities are fitted by adjusting the number of slices, thicknesses, and relative ratios of atomic concentration layers as well as setting experimental constraints and physical sample parameters, see Figure 6-1. As is typically mentioned, RBS cross-sections are robustly characterized within SIMNRA, such that no standard samples are needed for reference to measure the presence of Ce. The standard stoichiometric ratio of YAP along with the constant atomic density of the samples were used to convert areal density to atom concentrations. It should

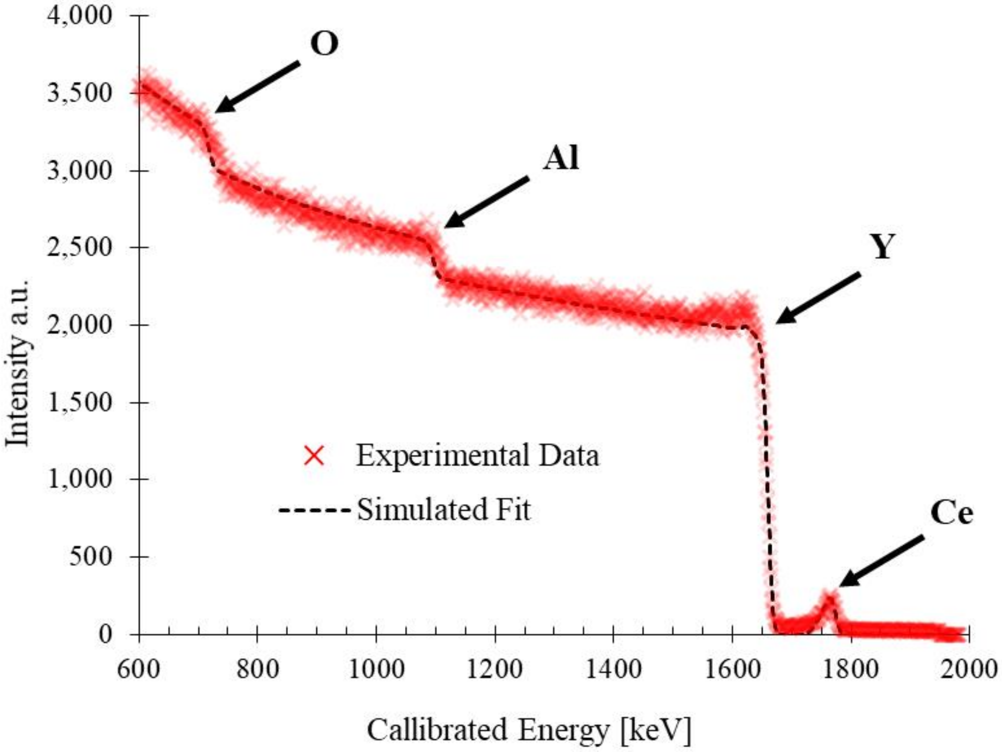

Figure 6-1. RBS spectrum for S2 measured using 2 MeV He+ with labeled element concentration plateaus, simulated atomic concentration fit using SIMNRA. The associated error is smaller than the data markers.

also be noted that Ce concentrations below 0.01 at.% are inapplicable due to the elemental areal density resolution limit of the RBS measurement.

As it happened, the RBS spectrum for S1 contained no measurable diffusion. Whereas, the diffused Ce concentration profile for S9 completely overlapped the Y concentration plateau for the YAP crystal and could not be deconvolved without significant error. In order to calculate the activation energy of Ce in the surface of the YAP, at least 5 fitted Ce diffusion coefficients at different temperatures are needed to generate an accurate linear regression fit. That is why S2 and S8 were also measured to better estimate the activation energy.

The Ce concentration profiles were then fit with a diffusion model to determine the diffusion coefficients, *D*. The model is based on straightforward, one-dimensional diffusion of a constant source concentration into a semi-infinite medium. Of course, the distribution of the Ce dopant layer is not actually constant or uniform between all discreet points throughout diffusion. However, it can be reasoned that 1) the diffusion layer is distributed with a self-consistent uniformity within the 1 mm^2 area of the RBS beam spot, 2) the driving diffusion mechanisms within the probed area are related to near surface diffusion, and 3) the volume of the of crystal wherein diffusion occurs is negligible compared to the volume of the diffusion layer both before and after annealing. Under such conditions, it has been shown that our assumptions accurately fit the bulk diffusion characteristics [119] [120]. Thus diffusion can be easily described with the complementary error function solution to the diffusion equation:

$$C\,(x,t) = C_0 \times erfc\left(\frac{x}{4\sqrt{Dt}}\right) \quad (1)$$

provided $C\,(x,t)$ is the atomic concentration of Ce as a function of diffusion depth, x, and time, t, C_0 is the initial surface concentration of Ce for an individual sample, $erfc$ is the complementary error function. Using the model D was fit to the Ce concentrations by constraining C_0, minimizing standard error and P-values, and maximizing the t-statistic, see Figure 6-2. The near surface region is fit with the described diffusion model within the context of the above assumptions, and a deeper secondary diffusion trend is not. This secondary region possess a more shallow gradient not related to C_0 as described in equation (1), and is considered further in the succeeding discussion section.

Results of the 5 fitted D are presented in Figure 6-3, see Table 6-2 for exact values. The logarithm of D as a function inverse anneal temperate is described as:

$$\log D = \log D_0 - \frac{Q_{Ce}}{2.3R}\left(\frac{1}{T}\right) \quad (2)$$

where D_0 is the pre-exponential factor or pre-diffusion coefficient, Q_{Ce} is the activation energy of Ce with YAP for diffusion, R is the gas constant, and T is the absolute temperature in K. Thus, obtaining the slope and y-intercept of the Arrhenius relationship via a least-squares fit is used to determine Q_{Ce} and D_0. For transport normal to the annealed crystal surfaces, Q_{Ce} and D_0 were estimated to be 1.02 $\pm$ 0.1 eV and $9.7 \pm 2 \times 10^{-15}\ m^2 s^{-1}$, respectively.

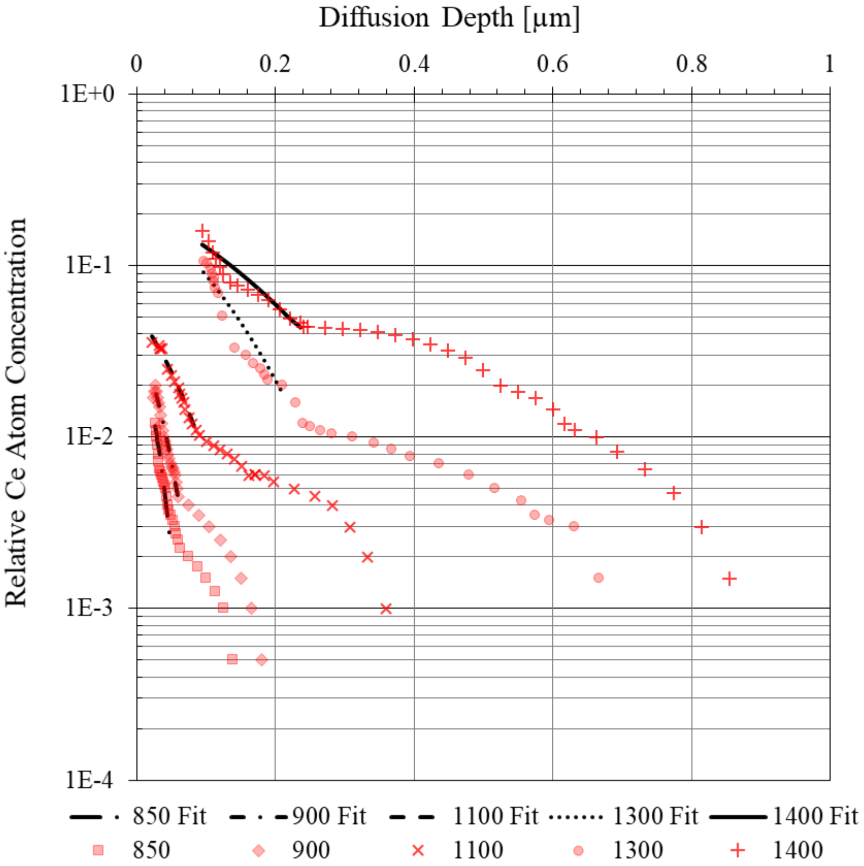

Figure 6-2. Relative Ce concentration as a function of diffusion depth fit with the one dimensional profile for semi-infinite source diffusion.

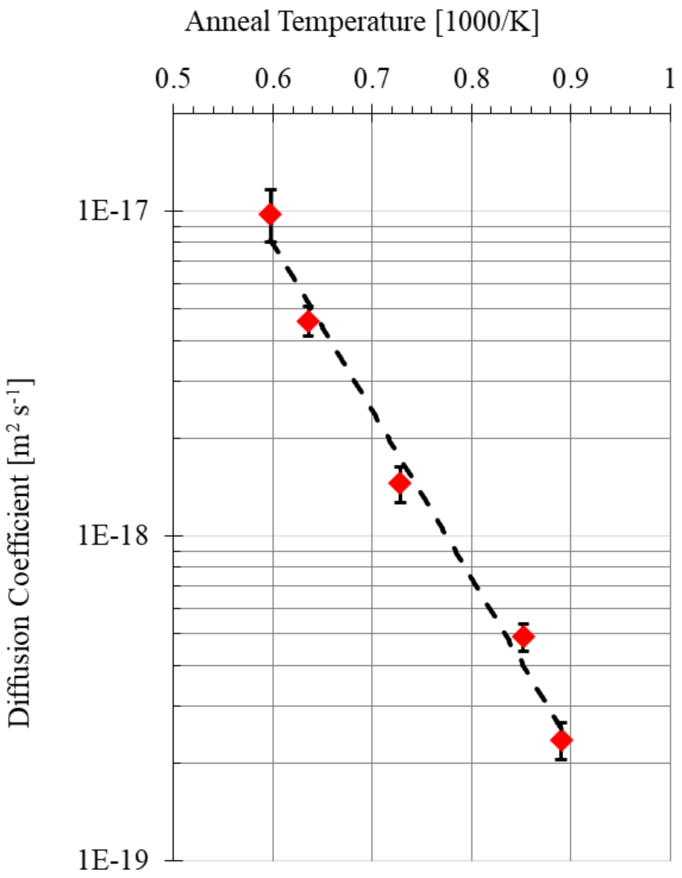

Figure 6-3. Diffusion coefficients for thermally diffused Ce within the annealed YAP Crystals under a reducing environment.

Table 6-2: Ce diffusion coefficients for YAP

Annealing Temperature [°C]	Diffusion Coefficient [10^{-20} m^2s^{-1}]
850	23.5 ± 3
900	49 ± 5
1100	145 ± 18
1300	460 ± 48
1400	980 ± 180

6.4.2X-Ray Diffraction

The structures of the annealed crystals and the diffusion layer were probed with X-ray diffraction (XRD) using a PANalytic Empyrean diffractometer setup in Bragg-Brentano geometry utilizing a PIXcel^{3D} area detector with a Cu-Kα source. The post-annealed Ce diffusion layer on a YAP crystal annealed at 900°C was examined with Powder X-Ray Diffraction (PXRD), see Figure 6-4 (*left*). As expected, it appeared to consist of a roughly even combination of Ce_2O_3 : CeO_2. The annealed crystal itself was then ground into a powder and subsequent PXRD spectra was analyzed with Rietveld Refinement using GSAS-II [121]. The lattice parameters $a = 5.3294(1)$ Å, $b = 7.3715(2)$ Å, and $c = 5.1795(1)$ Å were found, which are typical of single-phase YAP. Grazing Incidence X-Ray Diffraction (GIXRD), which has a low angle of x-ray beam incidence relative to the sample surface, scanning a 2θ range at a fixed incidence angle (ω), was used to observe the surface effects of the Ce diffusion into YAP crystals. For this particular experimental setup, ω corresponded to the depth of measurement in µm, where $\omega = 2°$ diffraction occurred at a depth of 2 µm. At ω values below 2°, the signal-to-noise ratio (SNR) dropped significantly. However, because the relatively large concentration of doped Ce caused disorder at depths beyond the RBS detectable limit of the diffused Ce, multiphase characteristics were observed well past 1 µm, see Figure 6-4 (*right*). Phase identification for the GIXRD spectra was performed using PANalytical X'Pert HighScore software. It was observed that the primary constituents of the complex surface layer were YAP, $Y_3Al_5O_{12}$ (YAG), $Y_4Al_2O_9$ (YAM) with trace amounts of Y_2O_3, CeO_2, Ce_2O_3, and the metastable hexagonal polymorph of $YAlO_3$

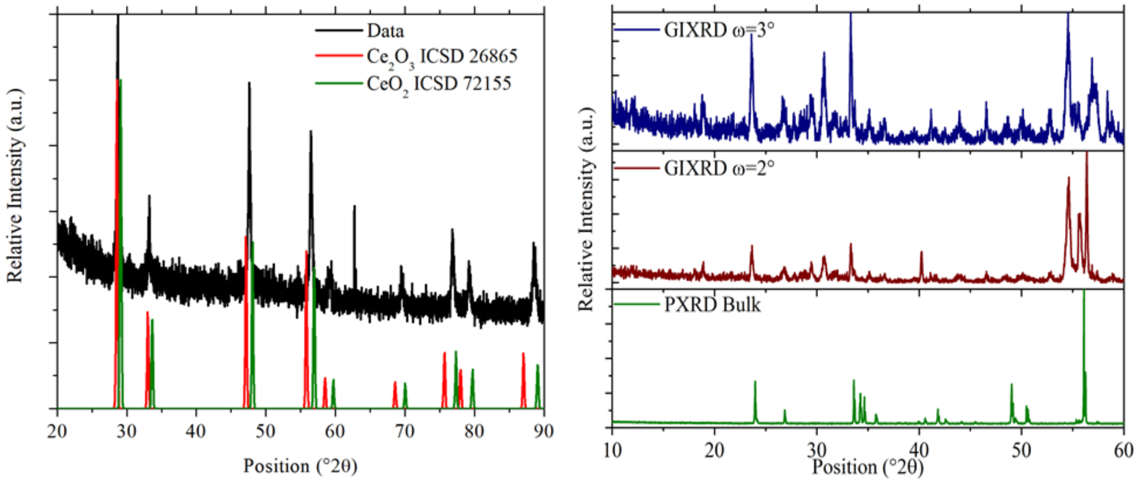

Figure 6-4. Powder X-Ray Diffraction spectra of surface material (*left*), and the stacked plot of bulk powder diffraction spectra and Grazing Incident X-Ray Diffraction spectra of sample S8 at an incident angles of 2° and 3° (*right*).

(YAH). Due to the complexity of the observed multiphase, the specific phase ratios could not be estimated.

6.4.3 Optical Properties

Transmission spectra were measured with a Varian Cary 5000 UV–VIS–NIR spectrophotometer for wavelengths between 200–800 nm. First, S1, S2, and S4 were tinted red following annealing, but S3 remain transparent, see Figure 6-5. Samples annealed at and above 1100°C, or S5-S9, remained visibly clear. Samples S3, S7 and S8 transmitted on average ~15% more ultraviolet (UV) light than the control sample. To further test optical temperature dependence, two additional YAP samples were coated with the Ce diffusion layer and annealed simultaneously at 900°C; one turned red and the other did not. Next, two more YAP samples were annealed in a vacuum tube furnace at 900°C with a new fused quartz tube at ~ 20 mTr under the same atmosphere. Both samples turned red. Finally, a YAP crystal was again annealed at 900°C, this time without a Ce diffusion layer; it also turned red.

The annealed YAP samples were excited with X-rays to characterize the radioluminescence (RL) properties of the $4f \rightarrow 5d$ transition for the diffused Ce. The source was an x-ray tube operated at 35 kV and 0.1 mA. The emission spectra of typical YAP:Ce consists of a single peak centered at 370 nm. The RL spectra of the annealed crystals possessed ultraviolet (UV) and visible light emissions of varied intensities. All sample emissions contained 4 peaks centered at approximately 295 nm, 362 nm, 438 nm, 551 nm. Two distinct emissions profiles indicative of phase

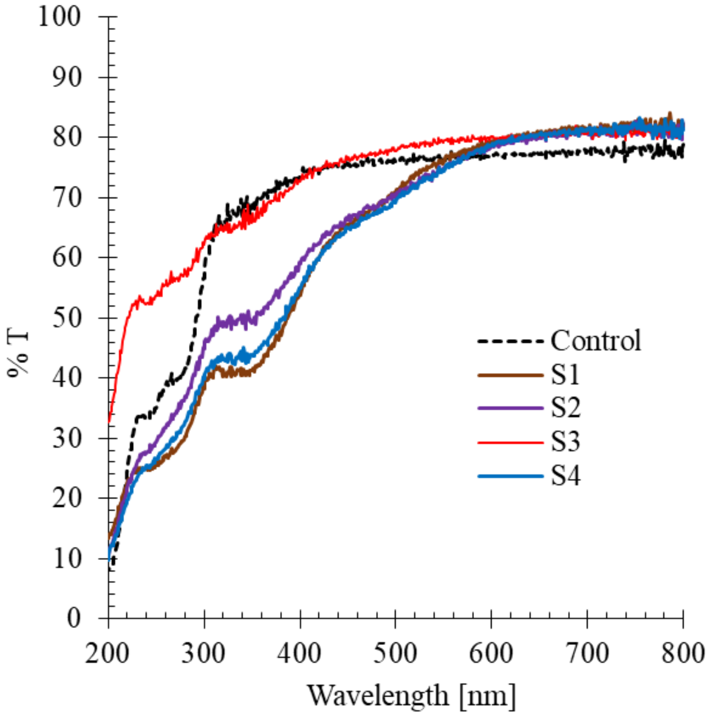

Figure 6-5. Optical transmission for an un-annealed YAP sample and samples annealed at temperatures between 800°C and 1000°C

transformations emerged: 1) a strong near ultraviolet (NUV) emission with an additional emission peak at 630 nm, and 2) a dominate visible 550 nm emission with an additional emission peak at 720 nm, see Figure 6-6. Samples S3, S7 and S8 were characterized as the first type of emission, and the rest of the samples were characterized as the latter.

The α responses from S2-S9 were examined (recall that there was negligible Ce diffusion for S1) using a 1μCi ^{241}Am source. The α source was placed directly onto the Ce-treated surface of the annealed crystals. The untreated back sides of the samples were secured to a R2059 Hamamatsu Photomultiplier Tube (PMT), along with the α source, using Teflon tape. The PMT was biased to -2.1 kV inside of a light-tight dark box, and the signal was readout with a CAEN DT5720 12-bit 250MS/s digitizer. Energy histograms were acquired with a gate width of 500 ns for a total of 600 s, see Figure 6-7. Sample S3, annealed at 900°C, showed the most well-resolved α energy peak.

6.5 Discussion

Before the results of the Ce diffusion are discussed, it is important to consider 2 facets of the experiment: 1) the selection of a simple heat cycle, and 2) the relatively short annealing time. First, it should be understood that in order to determine the activation energy of and study the diffusion mechanisms of the Ce dopant directly, it is best to forego a complex heat cycle for annealing. However, in actual application, it would be ideal to add a thermal soak following the initial Ce diffusion. An additional

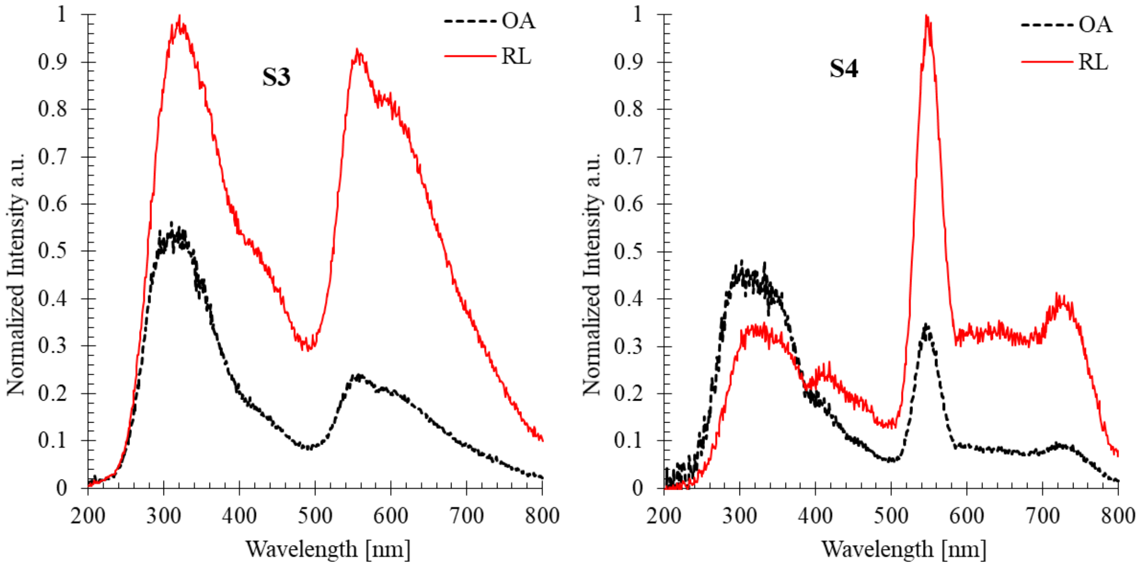

Figure 6-6. Optical Absorption and Radioluminescence of S3 representative of a strong UV profile (left), and of S4 representative of the 550 nm peak dominated profile (right).

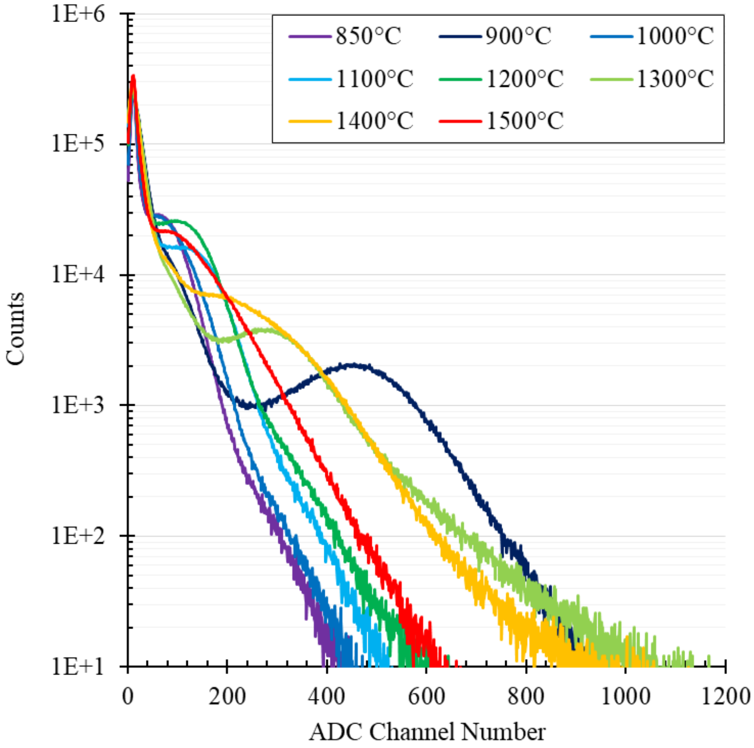

Figure 6-7. Pulse-height spectra of the Ce doped YAP samples as a function of annealing temperature

low temperature soak could be reliably expected to improve the observed optical clarity, relax lattice strain, remove/reduce metastable phases, such as YAH, and potentially increase light yield as trapping defects are eliminated via Frenkel recombination. Second, the 10 hr anneal duration was selected in order to avoid diffusing Ce too deeply for RBS analysis. The spatial resolution of the RBS measurements acquired with 2.0 MeV He^+ drops substantially past 1 μm depth [105]. It is also important to avoid observing overlapping Ce diffusion effects with the He^+ that are not backscattered, but instead are implanted in the YAP crystal at a depth of about 3.8 μm.

The distinctive diffusion regions shown in Figure 6-2 are representative of two diffusion mechanisms, surface and grain boundary diffusion. Due to the highly disordered cation sublattices of the surface phase aggregation, YAP, YAG, YAM, YAH, etc., it is highly likely that the surface transport is dominated by antisite substitutions. It has been shown by [122] that trivalent rare earth metals (REM) prefer to occupy the Y^{3+} sites within YAP and YAP lattices. While trivalent REMs are highly soluble in these crystals, readily occupying the Y^{3+} position, tetravalent REMs increase disorder in random phase aggregation while producing cation vacancies. High concentrations of Ce transitioned the single crystal structure to a polycrystalline surface, and created quasi-amorphous Y_2O_3 and Al_2O_3 phases. Thus, beyond the near-surface region, the diffusion trend is likely dominated by grain boundary diffusion.

Assuming that the trend of thermal diffusion at 1500°C can be calculated based on the derived Q_{Ce} for near surface diffusion and the least squares fit of the modeled temperature dependent $D(T)$, then we are able to estimate $D(1500°C) \approx 1.22 \times 10^{-17}\ m^2 s^{-1}$. Using this value, we can now make an assessment for the duration of heat cycle at 1500°C needed to thermal diffuse Ce 10 µm in YAP at a particular concentration relative to the surface layer ($C_0 : C$), see Table 6-3. This does not consider the contribution from the distinct secondary region of diffusion observed. The activation energy for this 2nd region, Q_{Ce}^{II} , of diffusion was also determined using equations (1) and (2). It was found that Q_{Ce}^{II} was within the stated 0.1 eV error of Q_{Ce}, but the trend was dependent on the chemical potential gradient of the Ce diffused into the near surface of YAP rather than the C_0 of Ce within the diffusion layer.

Optical instability was noted at below 1000°C, where YAP samples tended to turn a reddish color. This kind of instability at lower annealing temperatures is not uncommon; it is likely due to the presence of oxygen vacancies and the resulting absorbing F-centers [123]. It is thought that the relative ratio of the Y_2O_3/Al_2O_3 within a YAP crystal is positively correlated to the degree of the coloration in as-grown crystals [124]. Since Y_2O_3 was observed with GIXRD and Al_2O_3 was not, it is likely that this ratio is greater than 1. However, the bulk sample coloration was not observed as a function of the reducing environment or preparation and application of diffusion coating. Throughout the literature, YAP synthesis is performed at or above 1200°C to produce a pure single crystal phase. Indeed, significant sample-to-sample variations in YAP crystals from Proteus specifically have been reported [125]. Since no red coloration was observed above 1100°C, it was assumed for this study that the YAP samples, although from the same boule, possessed varied amounts of contaminants

Table 6-3 Diffused Ce concentration at 10 μm for 1500°C

Annealing Duration [hr]	Ce Concentration Ratio $[C_0 : C]$
18.8	0.0001
26.3	0.001
42.9	0.01
105.2	0.1
625.6	0.5

that dominate the optical clarity of the samples at low annealing temperatures. Increased visual hazing occurred in samples annealed at and above 1300°C, where the surfaces blackened, and amorphous surface phase transformation of the samples picked up the texture of the ceramic alumina sample boats. Again, an additional low temperature soak could be implemented in a reducing atmosphere to reduce these optical effects. S5 and S6 possessed good visual clarity, similar to S3.

The dominant scintillation process for Ce-doped YAP and YAG is well recognized as the *4f* → *5d* transition of trivalent cerium (Ce^{3+}). When a Ce^{3+} dopant replaces Y^{3+} in a YAP or YAG lattice, the Ce centers emit around the peak wavelengths of 370 nm and 550 nm, respectively. These emission peaks are characteristic of as-grown YAP:Ce and YAG:Ce crystals and are readily observed in the measured RL spectra. Notably, differences in crystal optical absorption have been shown to shift the YAP emission peak by as much as 20 nm [126]. These peaks were accompanied by 295 nm UV and 438 nm emissions, which are attributed to Ce^{3+} ion-localized excitons and Ce^{3+} excitation at the Al^{3+} position with the YAP lattice, respectively [127]. While dominant, Ce^{3+} may not possess the only means of Ce scintillation within the crystals. Under cathodoluminescence, tetravalent cerium (Ce^{4+}) has been observed emitting at typical 550 nm emission for Ce^{3+} in YAG. This was theorized to be caused by a two-part process of an electron entering a Ce^{4+} in an upper *5D* state, effectively creating Ce^{3+}, followed by the *5d* → *4f* transition [128]. In general, however, it is undesirable for a scintillator to possess even a relatively low Ce^{4+} concentration, as its absorption bands overlap with those of Ce^{3+}, causing strong quenching effects and reducing the light yields of most crystals. Maintaining the trivalent state in the diffusion layer during a heat cycle requires atmospheric control since Ce^{3+} will readily oxidize. However, the specific diffusion mechanisms of Ce and the crystalline stability of YAP during the heat cycle ultimately determine the valences and scintillation of Ce in the annealed crystals. From the RL features observed, it is probable that the broad emission band typical of YAM is convolved with the semi-continuous emissions resulting from the increasingly disordered stoichiometry of the YAP lattice [129].

Referring back to Figure 6-7, sample S3, annealed at 900°C, displayed the best resolved α energy peak. This is likely because S3 was most transparent to its own scintillation light, while simultaneously not suffering from deformation. Additionally, the average Ce mol. % estimated with RBS for S3 was 0.86 mol. %, see Figure 6-8, which is near to the ~0.6 mol. % allowed by the single crystal segregation coefficient for as-grown YAP:Ce [117].

The α count rates for the samples can be determined by subtracting out a constant background rate, and then by fitting the energy peaks of the pulse-height spectra with Gaussians. It is reasonable to assume that the intensity of the alpha response increased as annealing temperature increased, until significant visual hazing at 1300°C began, see Figure 6-9. As previously mentioned, a piece of electrical tape was present in the tube furnace during the heating cycle for S7. This is likely to have caused more darkening than otherwise may have occurred at this temperature.

The intensity of measured RL of S2-S9 can also be normalized with the spectral response of the R2059 PMT used to record the pulse-height spectra of the α response.

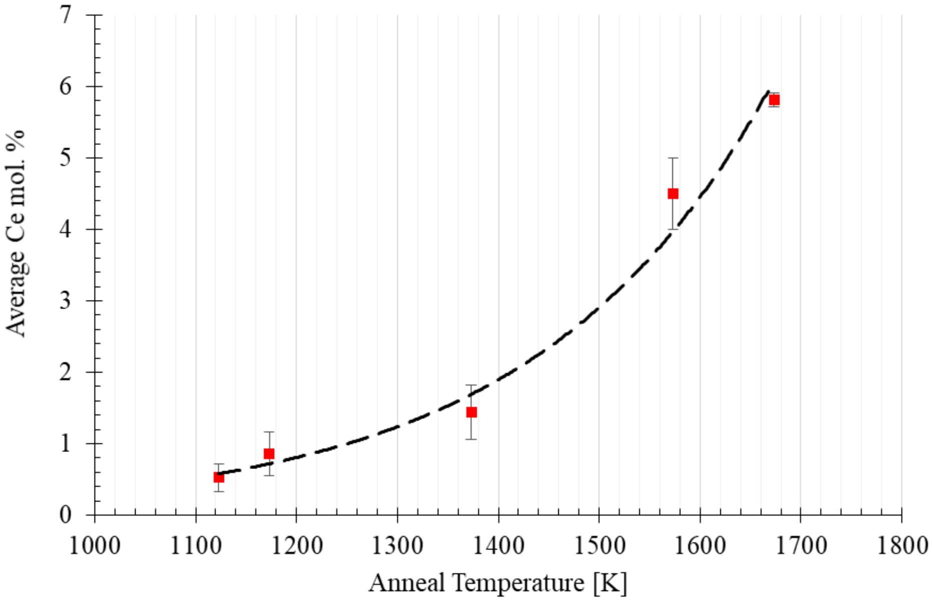

Figure 6-8. Averaged Ce mol. % contained within the doped samples as a function of the annealing temperature.

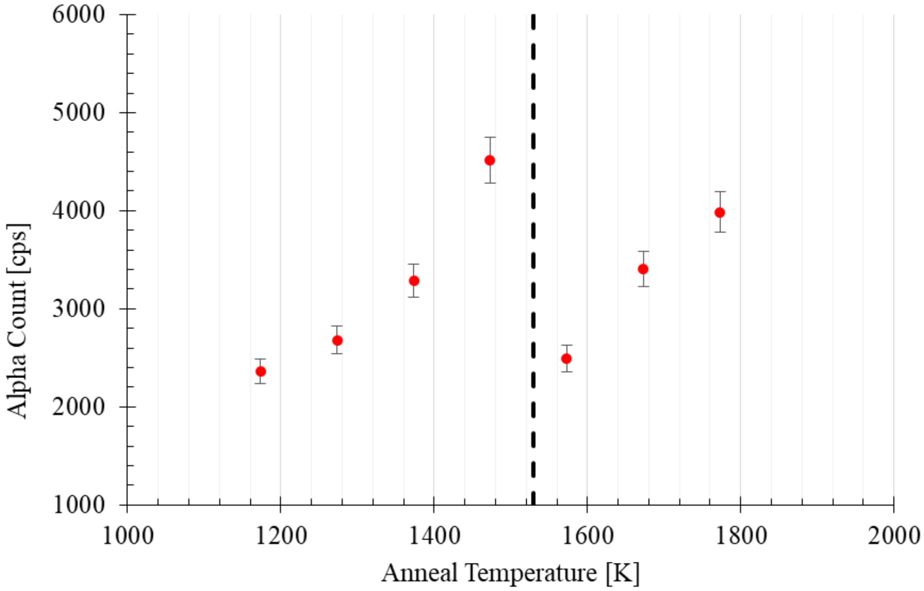

Figure 6-9. Surface Ce doped YAP crystal α count rate as a function of annealing temperature. The dashed line denotes when visual darkening began.

The maximum PMT spectral response is at 420 nm, and the PMT is insensitive to wavelengths larger than 650 nm. The relative spectral contributions of the 4 peaks centered at approximately 295 nm, 362 nm, 438 nm, 551 nm can be estimated from the PMT-normalized RL spectra by comparing the intensity of the fitted peaks. Due to the variation in peak intensity, the error associated with the spectral deconvolution by means of a linear combination of Gaussian functions was substantial for some samples. However, the trend of the derived relative contribution of the NUV emission for the pulse-height measurement does suggest that: 1) the observed NUV emission is dominant for all samples, 2) sample S7 possessed the strongest NUV emission, and 3) the NUV contribution plateaus around 0.7 at annealing temperatures above 1100°C with the exception of S7, see Figure 6-10. The addition of polyethylene to the reducing annealing atmosphere of S7 is the singular significant variant that likely caused this increased NUV emission.

6.6 Conclusion

In summary, the effects of thermally diffusing Ce into the surface of YAP at dopant concentrations greater than typically allowed during growth are described to inform future synthesis of surface scintillating α detectors for potential use with API systems. The diffusion coefficients of Ce from a dried diffusion layer on the surface of YAP were determined for a temperature range of 850 -1400°C using RBS measurements. An activation energy and the pre-exponential factor were derived from the least squares fit of these coefficients were established as 1.02 ± 0.1 eV and $9.7 \pm 2 \times 10^{-15}\ m^2 s^{-1}$,

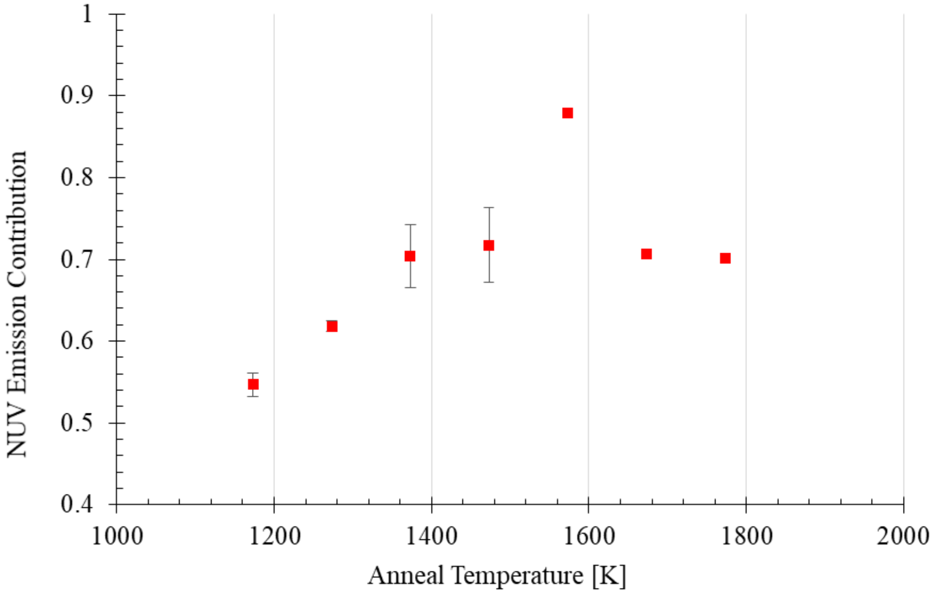

Figure 6-10. PMT spectral response normalized near-ultra-violet emission ratio as a function of annealing temperature.

respectively. It was estimated that at 1500°C several mol. % of Ce can be diffused 10 µm into the surface of YAP between 2 - 4 days under the given annealing conditions. The diffusion of several mol. % of Ce created a complex polycrystalline surface layer within annealed crystals. While the bulk single crystal is confirmed to be YAP, GIXRD indicated the multiphase surface to predominately consist of YAP, YAG, and YAM with trace amounts of Y_2O_3, CeO_2, Ce_2O_3, and YAH phases.

It is suspected that impurities within the YAP samples likely lead to optical instability at lower annealing temperatures. Both higher purity and annealing temperatures are suggested for future API application based research to diffuse Ce to a constant depth of 10 µm within optically clear YAP. It is also worth noting that the addition of a redox catalyst should be considered for the annealing atmosphere to further convert Ce^{4+} to Ce^{3+}. In terms of creating selectively activated regions of a scintillator, additive manufacturing of polycrystalline materials is currently limited to the use of cubic structures to avoid unwanted internal reflection. Although difficult to control, similar thermal doping techniques to the one presented could prove useful for unique applications with other non-cubic crystals as well as other amorphous materials.

Chapter 7

Conclusion

7.1 Summary

Initially, the response of the square packed multicore fiber array to the background (neutron shutter closed), and to the neutron beam (neutron shutter open) was observed. The response to the neutron beam displays an increased integrated charge distribution. Thus, cold neutrons clearly exhibit a higher light output response than the gamma background radiation present in the beamline. Using lessons learned from the measurements at CG-1D, a new multicore design and improved characterization setup were developed.

Li-glass cores with 7-10 μm diameter were drawn into 500 m of an all-solid glass composite, multicore fiber at a 70% packing fraction. It was shown that the Li-glass remains active and scintillates as expected following drawing. Although the Li absorber shows some diffusion into the cladding, the Ce activator is difficult to diffuse and is strongly bound during the multicore fabrication process. Hand-cleaved and polished single fibers of lengths 2-5 mm resolved features on the order of 10s of μm while utilizing the Neutron Microscope. Ideal light collection in these same fibers was theorized to allow for ≤ 20 μm resolution.

Work was planned to evaluate the radiographic spatial resolution of an array of 100 multicore neutron SCIFIs with a 5 x 5 mm field-of-view. This was a comparably thin design (1mm thick), with the outer jacket removed, and a well-polished surface. Since a larger field-of-view was desired for evaluation of imaging performance, the multicore fiber outer jacket was ground away, and a 10×10 array was stacked together. Assembly was finished by securing the array with structural glass plate siding and polishing the surfaces, see Figure 3-6.

The characterization of a SCIFI array via measurements and simulations in an effort to understand its current performance and the future potential for similar designs was completed. The $^{6}Li(n,\alpha)t$ reaction light yield of $7{,}700 \pm 1{,}000$ photons per event was estimated with ^{241}Am irradiation of the faceplate for the Nucsafe glass. This measurement confirmed that the expected light yield of the ^{6}Li glass had not deteriorated during multicore fabrication. Neutron radiographs of a PSI Siemens Star neutron imaging test target yielded an isotropic spatial resolution of $\sim$25 μm across the imaging surface of the SCIFI with 375 minutes of exposure. Here it was suspected that both the spatial and temporal resolution suffered from a nonuniform pixel stacking/polishing within the faceplate. However, specific regions of the faceplate resolved sub-20 μm features. The ultimate resolution for the ^{6}Li glass SCIFI faceplate of $\sim$16 μm was determined by fitting the line spread of these features with a Fourier peak fit. To the authors' knowledge, this resolution is the best reported result for a ^{6}Li-glass-based or any multicore SCIFI-based neutron imager.

Results of the experiments to dope the ^{6}Li loaded glass with an appreciable amount of trivalent Ce suggest that Ce can be thermally diffused at temperatures below 575°C without visual hazing or physical deformation of the glass under the described heating conditions. The activation energy for the Ce diffusion within the glass was found to be 411 ± 53 kJ/mol (4.26 ± 0.55 eV). With this activation energy, it is shown that 1 at.% Ce concentration diffused at least 1 μm with 5 hr of annealing at 550°C. Thus, an order of magnitude higher diffusion depth, or 10s of μm, should be expected following days of annealing at 550°C. For a unique application such as fabricating high resolution, cold neutron imaging detectors for advanced neutron scattering facilities, this length of time is not prohibitive. Upon examining the valence of the diffused Ce, we estimate that a roughly similar ratio, 1:1 of Ce^{3+}: Ce^{4+} valence states exists within the diffusion layer. After annealing with a reducing atmosphere, it was shown that the $Ce4^{+}$: $Ce3^{+}$ ratio is greatest at the samples' surfaces, < 50 nm, 0.80 ± 0.10 $Ce4^{+}$: $Ce3^{+}$, supporting the assumption that a near surface Ce (IV) oxide layer exists. The SNR of the 916.7 eV peak as a function of diffusion depth suggests that Ce is increasingly reduced as it diffuses deeper, and the Ce content is almost completely reduced to Ce^{3+} at depths near 1 μm. Thus, a surface polishing technique applied in an inert environment is expected to be able to remove the layer of tetravalent Ce that accounts for much of its observed concentration.

While the formation of color centers is somewhat expected under prolonged high flux alpha bombardment, the suspected radiation-enhanced reduction of Ce within the silicate was not anticipated given the differences between the Li silicate and pure ceria. It was observed that the Ce intensity after sputtering away the surface layer from the radiation-induced color center was increased by 70 ± 10%. This could suggest that radiation-enhanced reduction may assist in creating regions of selective scintillation within the proposed glass fiber scintillator, provided that the coloring is negligible or reversible.

The effects of thermally diffusing Ce into the surface of YAP at dopant concentrations greater than typically allowed during growth were described to inform future synthesis of surface scintillating α detectors for potential use with API systems. The diffusion coefficients of Ce from a dried diffusion layer on the surface of YAP were determined for a temperature range of 850 - 1400°C using RBS measurements. A least squares fit of these coefficients was used to derive an activation energy and a pre-exponential factor of 1.02 ± 0.1 eV and $9.7 \pm 2 \times 10^{-15}\ m^2 s^{-1}$, respectively. It was estimated that at 1500°C several mol. % of Ce can be diffused 10 μm into the surface of YAP over a time period of 2 - 4 days under the given annealing conditions. The diffusion of several mol. % of Ce created a complex polycrystalline surface layer within annealed crystals. While the bulk single crystal is confirmed to be YAP, GIXRD indicated the multiphase surface to predominately consist of YAP, YAG, and YAM with trace amounts of Y_2O_3, CeO_2, Ce_2O_3, and YAH phases.

7.2 Significance

This dissertation presents the first experimental results from trials to fabricate and characterize microstructured multicore scintillating fiber for a new generation of higher resolution thermal or cold neutron radiography (and perhaps applicable to other instruments as well) at international neutron science facilities. Specifically, the utilization of optoelectronic technology for high resolution neutron radiography has not been published on for nearly 25 years. Optoelectronics fabrication capabilities have clearly advanced over that timeframe. The fabrication technique described has the potential to generate consistent microstructured scintillating neutron sensitive fiber optics with active element pitch of a few microns. At this scale, tracking of the charged particles from the $^{6}Li\ (n,\alpha)\ ^{3}H$ reaction could allow for estimating thermal neutron interaction locations with micron-level precision on an event-by-event basis, overcoming the inherent uncertainty that comes with the variance in the orientations of charged particle tracks in neutron imaging scintillators. The experimental neutron imaging results described in this dissertation are the best reported for a ^{6}Li-glass-based or any scintillating multicore fiber-based neutron imager, showing that this technology has the potential to meet or exceed the state-of-the-art capabilities of the neutron imaging field.

In terms of creating selectively activated regions of a scintillator, additive manufacturing of polycrystalline materials is currently limited to the use of cubic structures to avoid unwanted internal reflection. Although difficult to control, similar thermal doping techniques to the one presented could prove useful for unique applications with other non-cubic crystals as well as other amorphous materials.

7.3 Recommendations for Continued Work

To increase the spatial resolution of the described SCIFI neutron imager, the core glass must be drawn to smaller sizes which should be possible with the current fabrication process. The unfiltered spatial resolution measured is roughly equal to twice the pitch of the core packing. Recall that the average simulated contrast ratio is approximately equal to 7.2:17.5. In theory, this would suggest that at ~50% of the modulation transfer function, a similar multicore design with a core pitch of 500 nm would be capable of resolving features on the order of 1 μm.

Besides the scale of the architecture, the proof-of-concept design itself has ample room for optimization. The current design could be improved upon by simply adding a reflective coating to one end of the faceplate. Moreover, fabrication without an outer cladding jacket will allow for more straightforward array assembly. Image contrast improvement primarily requires the use of a lower refractive index cladding material. Although not as simple, selecting a compatible optical cladding with a lower n_{clad} value would increase the contrast of the multicore fiber. (Success in fabrication of air-filled capillaries would be ideal but was found to be beyond the scope of this work.) An increase in single core numerical aperture would not only enhance light collection in individual cores but it would also reduce the inter-core optical cross-talk. For example, phosphate glass cladding possessing a refractive index of $n_c < 1.53$, could be used for another neutron SCIFI fabrication. Such a cladding could be expected to allow for more than twice the current amount of scintillation light to remain internally bound.

The possibility of directly coupling an optic SCIFI taper to a readout chip, imaging window, or even MCP touts potential light collection efficiencies that will be ever more important as the imaging community continues to probe increasingly smaller scales. Directly coupling to image at the micron scale would either require extremely precise aligning of individual fibers to pixels or use of a CCD with sub-micron pixel sizes. Radiation hardening of photosensors would be another important development. Once more light can be collected by improvements to the design and/or direct coupling, event centroiding and deconvolution of particle tracks [43] are post-processing abilities that may also be applied to further improve the spatial resolution of an optimized wave-guiding SCIFI.

Future work with Ce diffusion should include the use of the obtained activation energy to produce monolithic glass samples appropriate for efficient cold neutron detection and imaging and thorough characterization of the scintillation properties of samples in which the same Ce compound has been more deeply diffused. It is suspected that impurities within the YAP diffusion samples likely lead to optical instability at lower annealing temperatures. Both higher purity and annealing temperatures are suggested for future API application-based research to diffuse Ce to a constant depth of 10 μm within optically clear YAP. It is also worth noting that the addition of a redox catalyst should be considered for the annealing atmosphere to further convert Ce^{4+} to Ce^{3+}.

References

[1] R. Satija, D. L. Jacobson, M. Arif, and S. Werner, "*In situ* neutron imaging technique for evaluation of water management systems in operating PEM fuel cells," Journal of Power Sources, vol. 129, pp. 238-245, 2004.

[2] H. Kallmann, Neutron Radiography Research 1, 254, 1948.

[3] J. Chadwick, "Possible existence of a neutron." *Nature* 129.3252 (1932): 312.

[4] I. S. Anderson, R. McGreevy, and H.Z. Bilheux, et al. *Neutron Imaging and Applications: A Reference for the Imaging Community.* Springer. May 2009.

[5] "Neutron Physics." *Paul Scherrer Institute*, www.psi.ch/niag/neutron-physics, accessed February 27, 2019.

[6] S. Peetermans and E. H. Lehmann, "Simultaneous neutron transmission and diffraction contrast tomography as a non-destructive 3D method for bulk single crystal quality investigations," *Journal of Applied Physics,* vol. 114, p. 124905, 2013.

[7] E. H. Lehmann, et al. "Recent applications of neutron imaging methods." (2017): 5-12.

[8] H. Bilheux, J. Bilheux, A. Tremsin, L. Santodonato, R. Dehoff, M. Kirka*, et al.*, "Overview of the Neutron Radiography and Computed Tomography at the Oak Ridge National Laboratory and Applications," in *ASNT 24th Research Symposium 2015*, 2015, pp. 18-23.

[9] N. Kardjilov, A. Hilger, I. Manke, M. Strobl, M. Dawson, and J. Banhart, "New trends in neutron imaging," *Nuclear Instruments and Methods in Physics Research Section A: Accelerators, Spectrometers, Detectors and Associated*

Equipment, vol. 605, pp. 13-15, 6/21/ 2009.

[10] N. Kardjilov, I. Manke, A. Hilger, M. Strobl, and J. Banhart, "Neutron imaging in materials science," *Materials Today,* vol. 14, pp. 248-256, 6// 2011.

[11] M. Strobl, I. Manke, N. Kardjilov, A. Hilger, M. Dawson, and J. Banhart, "Advances in neutron radiography and tomography," *Journal of Physics D: Applied Physics,* vol. 42, p. 243001, 2009.

[12] D. J. Hare, et al. "Imaging metals in biology: balancing sensitivity, selectivity and spatial resolution." *Chemical Society Reviews* 44.17 (2015): 5941-5958.

[13] H. Simons, et al. "Dark-field X-ray microscopy for multiscale structural characterization." *Nature communications* 6 (2015): 6098.

[14] X. Chen, et al. "Visualizing electronic interactions between iron and carbon by X-ray chemical imaging and spectroscopy." *Chemical science* 6.5 (2015): 3262-3267.

[15] A. S. Tremsin, et al., "Neutron radiography with sub-15 μm resolution through event centroiding," *Nuclear Instruments and Methods in Physics Research Section A: Accelerators, Spectrometers, Detectors and Associated Equipment* 688 (2012): 32-40.

[16] S. H. Williams, et al. "Detection system for microimaging with neutrons," *Journal of Instrumentation* 7.02 (2012): P02014.

[17] A. E. Craft, D. M. Wachs, M. A. Okuniewski, D. L. Chichester, W. J. Williams, G. C. Papaioannou, et al., "Neutron radiography of irradiated nuclear fuel at Idaho National Laboratory," *Physics Procedia,* vol. 69, pp. 483-490, 2015.

[18] S. Peetermans and E. Lehmann, "Exploiting diffraction in neutron imaging to reveal spatial variation in crystal properties," *Neutron News,* vol. 26, pp. 39-43, 2015.

[19] A. S. Tremsin, M. G. Makowska, D. Perrodin, T. Shalapska, I. V. Khodyuk, P. Trtik*, et al.*, "*In situ* diagnostics of the crystal-growth process through neutron imaging: application to scintillators," *Journal of Applied Crystallography,* vol. 49, 2016.

[20] S. Sanabria, C. Lanvermann, F. Michel, D. Mannes, and P. Niemz, "Adaptive Neutron Radiography Correlation for Simultaneous Imaging of Moisture Transport and Deformation in Hygroscopic Materials," *Experimental Mechanics,* vol. 55, pp. 403-415, 2015.

[21] A. Schröder, K. Wippermann, W. Lehnert, D. Stolten, T. Sanders, T. Baumhöfer*, et al.*, "The influence of gas diffusion layer wettability on direct methanol fuel cell performance: A combined local current distribution and high resolution neutron radiography study," *Journal of Power Sources,* vol. 195, pp. 4765-4771, 2010.

[22] I. Manke, C. Hartnig, N. Kardjilov, M. Messerschmidt, A. Hilger, M. Strobl*, et al.*, "Characterization of water exchange and two-phase flow in porous gas diffusion materials by hydrogen-deuterium contrast neutron radiography," *Applied physics letters,* vol. 92, p. 244101, 2008.

[23] M. Hickner, N. Siegel, K. Chen, D. Hussey, D. Jacobson, and M. Arif, "Understanding liquid water distribution and removal phenomena in an

operating PEMFC via neutron radiography," *Journal of The Electrochemical Society,* vol. 155, pp. B294-B302, 2008.

[24] A. D. Santamaria, M. K. Becton, N. J. Cooper, A. Z. Weber, and J. W. Park, "Effect of cross-flow on PEFC liquid-water distribution: An in-situ high-resolution neutron radiography study," *Journal of Power Sources,* vol. 293, pp. 162-169, 2015.

[25] H.G. Jung, J. Hassoun, J.B. Park, Y.K. Sun, B. Scrosati, "An improved high-performance lithium-air battery," Nature Chemistry 4, 579-585 (2012), doi: 10.1038/nchem.1376.

[26] N. Imanishi, A. C. Luntz, and P. Bruce, *The lithium air battery: fundamentals*: Springer, 2014.

[27] J. Nanda et al., "Anomalous Discharge Product Distribution in Lithium-Air Cathodes," Jour. Phys. Chem. C 116 (2012) 8401-8408.

[28] L. Seung Wook, K. Ki-Yeon, K. Oh Yeoul, K. Nikolay, D. Martin, H. Andre, et al., "Observation of Magnetic Domains in Insulation-Coated Electrical Steels by Neutron Dark-Field Imaging," Applied Physics Express, vol. 3, p. 106602, 2010.

[29] I. Manke, N. Kardjilov, M. Strobl, A. Hilger, and J. Banhart, "Investigation of the skin effect in the bulk of electrical conductors with spin-polarized neutron radiography," Journal of Applied Physics, vol. 104, p. 076109, 2008.

[30] B. Khaykovich, et al. "Novel neutron focusing mirrors for compact neutron sources." *Physics Procedia* 26 (2012): 299-308.

[31] D. K. Rai, et al. "Focusing mirrors for enhanced neutron radiography with thermal neutrons and application for irradiated nuclear fuel." *Nuclear Instruments and Methods in Physics Research Section A: Accelerators, Spectrometers, Detectors and Associated Equipment* 879 (2018): 141-146.

[32] H. Bilheux, K. Herwig, S. Keener, and L. Davis, "Overview of the Conceptual Design of the Future VENUS Neutron Imaging Beam Line at the Spallation Neutron Source," *Physics Procedia,* vol. 69, pp. 55-59, 2015.

[33] M. Strobl. "The scope of the imaging instrument project ODIN at ESS." *Physics Procedia* 69 (2015): 18-26.

[34] Y. Wang, et al. "Ultrafast X-ray study of dense-liquid-jet flow dynamics using structure-tracking velocimetry." *Nature Physics* 4.4 (2008): 305.

[35] M. L. Taubin, A. A. Yaskolko, and D. A. Chesnokov. "Thermal Analysis of the Focal Spot of Anodes of Powerful X-Ray Tubes." *Biomedical Engineering* (2018): 1-4.

[36] P. Trtik, and E.H. Lehmann. "Isotopically-enriched gadolinium-157 oxysulfide scintillator screens for the high-resolution neutron imaging." *Nuclear Instruments and Methods in Physics Research Section A: Accelerators, Spectrometers, Detectors and Associated Equipment* 788 (2015): 67-70.

[37] G.F. Knoll, Radiation detection and measurement, John Wiley & Sons, 2010.

[38] J. L. Wiza, "Microchannel plate detectors." *Nucl. Instrum. Methods* 162.1-3 (1979): 587-601.

[39] G. W. Fraser and J. F. Pearson, "The direct detection of thermal neutrons by imaging microchannel-plate detectors." *Nuclear Instruments and Methods in Physics Research Section A: Accelerators, Spectrometers, Detectors and Associated Equipment* 293.3 (1990): 569-574.

[40] W. B. Feller, Robert Gregory Downing, and Paul L. White. "Neutron field imaging with microchannel plates." *Hard X-Ray, Gamma-Ray, and Neutron Detector Physics II*. Vol. 4141. International Society for Optics and Photonics, 2000.

[41] A. S. Tremsin, W. Bruce Feller, and R. Gregory Downing. "Efficiency optimization of microchannel plate (MCP) neutron imaging detectors. I. Square channels with 10B doping." *Nuclear Instruments and Methods in Physics Research Section A: Accelerators, Spectrometers, Detectors and Associated Equipment* 539.1-2 (2005): 278-311.

[42] A. S. Tremsin, et al. "High-resolution neutron radiography with microchannel plates: Proof-of-principle experiments at PSI." *Nuclear Instruments and Methods in Physics Research Section A: Accelerators, Spectrometers, Detectors and Associated Equipment* 605.1-2 (2009): 103-106.

[43] Y. Song, J. Conner, X. Zhang, and J. P. Hayward, "Monte Carlo simulation of a very high resolution thermal neutron detector composed of glass scintillator microfibers," *Applied Radiation and Isotopes,* vol. 108, pp. 100-107, 2016.

[44] B. Schillinger, *Neue Entwicklungen zu Radiographie und Tomographie mit thermischen Neutronen und zu deren routinemäßigem Einsatz*: Mensch-und-

Buch-Verlag, 1999.

[45] M. B. Chadwick, et al. "ENDF/B-VII. 0: next generation evaluated nuclear data library for nuclear science and technology." *Nuclear data sheets* 107.12 (2006): 2931-3060.

[46] A. R. Spowart. "Neutron scintillating glasses: Part 1. Activation by external charged particles and thermal neutrons." *Nuclear Instruments and Methods* 135 (1976): 441-453.

[47] J. Ziegler, J. Biersack, M. Ziegler, The Stopping and Range of Ions in Matter, SRIM, 2013, http://www.srim.org, (2013).

[48] L. Katz and A.S. Penfold. "Range-energy relations for electrons and the determination of beta-ray end-point energies by absorption." *Reviews of Modern Physics* 24.1 (1952): 28.

[49] 6-Lithium Enriched Glass Scintillators, https://scintacor.com/products/6-lithium-glass/ (accessed Jan. 11, 2019).

[50] A. R. Spowart, "Measurement of the absolute scintillation efficiency of granular and glass neutron scintillators." *Nuclear Instruments and Methods* 75.1 (1969): 35-42.

[51] G. Ban, et al. "Ultracold neutron detection with 6 Li-doped glass scintillators." *The European Physical Journal A* 52.10 (2016): 326.

[52] C. W. E. Van Eijk. "Inorganic-scintillator development." Nuclear Instruments and Methods in Physics Research Section A: Accelerators, Spectrometers, Detectors and Associated Equipment 460.1 (2001): 1-14.

[53] Scintillation Materials, Catalog, Nuclear Enterprises Ltd., 1990.

[54] C. L. Wang, and Richard A. Riedel. "Improved neutron-gamma discrimination for a 6Li-glass neutron detector using digital signal analysis methods." *Review of Scientific Instruments* 87.1 (2016): 013301.

[55] C. W. E. van Eijk. "Inorganic scintillators for thermal neutron detection." *IEEE Transactions on Nuclear Science* 59.5 (2012): 2242-2247.

[56] K. D. Ianakiev, et al. "Neutron detector based on Particles of 6Li glass scintillator dispersed in organic lightguide matrix." *Nuclear Instruments and Methods in Physics Research Section A: Accelerators, Spectrometers, Detectors and Associated Equipment* 784 (2015): 189-193.

[57] S. G. Brollo, Zanella, and R. Zannoni. "Light yield in cerium scintillating glasses under X-ray excitation." *Nuclear Instruments and Methods in Physics Research Section A: Accelerators, Spectrometers, Detectors and Associated Equipment* 293.3 (1990): 601-605.

[58] P. Ottonello, et al. "Slow neutron imaging using scintillating glass optical fibers." Nuclear Instruments and Methods in Physics Research Section A: Accelerators, Spectrometers, Detectors and Associated Equipment 349.2-3 (1994): 526-531.

[59] P. A. Hausladen, et al. "Portable fast-neutron radiography with the nuclear materials identification system for fissile material transfers." *Nuclear Instruments and Methods in Physics Research Section B: Beam Interactions with Materials and Atoms* 261.1-2 (2007): 387-390.

[60] T. A. Wellington, et al. "Recent fast neutron imaging measurements with the fieldable nuclear materials identification system." *Physics Procedia* 66 (2015): 432-438.]

[61] B. Canion, Seth McConchie, and Sheldon Landsberger. "Point kinetics framework for characterizing prompt neutron and photon signatures from tagged neutron interrogation." *IEEE Transactions on Nuclear Science* 64.7 (2017): 1761-1768.

[62] M. L. Litvak, et al. "The dynamic albedo of neutrons (DAN) experiment for NASA's 2009 Mars science laboratory." *Astrobiology* 8.3 (2008): 605-612.

[63] M. L. Litvak, et al. "Associated particle imaging instrumentation for future planetary surface missions." Nuclear Instruments and Methods in Physics Research Section A: Accelerators, Spectrometers, Detectors and Associated Equipment 922 (2019): 19-27.

[64] J. W. Cates, "Investigation of Time and Position Resolved Alpha Transducers for Multi-Modal Imaging with a DT Neutron Generator." (Doctoral dissertation, University of Tennessee, Knoxville) (2013).

[65] M. Nikl, “Scintillation detectors for x-rays,” Meas. Sci. Technol. 17, R37–R54 (2006).

[66] H. Leutz, “Scintillating fibres,” in Nuclear Instruments and Methods in Physics Research Section A Accelerators Spectrometers Detectors and Associated Equipment 364 (3), 422-448 (1995).

[67] N. Miyanaga, N. Ohba, and K. Fujimoto, "Fiber scintillator/streak camera detector for burn history measurement in inertial confinement fusion experiment," Review of Scientific Instruments. 68 (1), 621–623 (1997).

[68] A. Vedda, N. Chiodini, D. Di Martino, et al. “Ce3+ -doped fibres for remote radiation dosimetry,” Applied Physics Letters, 85 (26), 6356-6358, (2004).

[69] N. Chiodini, et al. "Ce-doped SiO_2 optical fibers for remote radiation sensing and measurement." *Fiber Optic Sensors and Applications VI*. Vol. 7316. International Society for Optics and Photonics, 2009

[70] P. Ottonello, G. A. Rottigni, G. Zanella, and R. Zannoni, “Neutron Imaging with Scintillating-Glass Fiber-Optic Plates,” Journal of Neutron Research 4(1-4), 109-116 (1996).

[71] R. A. Buckles, Z. A. Ali, J. R. Cradick, et al. “Scintillating Fiber Array Characterization and Alignment for Neutron Imaging using the High Energy X-ray (HEX) Facility,” in Proc. The Sixth International Conference on Inertial Fusion Sciences and Applications (2009).

[72] R. Ruchti, et al. "A Scintillating Glass, Fiber-Optic Plate Imaging System for Active Target and Tracking Applications in High Energy Physics Experiments." *IEEE Transactions on Nuclear Science* 30.1 (1983): 40-43.

[73] M. Atkinson, et al. "Initial tests of a high resolution scintillating fibre (SCIFI) tracker." Nuclear Instruments and Methods in Physics Research Section A: Accelerators, Spectrometers, Detectors and Associated Equipment 254.3 (1987): 500-514.

[74] M. Morgano, et al. "Unlocking high spatial resolution in neutron imaging through an add-on fibre optics taper." *Optics Express* 26.2 (2018): 1809-1816.

[75] M. E. Moore, et al. "A multicore compound glass optical fiber for neutron imaging." *Optical Fiber Sensors Conference (OFS), 2017 25th*. IEEE, 2017.

[76] M. E. Moore, et al. "Thermal diffusion of mixed valence Ce in ^{6}Li loaded silicate glass for neutron imaging." *Journal of Non-Crystalline Solids* 498 (2018): 145-152.

[77] G. H. Frischat. "Sodium diffusion in SiO2 glass." *Journal of the American Ceramic Society* 51.9 (1968): 528-530.

[78] W. Beier and G. H. Frischat. "A mass spectrometric method for the determination of Li self diffusion in oxide glasses." *Journal of Non-Crystalline Solids* 38 (1980): 569-573.

[79] W. Li, and S.H. Garofalini. "Molecular dynamics simulation of lithium diffusion in Li2O–Al2O3–SiO2 glasses." *Solid State Ionics* 166.3-4 (2004): 365-373.

[80] J.O. Isard. "The mixed alkali effect in glass." *Journal of Non-Crystalline Solids* 1.3 (1969): 235-261.

[81] L. Santodonato, et al. "The CG-1D neutron imaging beamline at the oak Ridge National Laboratory high flux isotope reactor." *Physics Procedia* 69 (2015): 104-108.

[82] P. Trtik, and E. H. Lehmann. "Progress in High-resolution Neutron Imaging at the Paul Scherrer Institut-The Neutron Microscope Project." Journal of Physics: Conference Series, vol. 746. No. 1. IOP Publishing, 2016.

[83] U. Stuhr, et al. "Time-of-flight diffraction with multiple frame overlap Part II: The strain scanner POLDI at PSI." *Nuclear Instruments and Methods in Physics Research Section A: Accelerators, Spectrometers, Detectors and Associated Equipment* 545.1-2 (2005): 330-338.

[84] C. Grünzweig, et al. "Highly absorbing gadolinium test device to characterize the performance of neutron imaging detector systems." *Review of Scientific Instruments* 78.5 (2007): 053708.

[85] R. R. Dehoff, et al. "Site specific control of crystallographic grain orientation through electron beam additive manufacturing." *Materials Science and Technology* 31.8 (2015): 931-938.

[86] T. Minniti, et al. "Towards high-resolution neutron imaging on IMAT." *Journal of Instrumentation* 13.01 (2018): C01039.

[87] M. E. Moore, et al. "Fabrication and experimental evaluation of microstructured ^{6}Li silicate fiber arrays for high spatial resolution neutron imaging." *Nuclear Instruments and Methods in Physics Research Section A: Accelerators, Spectrometers, Detectors and Associated Equipment* (2018).

[88] J. S. Sanghera, et al. "Development of low-loss IR transmitting chalcogenide glass fibers." *Biomedical Optoelectronic Instrumentation*. Vol. 2396. International Society for Optics and Photonics, 1995.

[89] OpticStudio, Zemax. "15.5." *Zemax LLC, Seattle, WA* (2016).

[90] E. J. Fairley, and A.R. Spowart. "Neutron scintillating glasses: Part III. Pulse decay time measurements at room temperature." *Nuclear Instruments and Methods* 150.2 (1978): 159-163.

[91] Weston, Ken. Message to the author. 11 January 2019. E-mail.

[92] P. Trtik, et al. "Improving the spatial resolution of neutron imaging at paul scherrer institut–the neutron microscope project." *Physics Procedia* 69 (2015): 169-176.

[93] C. A. Schneider, W.S. Rasband, and K.W. Eliceiri. "NIH Image to ImageJ: 25 years of image analysis." *Nature methods* 9.7 (2012): 671.

[94] T. Ferreira, and W. Rasband. "ImageJ user guide." *ImageJ/Fiji* 1 (2012).

[95] N. Kardjilovet et al. "A highly adaptive detector system for high resolution neutron imaging." Nuclear Instruments and Methods in Physics Research Section A: Accelerators, Spectrometers, Detectors and Associated Equipment 651.1 (2011): 95-99.

[96] A. S. Tremsin, et al. "Digital neutron and gamma-ray radiography in high radiation environments with an MCP/Timepix detector." *Nuclear Instruments and Methods in Physics Research Section A: Accelerators, Spectrometers, Detectors and Associated Equipment* (2018).

[97] R. O. Nelson, et al. "Neutron Imaging at LANSCE—From Cold to Ultrafast." *Journal of Imaging* 4.2 (2018): 45.

[98] V. F. Sears, "Neutron scattering lengths and cross sections." *Neutron news* 3.3

(1992): 26-37.

[99] L. Bollinger, G. Thomas, R. Ginther, "Neutron detection with glass scintillators." *Nuclear Instruments and Methods* 17.1 (1962): 97-116.

[100] A. R. Spowart, "Neutron scintillating glasses: Part II: The effects of temperature on pulse height and conductivity." *Nuclear Instruments and Methods* 140.1 (1977): 19-28.

[101] L. A. Boatner, J. T. Mihalczo, "High spatial resolution particle detectors." U.S. Patent No. 9,158,008. 13 Oct. 2015.

[102] X. Zhang, M.E. Moore, K.-M. Lee, E.D. Lukosi, J.P. Hayward, "Study of cerium diffusion in undoped lithium-6 enriched glass with Rutherford backscattering spectrometry." *Nuclear Instruments and Methods in Physics Research Section B: Beam Interactions with Materials and Atoms*, 378 (2016): 8-11.

[103] T. Behrsing, et al. "Cerium acetylacetonates—new aspects, including the lamellar clathrate [Ce (acac) 4]· 10H2O." *Inorganica chimica acta* 352 (2003): 229-237.

[104] National Center for Biotechnology Information. PubChem Substance Database; SID=24863813, https://pubchem.ncbi.nlm.nih.gov/substance/24863813 (accessed Dec 14, 2017).

[105] Y. Zhang, et al. "New ion beam materials laboratory for materials modification and irradiation effects research." *Nuclear Instruments and Methods in Physics Research Section B: Beam Interactions with Materials and Atoms* 338 (2014):

19-30.

[106] M. Mayer, *SIMNRA user's guide*. Garching: Max-Planck-Institut für Plasmaphysik, 1997.

[107] R. E. Stoller, et al. "On the use of SRIM for computing radiation damage exposure." Nuclear instruments and methods in physics research section B: beam interactions with materials and atoms 310 (2013): 75-80.

[108] R. W. Johnson, and D. S. Martin Jr. "Kinetics of the oxidation of cerium (III) by concentrated nitric acid." *Journal of Inorganic and Nuclear Chemistry* 10.1-2 (1959): 94-102.

[109] P. Burroughs, et al. "Satellite structure in the X-ray photoelectron spectra of some binary and mixed oxides of lanthanum and cerium." *Journal of the Chemical Society, Dalton Transactions* 17 (1976): 1686-1698.

[110] H. Ebendorff-Heidepriem, D. Ehrt, "Formation and UV absorption of cerium, europium and terbium ions in different valencies in glasses." *Optical Materials* 15.1 (2000): 7-25.

[111] M. L. Brandily-Anne, et al. "Specific absorption spectra of cerium in multicomponent silicate glasses." *Journal of Non-Crystalline Solids* 356.44-49 (2010): 2337-2343.

[112] V. Singh, et al. "Characterization, Luminescence, and Defect Centers of a Ce 3+-Doped Li 2 Si 2 O 5 Phosphor Prepared by a Solution Combustion Reaction." *Journal of Electronic Materials* 44.8 (2015): 2736-2744.

[113] C. Sun, H. Li, L. Chen. "Nanostructured ceria-based materials: synthesis, properties, and applications." *Energy & Environmental Science* 5.9 (2012): 8475-8505.

[114] M. Moszyński, et al. "Properties of the YAG: Ce scintillator." Nuclear Instruments and Methods in Physics Research Section A: Accelerators, Spectrometers, Detectors and Associated Equipment 345.3 (1994): 461-467.

[115] R. Pani, et al. "Multi-crystal YAP: Ce detector system for position sensitive measurements." Nuclear Instruments and Methods in Physics Research Section A: Accelerators, Spectrometers, Detectors and Associated Equipment 348.2-3 (1994): 551-558.

[116] C. J. Wharton, et al. "X-Ray Measurements Of A Thermo Scientific P385 DD Neutron Generator." *AIP Conference Proceedings*. Vol. 1336. No. 1. AIP, 2011.

[117] S. Baccaro, et al. "Scintillation properties of YAP: Ce." Nuclear Instruments and Methods in Physics Research Section A: Accelerators, Spectrometers, Detectors and Associated Equipment 361.1-2 (1995): 209-215.

[118] J. W. Cates, J. P. Hayward, and X. Zhang. "Increased light extraction from inorganic scintillators with laser-etched microstructures." *IEEE Transactions on Nuclear Science* 60.2 (2013): 1027-1032.

[119] D. J. Cherniak, "Sr and Nd diffusion in titanite." *Chemical Geology* 125.3-4 (1995): 219-232.

[120] P. Shewmon, "Diffusion in Solids, The Minerals." *Metals & Materials Society, Warrendale, PA* (1989): 37-38.

[121] B. H. Toby and Robert B. Von Dreele. "GSAS-II: the genesis of a modern open-source all purpose crystallography software package." *Journal of Applied Crystallography* 46.2 (2013): 544-549.

[122] M. M. Kuklja. "Defects in yttrium aluminium perovskite and garnet crystals: atomistic study." *Journal of Physics: Condensed Matter* 12.13 (2000): 2953.

[123] H. J. Kim. "Computational design of new scintillator chemistries and defect structures." (Doctoral dissertation, Iowa State University) (2015).

[124] D. Sugak, et al. "Optical in situ study of reduction/oxidation processes in YAlO3." *Acta Materialia* 56.20 (2008): 6310-6318.

[125] S. B. Donnald, et al. "Sample-to-sample variation in single crystal YAP: Ce non-proportionality." *IEEE Transactions on Nuclear Science* 61.1 (2014): 332-338.

[126] S. B. Donnald. "A Study of Energy Resolution and Non-proportionality of YAlO3: Ce and Gd3Ga3Al2O12: Ce." (Doctoral dissertation, University of Tennessee, Knoxville) (2014).

[127] V. Babin, et al. "Irregular Ce3+ and defect-related luminescence in YAlO3 single crystal." *Journal of luminescence* 124.2 (2007): 273-278.

[128] S. R. Rotman, H. L. Tuller, and C. Warde. "Defect-property correlations in garnet crystals. VI. The electrical conductivity, defect structure, and optical properties of luminescent calcium and cerium-doped yttrium aluminum garnet." *Journal of applied physics* 71.3 (1992): 1209-1214.

[129] G. Okada, et al. "Characterizations of Ce-doped Y4Al2O9 Crystals for Scintillator Applications." *Sensors and Materials* 30.7 (2018): 1547-1554.

Appendix

A summary of previous work (prior to the studies reported in this dissertation) to simulate and develop glass scintillator microfiber arrays follows. Significant simulation work (reported in [43]) was performed to develop a design for microfiber fiber array capable of inferring the position of thermal neutron capture with ~ 1μm resolution via charged conversion particle tracking. Based on the simulations of the neutron conversion particle track lengths (with TRIM), light transport (with ZEMAX), nuclear interaction, and light collection physics (with Geant4.10.0p1), a detector assembly composed of cerium doped lithium glass microfiber with 1 μm diameters was proposed. These scintillating core fibers were to be surrounded by air-filled glass capillaries with 1 μm diameters to reduce the cross talk of the scintillation light, see Figure A-1. Simulations for this design were performed to determine an ideal refractive index difference and core separation to yield single mode behavior and negligible crosstalk between adjacent cores. The empirical basis for this determination comes from the Snyder and Love formulae that gives the beat length (i.e. length after which there is a complete power transfer) as a function of the fiber parameters. It was determined that glasses with an index around 1.51 would be ideal, with a core-to-core separation of ~2.2 μm. This is similar to the refractive index value put forward in Chapter 3 for the hexagonal packed multicore design.

The square microfiber design was fabricated with using photonic crystal patterning techniques at the University of Southampton's Optoelectronics Research Centre. A 6 × 6 multicore fiber composed of cladded core surrounded by 8 cladded air capillaries was drawn and stacked into a larger 5 × 5 array of fibers to have 900 neutron sensitive cores at a ~2 μm pitch. The core glass was the same glass reported in this dissertation, i.e. Guardian Glass (Nucsafe Inc., Oak Ridge, TN, USA). The

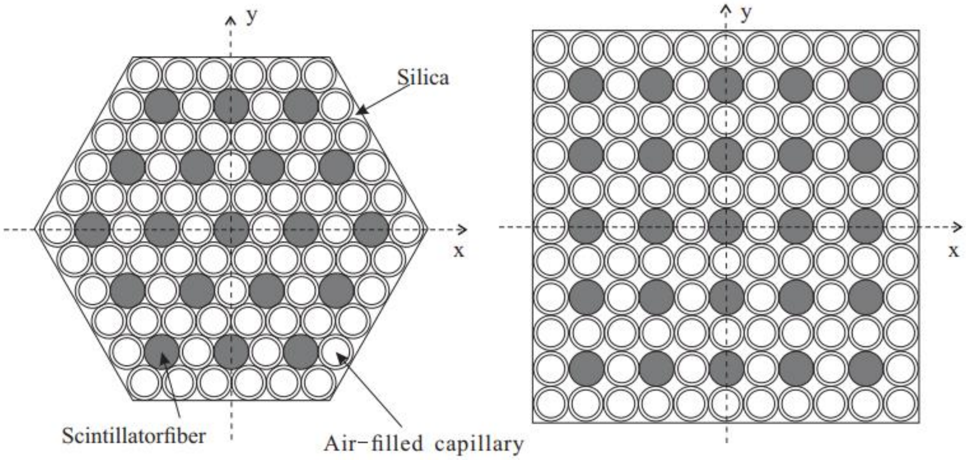

Figure A-1. The schematic layout (not to scale) of both hexagonal and square microfiber assemblies are viewed in neutron beam direction [43].

cladding glass choice was to be “soft,” and mechanically compatible with the core glass. A variant of the commercially available LLF1 SCHOTT glass was produced for the cladding at Southampton. The individual canes of the cladded core and the air capillaries were pulled to diameters of ~ 0.6 mm before drawing the 6 × 6 array, see Figure A-2. These elements were stacked in the square geometry, the preform was sealed to encapsulate the capillaries, and the multicore fiber was drawn under a N_2 atmosphere with significantly irregular geometry, see Figure A-3. It was observed that the LLF1 glass possessed a relatively lower drawing temperature compared to the Li-glass, and that the air capillaries tended to collapse. The multicores were subsequently reheated in a graphite mold again under a N_2 atmosphere to reduce the lead oxide inside the LLF1 glass. However, the Li-glass cores were crystallized. Finally, the multicore fibers were then loaded inside a thick round glass jacket to be drawn to the 1 μm scale. The fibers were not drawn under a vacuum and the preform was not sealed. The drawing failed. Fibers were lost, and the irregularity of the geometry worsened, see Figure A-4.

The lead silicate LLF1 glass was used because it was thought to be compatible with the Li-glass. However, while reheated in the reducing atmosphere, the lead in LLF1 was reduced to metallic lead, which increased optical loss. Structural deformations occurred during the fabrication process due to the difference in drawing temperature, the chemical instability of the glasses in contact, and over pressurization of the air within the sealed capillaries. While pressurization is needed to push against the force of the extrusion to prevent the capillaries from collapsing, too high of a pressure resulted in having

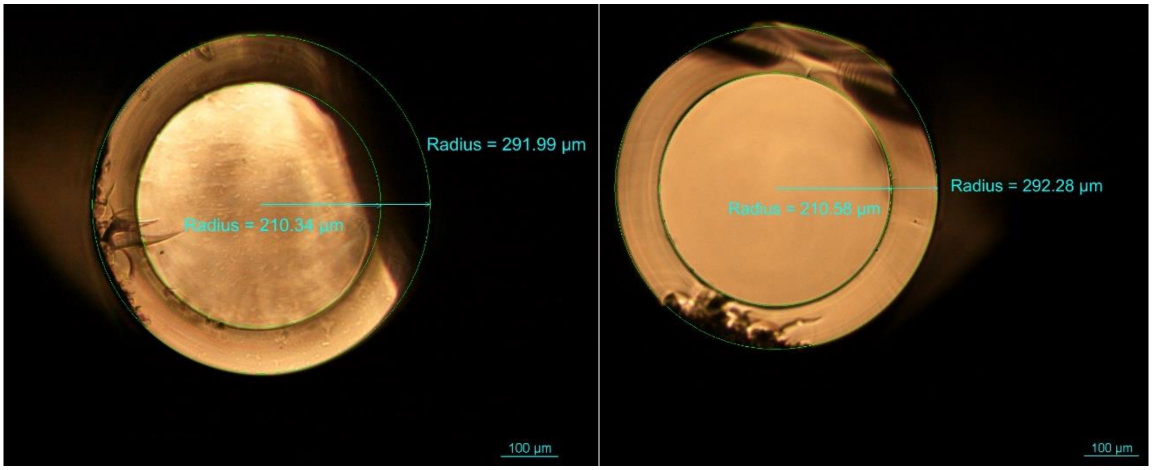

Figure A-2. Optical photos of the cane of Li-glass core cladded with LLF1 (*right*), and air-filled LLF1 glass capillary (*left*) prior to drawing microfiber array.

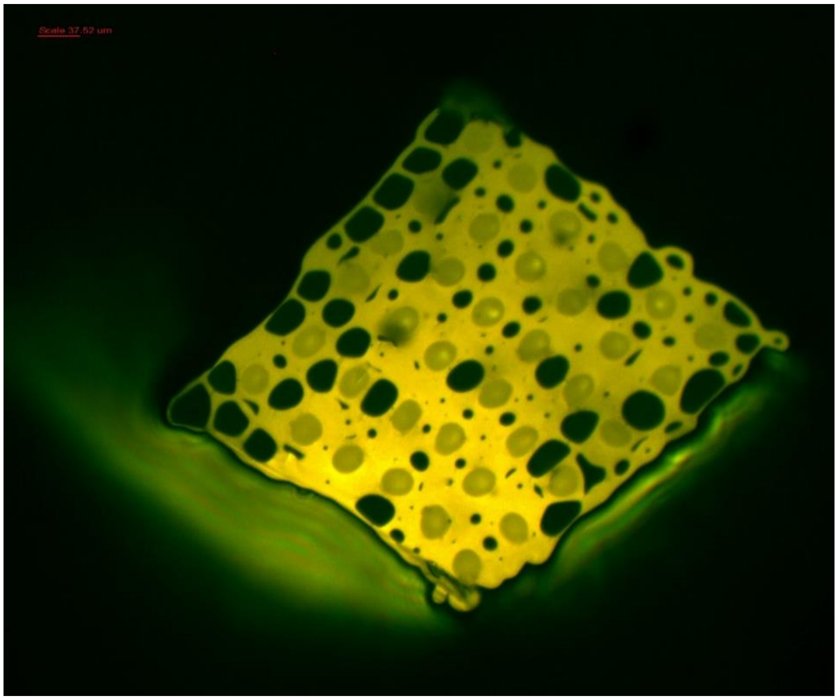

Figure A-3. Optical photo of the irregular structure resulting from the square packed multicore fiber.

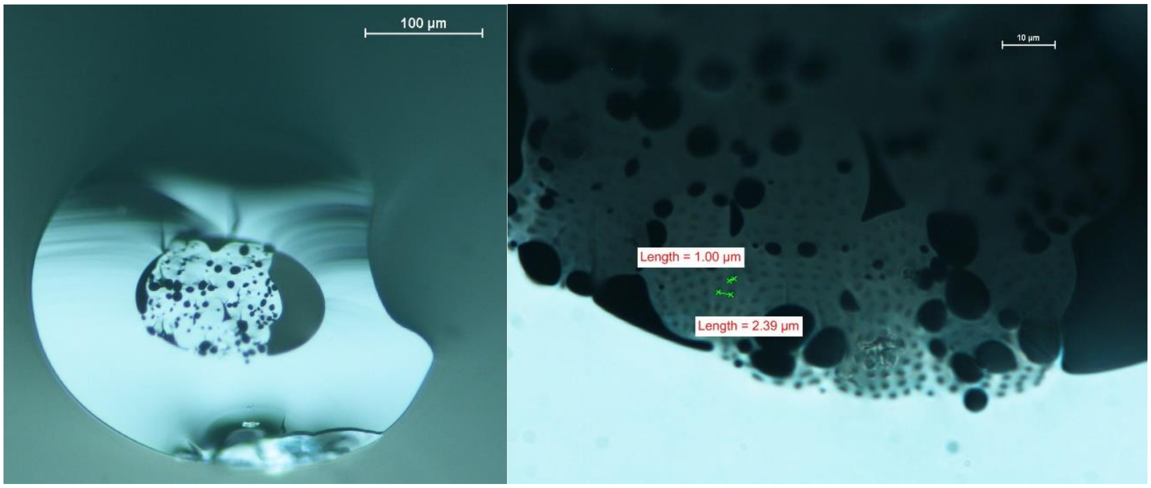

Figure A-4. Optical photos of the failed array of multicore microfibers in the round glass jacket (*left*), and the magnified multicore ends with the Li-glass core dimensions and pitch denoted (*right*).

most capillaries break. From these past observations, an all-solid-glass design was decided on for the following iteration of the microfiber array, which is presented in Chapter 2.

Vita

Michael Edward Moore was born in Pittsburgh, PA. He obtained an A.S. in Engineering Science with honors from the Community College of Allegheny College in 2013. Moore then attended The Pennsylvania State University, within the Department of Mechanical and Nuclear Engineering, where he began his academic research with Prof. Igor Jovanovic. During his undergraduate studies, he was awarded the U.S. Department of Homeland Security's and the Domestic Nuclear Detection Office's Nuclear Forensics Undergraduate Fellowship, the American Nuclear Society's Human Factors, Controls, and Instrumentation Division Nuclear Power Scholarship, and was inducted into the engineering honor society, Tau Beta Pi. In 2015, he graduated with a B.S. in Nuclear Engineering. In the autumn of 2015, Moore then attended The University of Tennessee, Knoxville, where he continued his studies with Prof. Jason Hayward within the Department of Nuclear Engineering. He researched a Li glass multicore fiber thermal neutron imager for high resolution on the university campus and at international neutron science user facilities. After completing that work, Moore began fundamental research to describe synthesize of a partially activated amorphous and crystal scintillators, the latter was investigated for associated particle imaging applications. In April of 2019, he received the Department of Nuclear Engineering PhD Graduate Research Excellence Award, which is typically presented to one PhD student in the department each year.